Processing and Properties of Polymer-based Composites for Metamaterials Applications

Yunqi Wang

St Cross College

Trinity Term 2015

A thesis submitted for the degree of Doctor of Philosophy at the

University of Oxford

Abstract

Transformation optics offers a theoretical tool for the design of electromagnetic devices that can manipulate the flow of microwaves in an unprecedented way, but also places demanding requirements on the permittivity ε and permeability μ of materials used to form the devices, along with their spatial variations in three dimensions. Polymers that are light-weight and with high processability are considered potentially useful in realizing transformation optic designs, but only where the effective ε and μ can be increased controllably by loading the polymer with inorganic particles. This thesis focuses on the development of bespoke polymer-based composite materials and robust manufacturing approaches for potential applications in electromagnetic devices.

Three main manufacturing approaches have been explored. Firstly, casting was demonstrated to produce bulk materials with equal permittivity and permeability by embedding NiZn ferrite particles in an epoxy matrix. Hybrid composites with a combination of soft magnetic ferrite and metallic magnetic fillers, anisotropic composites with magnetic field aligned fillers, and high magnetic anisotropic materials with multi-layered structures were all produced successfully. Developed materials showed superior electromagnetic properties to many competitor approaches for miniaturization and low profile antenna, especially for the case of magnetically anisotropic cast tiles. Secondly, a spray deposition approach was developed for the fabrication of large-scale nanocomposite polymer-based films. By incorporating Fe_3O_4 nanoparticles or multi-wall carbon nanotubes, as a thin sandwich layer into a perfluoro

alkoxy (PFA) matrices respectively, 30-50 μm thick flexible multilayer nanocomposite films with enhanced dielectric and magnetic properties were produced. A broadband permittivity and permeability measurement technique was also developed for these films. Finally, a 3D printing technique was employed to produce electromagnetic materials with complex 3D shape. Feedstock on a ferrite/acrylonitrile butadiene styrene (ABS) composite filament was demonstrated successfully and may facilitate the realization of complex design transformation optics devices.

Acknowledgements

This thesis would not have been possible without the support and help from numerous people who assisted and inspired me throughout this work.

First and foremost, I would like to express my deepest gratitude to my supervisor Prof. Patrick Grant for his invaluable guidance, fruitful discussions and continuous encouragement throughout my DPhil study and his great support on my financial aid opportunity. I am very grateful that he gave me the great freedom and the space to pursue my project in the directions that most interested me, and encouraged me to attend various workshops and international conferences which allowed me to communicate and establish relationships with experts in the field. Without his investment of time and efforts, the project would never reach the fruition.

I also deeply appreciate the advice and support from my supervisor in UK Defence Science and Technology Laboratory (DSTL), Dr. Nathan Clow, who travells far to Oxford to discuss and help me a lot with questions of antennas and simulations. I am very thankful for his invaluable guidance on the applications of developed materials and great encouragement on my produced results.

I would also like to thank my colleagues in the QUEST project. Very thanks to Dr. Ian Hooper for his very kind help with measurement and simulation. Many thanks are also

given to Dr. Susie Speller, Dr. Eleanor Edwards, Dr. Claire Dancer, Dr. Robert Foster, Dr. Yangjie liu, Dr. Flynn Castles, Dr. Dmitry Isakov, Dr. Rhiannon Mitchell-Thomas, Dr. Luigi La Spada, Ms. Juliana Mohd Janurudin, Ms. Qin Lei, Mr. Majid Naeem, Ms. Laura Parke, Dr. Joseph Dockrey for their very kind help and support. I would like to thank the Electromagnetic and Acoustic Materials group at University of Exeter for access to the equipment.

I also owe a lot of gratitude to Dr. Colin Johnston, Dr. Alison Crossley, Ms. Gabriella Chapman, and Mr. Chris Salter, who trained me on different equipments and were always offering me helpful suggestions; Dr. Paul Warren, for his kind help with IT problems. I would also like to extend my thanks to the great colleagues in my group: Mr. Robin Vincent, Mr. Richard Turner for technical supports; Dr. Hongtao Zhang, Dr. Chaopeng Fu, Dr. Enzo Liotti, and Dr. Atsushi Sato for their help and intelligent advices; Dr. Laura O'Neill, Dr. Ann Huang, Dr. Amoghavarsha Mahadevegowda, Mr. Zuliang Hong for their encouragement and discussion; My office colleagues Dr. Ziqian Ding, Dr. Long Jiang, Mr. Vincent Tobin, Ms. Liye Yan, and last Ms. Julie Young and Ms. Jan Pearson for their assistance in everything and bring the group as a big family.

I would like to thank all my friends in Oxford, particularly Ms. Zhe Sha and Ms. Yiduo Wang, who made my life in Oxford so wonderful.

My deeply gratitude goes to my other half, Dr. Baojun Tang. Thank you for coming into my life and bring out the best in me. Thank you to encourage and advise me all the time. Your sharing valuable research experience made my DPhil study with less

detours. Thank you to accompany me travelling around the world and bring me the special moment of my life in Iceland. I truly appreciate that we insist on our belief even when we separated in different cities most of time.

Finally, I owe my deepest love and admiration to my parents, Mr. Huishen Wang and Mrs. Yanli Wang, who share my happiness and sorrow on the road of my life. This thesis would never been made into reality without their endless love and spiritual support.

This work is funded by the UK Engineering and Physical Sciences Research Council (EPSRC) through the programme "The Quest for Ultimate Electromagnetics using Spatial Transforms (QUEST)" and the UK Defence Science and Technology Laboratory (DSTL). The author would also like to acknowledge the use of the Advanced Research Computing (ARC) in carrying out this work.

Contents

List of Figures

List of Tables

Chapter 1

Introduction

The study of metamaterials and their interaction with electromagnetic radiation has emerged as a new research area in the last decade. Metamaterials are regarded as a human-made or contrived composite composed of an engineered sub-wavelength structure, whose functional performance are due directly to the periodic structure.[1] As a nascent but fast growing field, metamaterials have been suggested in theory and demonstrated in practice to offer a wide variety of exotic electromagnetic characteristics that cannot be induced by monolithic materials. Such characteristics include negative refraction,[2] spatial varying refractive index or anisotropic electromagnetic properties, where the former may be used, for example, for high resolution super focusing lenses,[3-6] while the latter can be used for invisibility cloaks via spatial transformation optics.[7,8] Less dramatically but perhaps more significantly, metamaterials can offer significant reductions in the size of the classical devices required in microwave engineering, such as antennas[9,10] and sensors[11], and may also offer a higher capability than conventional material-device combinations.

The electromagnetic properties of materials are usually characterized by a dielectric permittivity ε and a magnetic permeability μ, and another important material parameter of refractive index $n = \sqrt{\varepsilon\mu}$ can be determined accordingly. Most materials in nature have a relative permittivity $\varepsilon_r = \varepsilon/\varepsilon_0$ larger than unity, and a relative permeability $\mu_r = \mu/\mu_0$ also approximately unity, where ε_0 and μ_0 are the permittivity and permeability of free space or air. Metamaterials on the other hand can realize much greater variations in ε and μ, including negative values by appropriate design of the cellular or periodic sub-wavelength architectures comprising materials of different composition.

Recent breakthroughs in the theory of spatial transformation optics[12] provide a design framework to control the propagation of electromagnetic waves when the spatial distribution of permittivity and permeability of materials can be controlled. The most common approach to realise the required electromagnetic properties of materials suggested by transformation optics designs are based on local resonances of periodic arrays of sub-wavelength metallic structures, including wire meshing,[13] split ring resonators,[14] omega-type resonators,[15] metallic rod pairs,[16] and fishnets[17]. However, while producing sometimes exotic behaviours such as negative ε and μ, these arrangements often have the drawback of narrow bandwidth operation, high material losses and difficulties in practical implementation.

Another approach that dispenses with the resonant approach, and is generally referred to as the "all-dielectric" approach, uses composites with functional, randomly arranged nano- and micro-inclusions (usually based on a polymer matrix), and have also

demonstrated cloaking[18] and flat antenna[19] devices. The all dielectric approach generally produces narrower manipulations of ε and μ, but because it does not rely on resonant behaviours, can offer much greater bandwidth while the use of polymeric matrix material provides much more convenience and flexibility for practical implementation.

Nevertheless, for both resonant (periodic) and all-dielectric (non-resonant) approaches, the associated and suitable materials and manufacturing processes are current bottlenecks in metamaterial technology, while theory and simulation continue to advance. The major challenges are: (1) most photonic or microwave sub-wavelength structures show desired properties only over narrow wavelengths and are otherwise extremely lossy or even efficient absorbers; (2) good quality material samples with a wide range of controllable (frequency-dependent) values of permittivity and especially permeability that can serve the material requirements determined by transformation optics are not readily available; and (3) the development of flexible manufacturing technology capable of making useful devices such as lenses or antennas, rather than small scale, crafted ornaments in the laboratory only.

This thesis focuses on development of polymer-based magnetic composites (permeability > 1) with controllable permittivity and permeability, and "all-dielectric" manufacturing approaches. The objectives of the research are:

- To develop polymer-based magnetic composites with tailored values of permittivity and permeability to expand the range of materials available for all-dielectric approaches to novel manipulations of microwaves.
- To investigate the process-microstructure-property relationships in developed materials and to relate material electromagnetic performance to microstructure.
- To explore the capability of easy-to-process routes to produce polymer-based composites that are inexpensive, scalable and can be conveniently arranged spatially or can be directly formed into 3D geometries transformation-based designs.

Bibliography

1 T. J. Cui, D. Smith, and R. Liu, *Metamaterials: Theory, Design, and Applications*. (Springer, 2009).

2 D. R. Smith, J. B. Pendry, and M. C. K. Wiltshire, Science **305**, 788 (2004).

3 J. B. Pendry, Phys. Rev. Lett. **85**, 3966 (2000).

4 S. Anantha Ramakrishna, J. B. Pendry, M. C. K. Wiltshire, and W. J. Stewart, J. Mod. Opt. **50**, 1419 (2003).

5 X. S. Rao and C. K. Ong, Phys. Rev. E **68**, 067601 (2003).

6 W.Genov Cai, D. A. Shalaev, V. M., Phys. Rev. B **72**, 193101 (2005).

[7] J. Valentine, J. Li, T. Zentgraf, G. Bartal, and X. Zhang, Nat. Mater. **8**, 568 (2009).

[8] H. Chen, C. T. Chan, and P. Sheng, Nat. Mater. **9**, 387 (2010).

[9] R. W. Ziolkowski and A. Erentok, IEEE Trans. Antennas Propag. **54**, 2113 (2006).

[10] A. Alù, F. Bilotti, N. Engheta, and L. Vegni, IEEE Trans. Antennas Propag. **55**, 13 (2007).

[11] T. Chen, S. Li, and H. Sun, Sensors **12**, 2742 (2012).

[12] J. B. Pendry, D. Schurig, and D. R. Smith, Science **312**, 1780 (2006).

[13] J. B. Pendry, A. Holden, D. Robbins, W. J. Stewart, and I. Youngs, Phys. Rev. Lett. **76**, 4773 (1996).

[14] J. B. Pendry, A. Holden, D. Robbins, and W. J. Stewart, IEEE Trans. Microwave Theory Tech. **47**, 2075 (1999).

[15] J. Huangfu, L. Ran, L. Chen, X. -H. Zhang, K. Chen, T. M. Grzegorczyk, and J. A. Kong, Appl. Phys. Lett. **84**, 1537 (2004).

[16] Z. G. Dong, H. Liu, M. X. Xu, T. Li, S. M. Wang, S. N. Zhu, and X. Zhang, Opt. Express **18**, 18229 (2010).

[17] M.Tsiapa Kafesaki, I.Katsarakis, N.Koschny, Th.Soukoulis, C. M.Economou, E. N., Phys. Rev. B **75**, 235114 (2007).

[18] D. Bao, K. Z. Rajab, Y. Hao, E. Kallos, W. Tang, C. Argyropoulos, Y. Piao, and S. Yang, New. J. Phys. **13**, 103023 (2011).

[19] W. Tang, C. Argyropoulos, E. Kallos, W. Song, and Y. Hao, IEEE Trans. Antennas Propag. **58**, 3795 (2010).

Chapter 2

Literature Review

This literature review describes the fundamentals and applications of metamaterials, and then introduces the spatial transformation technique that provides the theoretical support for metamaterials design. The basic principles and frequency responses of the two macroscopic electromagnetic parameters, permittivity and permeability, are discussed. The typical designs and manufacturing technologies for metamaterials are then introduced. Metamaterials based on composites that may offer the potential for practical applications are discussed in detail.

2.1 Metamaterials

2.1.1 Fundamentals and Applications

Metamaterials are artificial materials engineered to offer electromagnetic properties that are difficult or impossible to achieve with naturally appearing materials.[1] Recently, metamaterials have become a major topic of research and discussion in a growing

number of scientific publications, because these artificially constructed materials can control the propagation of electromagnetic waves in unprecedented ways. Accordingly, metamaterials represent the next level of structurally altered materials, hence the prefix based on the Greek μετά (meta) that means "beyond". The unusual and desired properties of metamaterials are due to their particular designed structures and compositions. Metamaterials are composed of elements, in the same sense as matter consists of atoms, which interact with electromagnetic waves to produce electric and magnetic moments. When the wavelength, λ, of an incident electromagnetic wave is hundreds of times larger than the elements of which the material is composed, the electromagnetic wave passing through the structure cannot perceive the details of the elements. Conceptually, from the electromagnetic point of view, the inhomogeneous medium is replaced by a homogeneous medium which is characterized by two macroscopic electromagnetic parameters: the electric permittivity ε, and the magnetic permeability μ. The values of ε and μ are described by the scattering properties of any collection of structured objects whose size and spacing are much smaller than λ, not strictly arising from the response of atoms or molecules.[1] In other words, the inclusion of small inhomogeneities which are on length-scales much smaller than one wavelength of the radiation enacts effective macroscopic behaviour of the bulk composite medium.

Metamaterials can be made by embedding one or more controlled inclusions in a specified host material. The type, size, morphology, and compositions of inclusions, and the properties of matrix materials are a large collection of independent design parameters that can be explored to produce the targeted electromagnetic properties.[2]

The electromagnetic properties of materials are described by the macroscopic parameters ε and μ. The permittivity is a measure of how easily a dielectric polarizes when subjected to an electric field. The permeability is the degree of magnetization that a material obtains in response to an applied magnetic field.

In optics, the index of refraction, n, is a measure of the optical density of the medium and is defined as:

$$n = \frac{c}{v} \tag{2.1}$$

where c is the velocity of light propagation in free space, and v is the velocity of an electromagnetic wave in the medium. The denser the medium the lower the velocity of the electromagnetic wave propagation.

According to Maxwell's equations, the index of refraction is defined by the Maxwell relation:

$$n^2 = \varepsilon\mu \tag{2.2}$$

There are four possible combinations for the signs of ε and μ: (+,+), (+,-), (-,+) and (-,-). The classification of a medium was given by Ziolkowski[3] as shown schematically in Fig. 2.1.

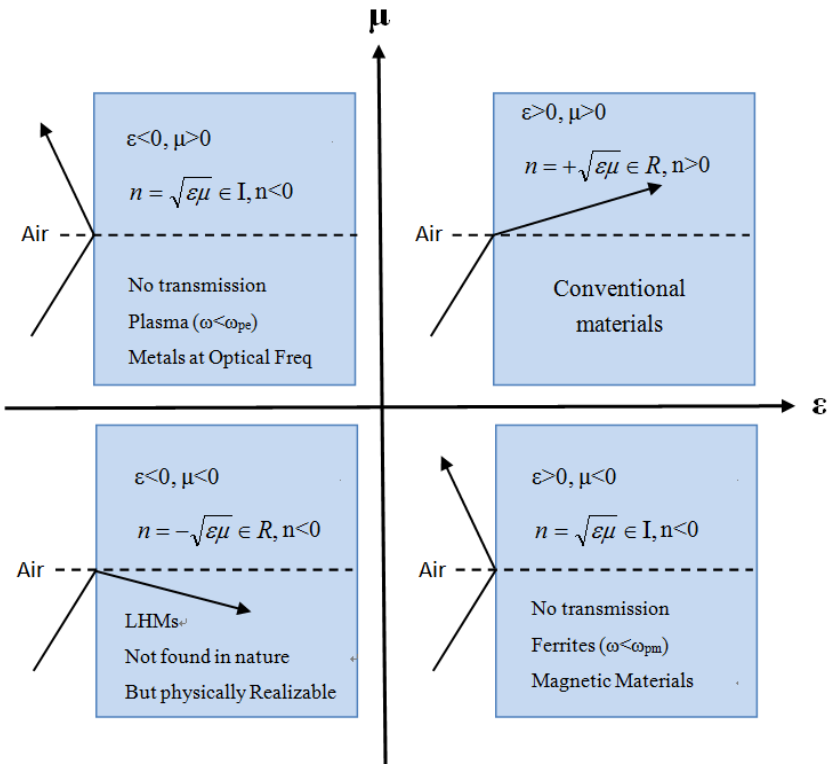

FIG. 2.1. Material classification based on the signs of permittivity and permeability. The diagram is showing the possible domains of electromagnetic materials and wave refractions. Wave refraction happens positively in the conventional materials and negatively in the LHMs. The arrows indicate the directions of electromagnetic wave vector in the medium. Redrawn from [3].

Many naturally occurring materials, such as dielectrics, fall under the designation of positive permittivity and permeability ($\varepsilon>0$, $\mu>0$), and thus they are called as double-positive (DPS) media. If both of these quantities are less than zero ($\varepsilon<0$, $\mu<0$), they are called double-negative (DNG) or left-handed materials (LHMs). In 1967, Veselago[4] first pointed out that a medium should have a negative refractive index $n = -\sqrt{\varepsilon\mu}$ if it has simultaneously negative ε and μ at a given frequency. Because the product of ε and μ is positive, n is real and such substances can transmit light. However, this class of materials has not been found in nature to date. In the last few years,

structured photonic media whose ε and μ could become negative in certain frequency regimes have been demonstrated with artificial constructs.[5,6] The realization of negative refractive index materials brings the idea of perfect lenses which are able to provide image details with a resolution beyond the conventional positive-index lenses diffraction limit close to becoming realisable.[7]

The category of materials with one negative parameter of ε or μ is called single-negative (SNG). In the case of a medium with permittivity less than zero and permeability greater than zero ($\varepsilon<0, \mu>0$), they are sub-categorised as epsilon-negative (ENG). Natural materials, such as cold plasma and the noble metals silver and gold, exhibit this characteristic in the microwave and optical frequency domains. A medium with permittivity greater than zero and permeability less than zero ($\varepsilon>0, \mu<0$) is designated as a mu-negative (MNG) medium. In certain frequency regimes some gyrotropic materials behave in this manner. For example, ferromagnetic materials exhibit a negative permeability in the very high frequency (VHF) and ultra high frequency (UHF) regimes.

Metamaterials can be broadly categorised into two types.[3] The first type of metamaterials could mimic the properties of natural materials but with superior efficiency compared with those found in nature. For example, these nanostructured materials could show enhancement of electromagnetic response by artificially including highly conductive fillers, more insulative components, or designed chirality, or larger values of other material parameters. The other type of metamaterials exhibit

entirely new properties with no analog in conventional materials, such as negative or extreme permittivity and permeability.

Metamaterials composed of designed inclusions may exhibit exotic and unique electromagnetic properties that might enable the construction of novel devices and use in diverse applications such as superlensing, biosensors, cloaking, conformal antennas and other flat electromagnetic lens devices.

2.1.1.1 Superlens

A superlens (or perfect lens) is a slab of negative-index material that could compensate for wave decay and allow imaging of details beyond the diffraction limit without the usual constraints imposed by wavelength.[7,8] Unlike conventional positive-index lenses that require a curved surface to bend and focus the rays emanating from an object to produce an image, the planar superlens with negative refraction index diverges rays from an object and refracts the rays at the front surface of the lens, reversing their trajectories to focus within the lens. Again, the rays diverge from this focus and are negatively refracted at the back surface and to converge to form a second image outside the lens,[7] as demonstrated in Fig. 2.2. Superlenses could be used in the microchip industry to decrease the optical lithography limit, or the superlenses could be used in more precise medical imaging systems.

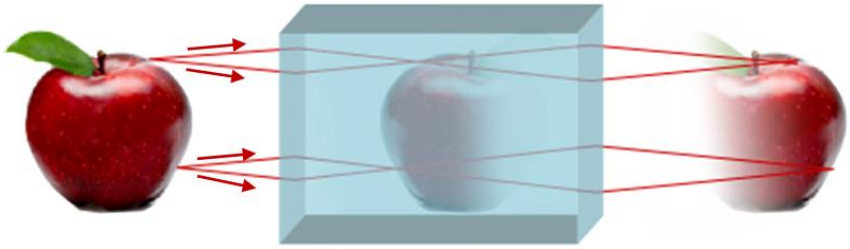

FIG. 2.2. A rectangular slab of negative-index material is shown with rays (red lines) from a nearby object incident upon it. The rays are refracted twice at the interfaces between air and the slab, governing by Snell's law but with negative diffraction index, and finally form an image outside the lens (right). For some metamaterials, the image could show details finer than the wavelength of the electromagnetic wave used. Redrawn from [9].

2.1.1.2 Biosensor

Metamaterials can exhibit a strong localization and enhancement of fields based on plasmon-mediated interactions between the inclusions so that they can be more sensitive to detect nonlinear substances and hence improve the sensor selectivity.[10,11] The nonlinear substances refer to those whose macroscopic electromagnetic properties have nonlinear relations between their electric displacement *D* and electric filed *E*, and/or between magnetic flux density *B* and magnetic field strength *H*. Surface plasmons occur at the interfaces of metals and dielectrics and are extremely sensitive to the refractive index of the dielectric media. Sensors can be conceived composing a nanoporous dielectric matrix and receptor functionalised inclusions, which would

allow analytes to diffuse in and bind with the receptors, leading to a refractive index change upon binding.[10]

2.1.1.3 Cloaking

Metamaterials to control electromagnetic fields have been proposed to provide invisibility cloaking devices.[12],[13] The cloaking materials are theoretically designed and engineered with the necessary special radiation in finite local permittivity and permeability values so that electromagnetic waves can be bent around an object without scattering and reflections, as if nothing were there. Although this remains a long term concept, more recent advances have been made experimentally in both the optical and microwave regime.[14 -17]

2.1.2 Spatial Transformation Technique

Spatial transformation of electromagnetic materials allows a practical approach to manipulate waves in unprecedented ways by carefully adjusting the material parameters of space. This technique provides theoretical support for metamaterials design and provides a framework to how to design novel devices.

We can use a Cartesian coordinate system (x, y, z) to describe a 3D volume space, and a distorted coordinate system (x', y', z') to describe a second volume. The two

coordinate systems are correlated through the transformation functions x’ = x’(x, y, z), y’ = y’(x, y, z), z’ = z’(x, y, z). Now, assume an incident electromagnetic wave travels along a path in both coordinate systems. Its path should be a straight line in the Cartesian coordinate and is distorted according to the mesh defined in the distorted coordinate. The distorted system will no longer hold isotropic and homogeneous properties after coordinate transformation from a Cartesian coordinate system. The distribution profiles of electromagnetic parameters (e.g. permittivity and permeability) are derived mathematically from the Maxwell’s equation and the coordinate transformation function between the two systems.[12],[14] In practical applications, the propagation path of a travelling electromagnetic wave can be first theoretically designed, and a medium with the necessary parameters is subsequently engineered to achieve the specific behaviour. For example, in Fig. 2.3(a) the incoming wave will impinge on the object, but will avoid it [Fig. 2.3(b)] in a distorted space generated by the appropriate tuning of the material parameters.[14]

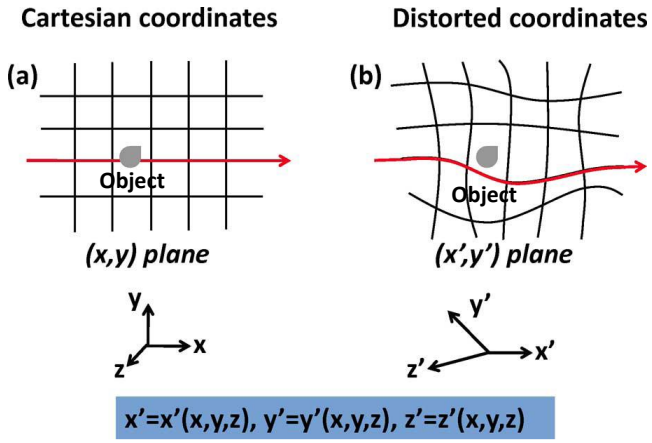

FIG. 2.3. Two coordinate systems: (a) the Cartesian coordinate and (b) the distorted coordinate. The incident wave travels smoothly around the gray object in the distorted coordinate. Taken from [14].

A physical explanation of the cloaking behaviour originating from electromagnetic transformation can be described by analogy with the well-known optical mirage effect, in which the light rays are bent towards increasing refractive index gradient caused by air density. Similarly, in the present example the electromagnetic wave traversing a cloak tends to bent towards the higher refractive index region.[18,19] Based on spatial transformation theory and simulation, Hao's group at Queen Mary University of London reported the first cloaking structure made of a high-ε dielectric-loaded foam mixture, which was demonstrated to work for all incident angles over a wide range of microwave frequencies.[15] The cloaking material was segmented into a number of small blocks whose dimensions were comparable to the wavelength. These blocks had a finite, different permittivities. Polyurethane was chosen as a low-ε foam matrix, and different ratios of the high-ε barium titanate ($BaTiO_3$) were introduced as inclusions into the composite to produce the required range of permittivities according to spatial transformation theory.

By extending the cloaking principle in a reverse process such that the distorted coordinate system in the virtual space is transferred into an orthogonal coordinate system in physical space, it has also been shown that many curved devices in antenna systems, can be designed into more convenient flat shapes but still operate in the same manner.[14] In the virtual space which is described by a distorted coordinate system, the devices perceived by the electromagnetic wave have curved edges, homogeneous and isotropic material parameters. The physical space where the devices have flat edges,

inhomogeneous and anisotropic material parameters is mapped from the distorted coordinate system using appropriate transformations, and is described by an orthogonal coordinate system (as shown in Fig. 2.4). This method has been used to successfully design a flat reflector and a flat focusing lens.[14] Finite-Difference Time-Domain simulations have also been used to demonstrate good agreement between the performance of the transformed devices and that of their conventional curved-shaped counterparts.[14]

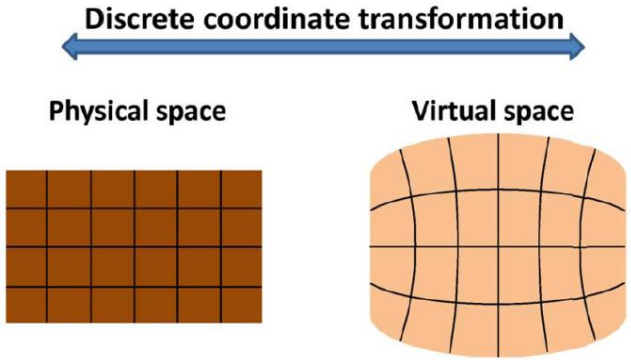

FIG. 2.4. A discrete coordinate transformation is applied to map between physical space and virtual space. Instead of using a continuous transformation function, the discrete transformation maps between distorted cell and orthogonal cell by choosing a proper grid in space. Taken from [14].

2.2 Macroscopic Electromagnetic Parameters: Permittivity and Permeability

2.2.1 Permittivity

2.2.1.1 Definitions and General Relations of Dielectrics

A dielectric is effectively an electrical insulator that can be polarized when exposed to an electric field. Permittivity is a measure of how easily the dielectric can be polarized by the applied electric field and relates to the ability that the material allows the field to transmit.[20] There are various types of charges in the dielectric, as shown in Fig. 2.5.

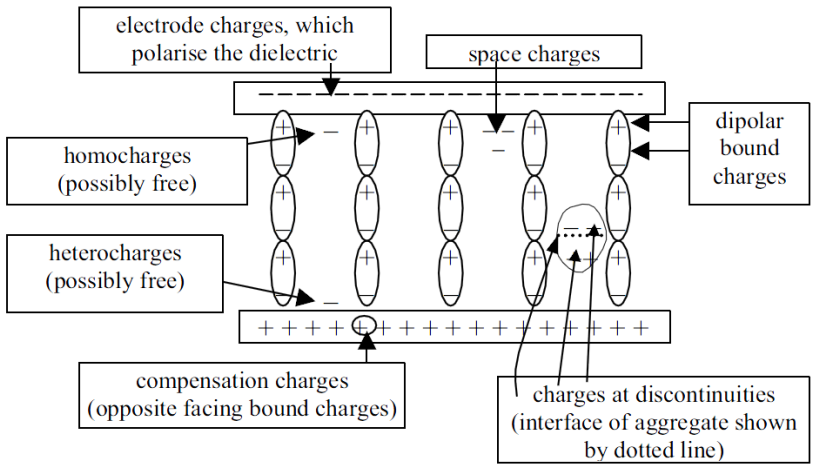

FIG. 2.5 Different types of charge that can be found in dielectrics. Taken from [21].

An applied electric field may induce dipoles that do not exist without a field in the material (e.g. in single atoms or covalent bonded crystals like Si), or/and may change the distribution of existing dipoles trying to align them (e.g. in ionic crystals or H_2O). The dipolar moment $d\vec{\mu}$ is defined by:

$$d\vec{\mu} = qd\vec{l} \tag{2.3}$$

where q is the negative or positive charge value bounded to an electric dipole and $d\vec{l}$ is a vector pointing from the negative to the positive charge. Therefore, the polarization $\vec{P}$ of the material [Eq. (2.4)] is also a vector pointing from the negative to the positive charge.[21] $\vec{P}$ can be defined as the dipole moment per unit volume V.

$$\vec{P} = \frac{\sum \vec{\mu}}{V} = <\vec{\mu}> \cdot N_V \tag{2.4}$$

where $<\vec{\mu}>$ is the average vector dipole moment, N_V is dipole density. Thus the polarization has the physical unit of C/m^2 and is equal to the charge per unit area on the surface of a polarized dielectric. If the dipole moment vectors are randomly orientated, the polarization which depends on the vector sum of all dipole moments is zero. There is a linear relationship between $\vec{P}$ and the applied electric field $\vec{E}$.[20]

$$\vec{P} = \varepsilon_0 \cdot \chi \cdot \vec{E} \tag{2.5}$$

where the proportionality constants are vacuum permittivity ε_0 and dielectric susceptibility χ. It is important to note that this is an empirical relation. In order to make relation with the quantities that are often used in Maxwell's equations, a

connection between the polarization $\vec{P}$ and the electrical displacement $\vec{D}$ needs to be made.[20] $\vec{D}$ is the electric displacement or the electric flux density which is defined as:

$$\vec{D} = \varepsilon_r \cdot \varepsilon_0 \cdot \vec{E} \tag{2.6}$$

and ε_r is the relative permittivity or called dielectric constant of the material, which is the ratio of a material's permittivity to vacuum permittivity. $\vec{D}$ can be considered to be the flux acting inside the dielectric by summing the displacement $\vec{D}_0$ in vacuum and the polarization $\vec{P}$ of the material.

$$\vec{D} = \vec{D}_0 + \vec{P} = \varepsilon_0 \cdot \vec{E} + \vec{P} \tag{2.7}$$

by substituting $\vec{D}$ and $\vec{P}$ with ε_r and χ into Eq. (2.7),

$$\varepsilon_r = 1 + \chi \tag{2.8}$$

ε_r and χ depend on the frequency, temperature and structure of the material.

Polarization mechanisms correspond to the responses of atoms and molecules to an applied electric field leading to the formation and orientation of dipoles. There are four essential types of polarization mechanisms as shown schematically in Fig. 2.6.

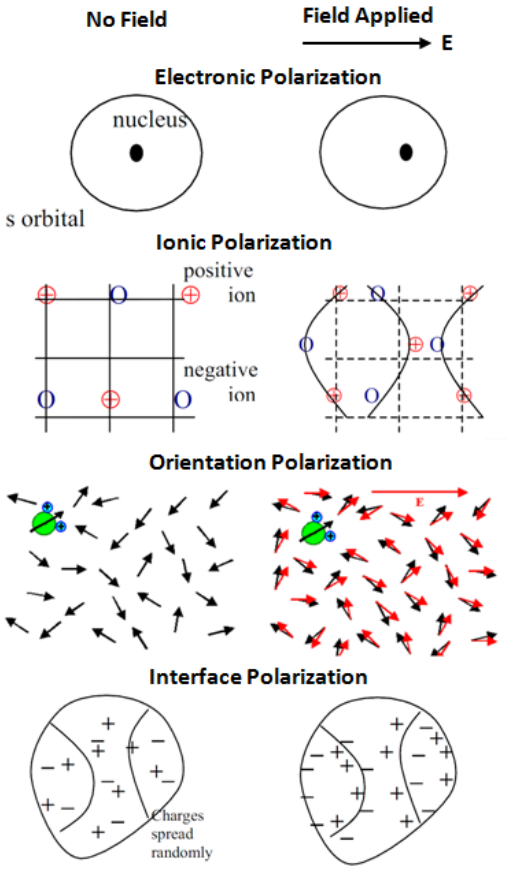

FIG. 2.6. Schematic of four essential types of polarization mechanisms. The arrows in orientation polarization mechanism indicate the directions of molecular electric diploe. A net dipole moment can be produced in the material with an externally applied field. Redrawn from[21].

2.2.1.2 Frequency Dependence of the Relative Permittivity

In all polarization mechanisms, mass movements are involved in response to an electric field, which means the mechanical response to an electric field must be frequency dependent. If the field frequency is so high that no mechanical system is able to follow, the relative permittivity will approach 1 as there is no polarization response at all. It is well known that the index of refraction is given by $\varepsilon_r^{1/2}$ [refer to Eq. (2.2)] if there is no magnetic component. As a result, there are no X-ray microscopes with lenses because no materials have relative permittivity larger than 1 for the frequencies of X-rays (3×10^{16} - 3×10^{19} Hz).

There are only two characteristic physical systems governing the movement of charged masses in experiencing alternating fields.[20] In the cases of electronic and ionic polarization, there is always a restoring force that is proportional to the distance between the dipole charges involved, acting as an oscillating system with a linear force law and some damping. Resonance is the characteristic physical property of such oscillating system.

The general dielectric functions of real ε' and imaginary ε'' permittivity for resonant polarization systems are given:

$$\varepsilon' = \varepsilon_0 + \frac{N \cdot q^2}{m}\left(\frac{\omega_0^2 - \omega^2}{\left(\omega_0^2 - \omega^2\right)^2 + k_F^2 \cdot \omega^2}\right) \tag{2.9a}$$

$$\varepsilon'' = \frac{N \cdot q^2}{m}\left(\frac{k_F \cdot \omega}{\left(\omega_0^2 - \omega^2\right)^2 + k_F^2 \cdot \omega^2}\right) \tag{2.9b}$$

Where m is the masses of the oscillating charges; N is the charge density; ω_0 is the resonance frequency; ω is the applied electric field frequency; k_F is the damping constant, which is only important around the resonance frequency, describing the time for energy dispersion from a single oscillating unit to the whole lattice.

In the case of orientation polarization, there is no restoring force directly acting on the dipoles. Instead, the system can always find an equilibrium state within some characteristic time in response to the alternating field. Hence, the relaxation time τ is the characteristic physical property of such a system instead of a resonance frequency.[20] The typical relaxation time is around 10^{-11} s corresponding to the GHz region.

The dielectric functions of real and imaginary permittivity for dipole polarization mechanism are given by:

$$\varepsilon' = \varepsilon_\infty + \frac{\varepsilon_s - \varepsilon_\infty}{1 + (\omega/\omega_0)^2} \tag{2.10a}$$

$$\varepsilon'' = \frac{(\omega/\omega_0)(\varepsilon_s - \varepsilon_\infty)}{1 + (\omega/\omega_0)^2} \tag{2.10b}$$

where ε_s is the static permittivity at zero frequency, and ε_∞ is the permittivity value for infinite frequency which is equal to 1 by definition.

Unlike last three polarization mechanisms, interface polarization is not amenable to basic considerations and calculations. There is no general way to calculate the charges on interfaces (e.g. grain boundaries, surface of precipitates, etc.) nor their contribution to the total polarization of a material.[20]

The frequency dependence of real and imaginary parts of relative permittivity of a material is determined by the superposition of four polarization mechanisms. The following curves (Fig. 2.7) present an ideal case with all mechanisms occurring in their ideal forms.

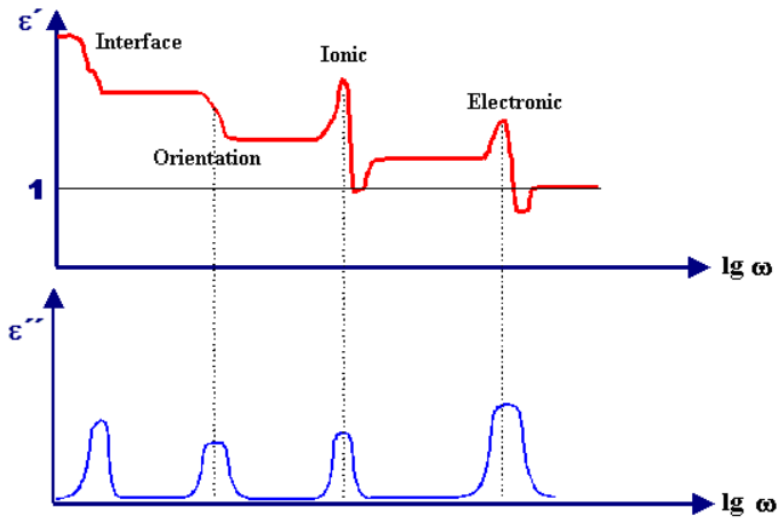

FIG. 2.7. Schematic curves of the real and imaginary parts of the relative permittivity with all polarization mechanisms against applied frequency. Taken from [20].

2.2.1.3 Dielectric Loss

Low dielectric loss is desirable to minimize noise and energy dissipation for microwave devices applications. For an alternating electric field, displacement currents may be generated in dielectrics. The strength of the current *j(ω)* can be expressed as:

$$j(\omega) = \frac{dD}{dt} = \varepsilon(\omega) \cdot \frac{dE}{dt} = \varepsilon(\omega) \cdot \frac{d[E_0 \exp(i\omega t)]}{dt} = \varepsilon(\omega) \cdot i \cdot \omega \cdot E(\omega) \tag{2.11}$$

By substituting the dielectric function into Eq. (2.11):

$$\varepsilon(\omega) = \varepsilon'(\omega) - i \cdot \varepsilon''(\omega) \tag{2.12}$$

$$j(\omega) = \varepsilon''(\omega) \cdot \omega \cdot E(\omega) + \varepsilon'(\omega) \cdot i \cdot \omega \cdot E(\omega) \tag{2.13}$$

where the real part of *j(ω)* in phase is called the active power indicating the power lost as heat, and the imaginary part of *j(ω)* is 90° out of phase and is called the reactive power, which can be recovered each cycle.

The dielectric loss tan δ is defined as a ratio of the active power to the reactive power, which is a quality measure of a dielectric.[21] tan δ can be simply expressed as:

$$\tan\delta = \frac{\varepsilon''}{\varepsilon'} \tag{2.14}$$

2.2.2 Permeability

2.2.2.1 Definitions and General Relations of Magnetics

Magnetism is a property of materials that can respond to an applied magnetic field. The obvious difference between dielectric and magnetic phenomena is that there are no magnetic monopoles in magnetic materials. The relation between the magnetic flux density $\vec{B}$ and the magnetic field strength $\vec{H}$ in vacuum comes from the Maxwell equation:

$$\vec{B} = \mu_0 \cdot \vec{H} \tag{2.15}$$

in which $\mu_0 = 4\pi \times 10^{-7}$ Hm^{-1} is the magnetic permeability of vacuum. If a material is present, the Eq. (2.15) becomes,

$$\vec{B} = \mu_0 \cdot \mu_r \cdot \vec{H} \tag{2.16}$$

where μ_r is the relative permeability of the material, which is a dimensionless number.

Accordingly, the magnetic flux density $\vec{B}$ in the presence of a material can be split into the contributions of the vacuum and the material, which is expressed as

$$\vec{B} = \mu_0 \cdot \vec{H} + \vec{J} \tag{2.17}$$

or

$$\vec{B} = \mu_0 \cdot (\vec{H} + \vec{M}) \tag{2.18}$$

where $\vec{J}$ is the magnetic polarization of the material, and $\vec{M}$ is the magnetization defined as $\frac{\vec{J}}{\mu_0}$. By substituting Eq. (2.16) into Eq. (2.18), the relation between the magnetization $\vec{M}$ and the magnetic field strength $\vec{H}$ is obtained as

$$\vec{M} = (\mu_r - 1) \cdot \vec{H} \tag{2.19}$$

$$\vec{M} = \chi_m \cdot \vec{H} \tag{2.20}$$

where $\chi_m = (\mu_r - 1)$ is the magnetic susceptibility that describes the degree of the magnetization of a material in response to an applied magnetic field, in analogy to the dielectric susceptibility.

2.2.2.2 Classes of Magnetic Materials

The magnetic moment of an atom originates from the sum of all the orbital and spin moments of all the electrons in the atom. Hence, the magnetic behaviour of a material is determined by its structure and electron configuration. There are five major types of magnetism: diamagnetism, paramagnetism, ferromagnetism, antiferromagnetism, and ferrimagnetism.[22] The first two groups have no collective interaction of atomic magnetic moments and are not magnetically ordered. The last three groups exhibit long-range magnetic order below their critical temperatures.[23] The characteristic curves and temperature dependence of magnetic susceptibilities of the five magnetisms are summarized in Table 2.1.

Table 2.1. Summary of the characteristic curves and temperature dependence of magnetic susceptibilities of the five types of magnetism. Redrawn from [20].

Magnetization M=M(H)	**Magnetic susceptibility** $\chi_m = \chi_m(T)$	
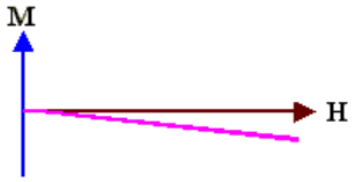	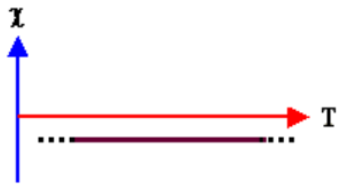	**Diamagnetism**: The susceptibility is negative and close to zero. There is no temperature dependence.
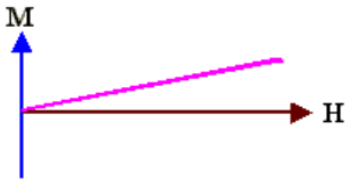	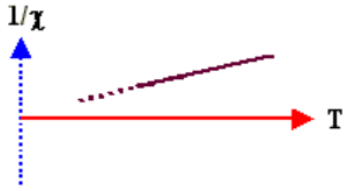	**Paramagnetism**: The susceptibility is barely larger than zero and decrease with temperature.
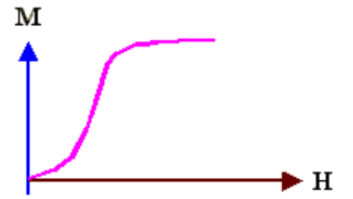	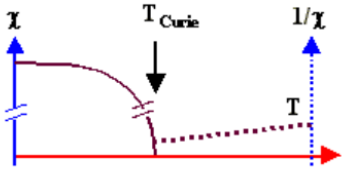	**Ferromagnetism**: The susceptibility is large. Paramagnetic behavior is observed above the Curie temperature.
	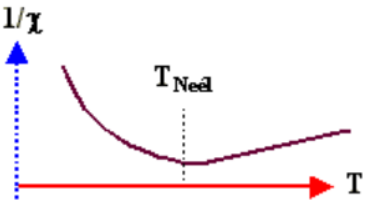	**Antiferromagnetism**: The susceptiblity is small but temperature dependent below Néel temperature. Paramagnetic behavior is observed above the Néel temperature.
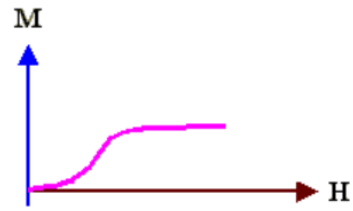	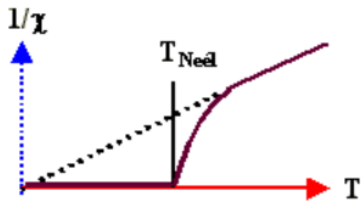	**Ferrimagnetism**: The behavior is much like ferromagnetism but smaller tendency. The 1/χ(T) is very close to zero below the Néel temperature.

2.2.2.3 Magnetics Loss and Frequency Behaviour

Consider a ferromagnetic material exposed to an oscillating magnetic field. Assume the field frequency is low so that the internal magnetization of the material is able to instantaneously follow. There are two main independent mechanisms which cause magnetic losses: eddy current loss P_{eddy} and hysteresis loss P_{hyst}.[20] Different from dielectrics, ferromagnetic materials are mostly conductive so that currents can be induced, known as eddy currents, in the material by the oscillating magnetic field. On the other hand, the movement of domain walls also involves loss of energy which is considered as intrinsic magnetic losses or hysteresis loss. Both energy losses are converted into heat. The total ferromagnetic loss P_{Fe} per unit volume of the material can be estimated as:

$$P_{Fe} \approx P_{eddy} + P_{hyst} \approx \pi \cdot \frac{d}{6\rho} \cdot (f \cdot \vec{B}_{\max})^2 + 2f \cdot \vec{H}_c \cdot \vec{B}_{\max} \qquad (2.21)$$

where d is the thickness of the material perpendicular to the field direction; the conductivity $\sigma = 1/\rho$ is referring to the eddy current, where ρ is the resistivity; f is the frequency of the magnetic field; $\vec{H}_c$ is the magnetic coercivity; and $\vec{B}_{\max}$ is the maximum magnetic flux in both cases.

To minimize the eddy current losses, a material with a high resistivity should be chosen. To make d smaller, the ferromagnetic material can be designed as composing of a stack of stacked insulated thin sheets.[20] For a certain material with a given hysteresis curve,

its hysteresis loss is fixed. The area inside the hysteresis curve can be roughly represented by the term $\vec{H}_c \cdot \vec{B}_{\max}$.

The frequency response of ferromagnetic materials is determined by the movement of domain walls in response to an oscillating magnetic field. For materials with a large coercivity, strong forces are needed to move domain walls and it will be hard to move them fast. Even for materials with low coercivity, they are not able to response to large frequencies, e.g. in the optical range. There is no general formula to express the frequency dependence of domain wall movements, but it has been obtained for some specific magnetic materials.

2.3 Design and Manufacture of Metamaterials

2.3.1 Structures of Metamaterials

The unusual electromagnetic properties of metamaterials are determined by their specially designed structures. The structures, such as spilt ring resonators,[5,24,25] S-shape resonators,[26] multilevel dendritic structures,[27] nano-apertures[28,29] and metallic nanoclusters[30] have been designed by physicists and electrical engineers to achieve negative permittivity and negative permeability. In this sub-section, some of these structures are introduced.

2.3.1.1 Split Ring Resonator

The split ring resonator (SRR) has been typically used to achieve a magnetic response first proposed by Pendry in 1999.[31] The SRR consists of a planar set of conducting concentric rings with a gap on each ring, as shown in Fig. 2.8(a). An effective magnetic material can be formed by arranging these SRR elements in an array [Fig. 2.8(b)].

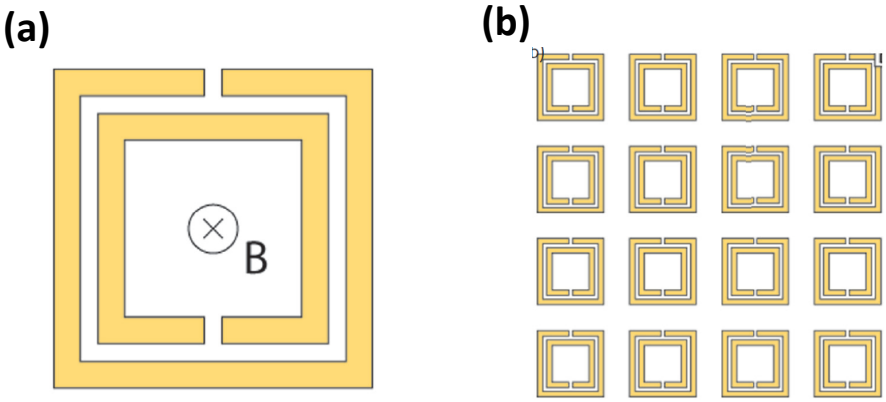

FIG. 2.8 (a) an SRR with an external magnetic field incident upon it. (b) an effective magnetic material is formed by arranging SRR into an array. Taken from [24].

According to Faraday's law, circulating current can be induced when a time varying magnetic field is applied perpendicular to the plane of the SRRs. The charges resulted from the circulating current are then built up across the split gaps in the SRR. The gaps can be thought of as capacitances. Thus, the SRR can be viewed as a LC circuit, where the inductance comes from the current path of the SRR. As the frequency of the magnetic field increased above the SRR resonant frequency $\omega_0 \sim \sqrt{1/LC}$, the currents can no longer keep up and eventually this result in a "negative response" which implies

an effective negative μ has been induced.[24] It is known that any metal has a negative value of ε below its plasma frequency, and can be achieved by interleaving the SRR lattice with a lattice of conducting wires.[32] This "composite" can then be designed to have an overlapping frequency region where both ε and μ are negative by carefully choosing the parameters of the wire lattice.

In 2000 Smith *et al* [5] fabricated a negative index material by combining a wire structure and an SRR structure. This preliminary experiment showed that Veselago's hypothesis could be realized. The first demonstration and confirmation of negative refraction was given by Shelby *et al*.[6] only as recently as 2011, as shown in Fig 2.9.

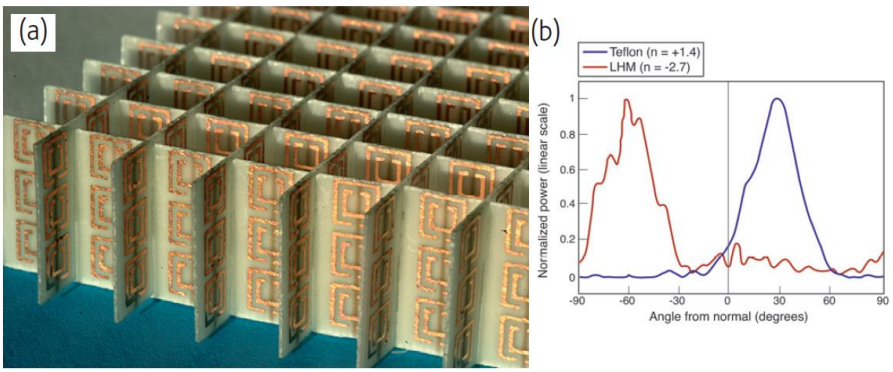

FIG. 2.9 (a) A negative index metamaterial was formed by combining SRRs and wires which were lithographically deposited on opposite sides of standard circuit board. The height of the structure is 1 cm (b) The power detected as a function of angle in a Snell's law experiment performed on a Teflon sample (blue curve) and a negative index sample (red curve). Taken from [24].

However, the effect began to fail for increasing frequencies somewhere around the optical range. There are two main limitations. Firstly, the cell-size to wavelength

parameter is no longer satisfying $a/\lambda_0 << 1$ in the visible frequency regime. Secondly, the metals lose their metallic free-electron like properties and thus their conductivity at optical and ultraviolet wavelengths. The effective magnetic response of the SRR cannot be exhibited without macroscopically circulating currents.[24]

2.3.1.2 Conducting Nanowire Media

In the case of an array of SRRs, the negative refraction is constrained in two dimensions and is limited to a narrow band of frequencies. Resonance losses and fabrication difficulties are major challenges to realize bulk metamaterials with a negative refractive index for visible light. In recent theoretical studies, metamaterials consisting of metal nanowire arrays could exhibit negative refraction for a broad frequency band for all incident angles and the material loss was suggested to be much lower than traditional metamaterials with similar functionality.[33,34] Then, assemblies of metallic nanowires in a dielectric matrix have been considered. An array of parallel metal nanowires, such as Au and Ag, embedded vertically in an aluminium oxide nanotemplate was fabricated and demonstrated negative refraction in the optical range,[35,36] as shown in Fig 2.10. Nanoporous aluminium oxide templates were first generated by electrochemical anodization, into which nanowires were then synthesized by means of AC electro-depositon.[35]

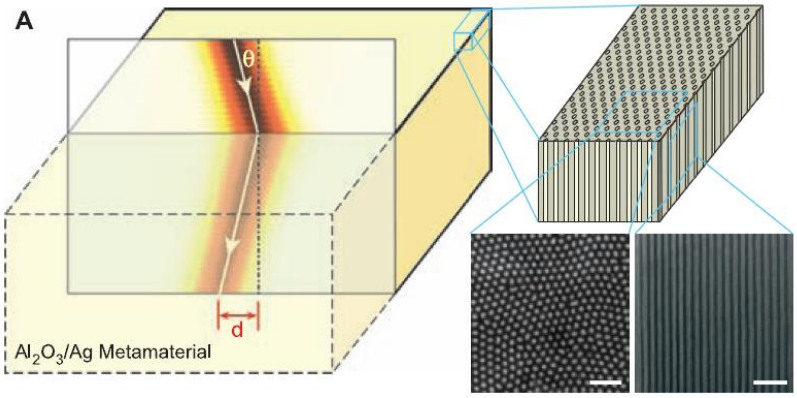

FIG. 2.10 (Left) Schematic of negative refraction from air into the Al_2O_3/Ag nanowire metamaterials at visible frequencies. (Right) Ag nanowires embedded vertically in an alumina matrix. The scanning electron microscopy (SEM) images showing the top and side view of the nanowires (60 nm wire diameter and 110 nm center-to-center distance). The scale bars indicate 500 nm. Taken from [36].

The negative refraction behaviour results from the plasmon resonance between the pairs of nanowires for electromagnetic fields. The refractive index is negative above the resonance frequency. The metamaterial can be viewed as an optical LC-circuit, where the metal nanowires act as inductive elements and the dielectric gaps perform as capacitive elements. It was demonstrated that the position and intensity of the resonance peak were dependent on the composite dimensions, filling level and the angle of incidence and polarization direction.[35]

2.3.1.3 Fishnet and Swiss-cross Structures

Recent theoretical studies suggested that stacking up multiple metallic strips oriented along the direction of magnetic field vertically separated by dielectric layers can exhibit a magnetic resonance with a negative permeability over a limited frequency range.[37,38] The effective plasma frequency of the structure could be manipulated by adding an array of metallic strips along the direction of electric field to this magnetic structure resulting in a metal-dielectric-metal sequence formed a fishnet structure as a whole, as shown in Fig. 2.11. Carefully choosing the lattice parameters and the hole size so that the effective plasma frequency was above the magnetic resonant frequency leads to a superimposed region where both permittivity and permeability of the structure were negative in a certain frequency band.[39]

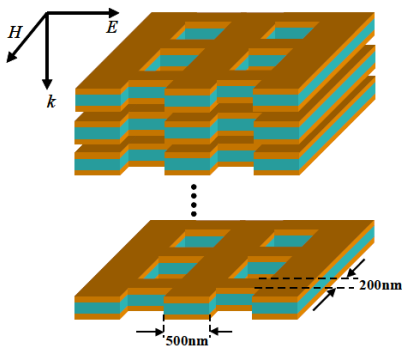

FIG. 2.11 Schematic of a metal-dielectric-metal sequence of fishnet structure. Taken from [39].

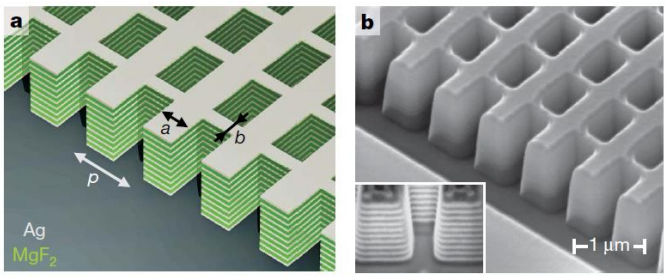

FIG. 2.12 (a) Schematic of the 21-layer Ag/MgF_2 fishnet structure with parameters of p = 860 nm, a =565 nm and B= 265 nm. (b) SEM image of the fishnet structure with alternating layers of 20 nm Ag and 50 nm MgF_2. Taken from [40].

The first fishnet metamaterial consisting 21 alternating films of Ag and MgF_2 (10 functional layers) was fabricated by using focused ion-beam milling (FIB) in Zhang's group at University of California, Berkeley,[40] as shown in Fig 2.12. The simulation predicted broad negative-index band from 1.45 μm to 2.2 μm wavelength could be achieved and a refractive index of -1.23 at 1775 nm was confirmed by experiment.

A drawback of the fishnet structure is that the effective optical parameters depend on the incident polarization. A new structure of Swiss Cross pattern was theoretically and experimentally realized aimed at eliminating the shortcoming of polarization dependence for negative refraction metamaterials.[41] The proposed structure was comprised of Au-MgO-Au three layer stacking in the vertical direction on a glass substrate. The Swiss Cross patterns were achieved by an e-beam-lithography and lift-off technique. A schematic of the geometry and SEM image are shown in Fig. 2.13. An effective index of refraction of n = -1.9 at 1400 nm wavelength was confirmed by experiment.[41]

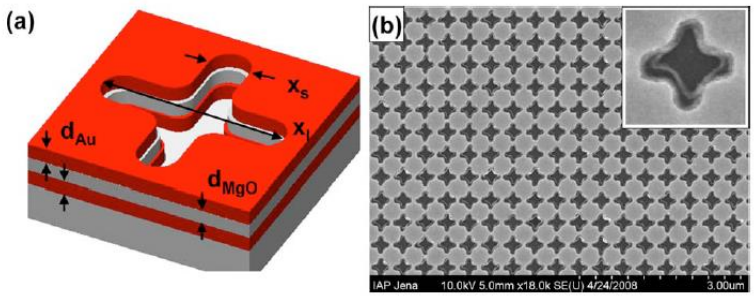

FIG. 2.13 (a) Schematic of the Swiss cross structure with alternating layers of 30 nm Au and 37.5 nm MgO. The parameters of x_l = 310 nm and x_s =80 nm. (b) Top view SEM image of the Swiss cross structure with a lattice constant of 410 nm. Taken from[41].

2.3.1.4 Nanostructured Composite Metamaterials

In the above artificially patterned structures, resonance was considered to be the main mechanism to realize the unusual electromagnetic properties of metamaterials. Recently, it has been demonstrated that metamaterials can be achieved by arranging 'natural' materials in particular shapes or combinations, such as magnetodielectric spherical particles,[42] superlattices of natural materials,[43] and uniaxial crystals.[44] Research has focused on metals and ceramics that can realize negative or desired values of permittivity and permeability under certain conditions. In particular, ferromagnetic materials have received considerable interests in the realization of metamaterials, because of the resultant negative permeability of some ferromagnetic metals and metallic alloys in the vicinity of the ferromagnetic resonance frequency as well as negative permittivity of metallic materials below their plasma frequency.[45 - 47]

A design of metamaterials has been proposed based on periodically arranged noble metal nanoinclusions, such as Ag or Au, on two different length scales in a host dielectric.[48,49] The effective permittivity of the medium can be altered on the first length scale, and the effective permeability of the medium can be modified on the second length scale. Simulations based on the finite-difference time-domain (FDTD) method showed that for certain combinations of the inclusion size and the wavelength, the real part of the effective permittivity is negative, but positive for other combinations. Use of nonmagnetic coated $LiTaO_3$ spheres in a lattice has also been reported to provide a medium with both effective materials parameters exhibiting resonance in the same spectral domain, thus realising a negative index material at infrared frequencies.[50]

2.3.2 Manufacturing Technologies

Metamaterials have mostly been manufactured by top down technologies such as e-beam lithography or focused ion bean patterning.[36,40,51,52] Nanoimprint lithography has also been used to fabricate the state-of-the-art fishnet and Swiss-cross metamaterials in a relative quick and cheap way, at up to 0.9 × 0.9 cm^2 in dimension.[53] Other techniques, such as atomic layer deposition (ALD),[54] electrochemical deposition,[55] magnetron sputtering[56] and etc., have all seen used for metamaterials fabrication. However, these techniques have the disadvantage of being expensive and obtaining large areas and three dimensional arrangements is difficult. Moreover, by far the most work has been applied to the optical dimension with comparatively little attention on the microwave domain, where applications require larger length-scale variations.

Self-assembly and chemical approaches have been used to manipulate nanocrystals into close-packed, glassy, and ordered assemblies by slowly destabilizing a colloidal dispersion.[57] However, this technique requires a monodisperse distribution of nanoparticles and the process is slow.[58] Novel technologies, such as protein-guided assembly of nanostructures, have been explored for the fabrication of truly 3D magnetic nanostructures. For the protein crystallization technique, nanoparticles with the desired function are synthesized inside protein molecules whose shells are used as nanoreactors.[59] Then, the protein is crystallized to form the desired array structure. The periodicity and symmetry of the array is controlled by the protein type, size, chemistry, etc. Self-assembled gyroid metamaterials have also been demonstrated to show superior optical properties by replacing a block copolymer self-assembled morphology into plasmonic materials, such as Au[60] and TiN.[61] A range of architectures of the mesoscopic unit cell can be controlled by varying the molecular weight of the structure-forming block polymers, and the optical behavior of the formed gyroid metamaterials can be tuned accordingly.[60]

The weight, shape-flexibility and the ease of processing are key factors for metamaterials application. Hence, many research efforts have focused on polymer composites that can be cheaply and easily processed in bulk. The conventional techniques of forming composites by blending particles into polymers, such as extrusion, casting, spin-coating and etc., have all been employed to fabricate metamaterials based on polymeric composites.

In the extrusion process, the energy consumption should increase with increasing filler loadings as ceramic content is absorbing part of the applied heat, and the processing time should also increase to allow adequate mixing time to achieve homogeneous dispersion of the fillers throughout the composites. Amorphous alloy-epoxy composite samples were produced by directly mixing $Fe_{78.4}Si_{12}B_{9.6}$ amorphous alloy powders into an epoxy resin, and then the electromagnetic properties of the composites were studied by varying the particle size and fraction.[62] Another technique, melt blending, was also proposed to process nanocomposites with embedded Fe nanoparticles.[63] Melt blending is a cost-effective technique used in industry that gives an intimate mixing of the additive into the polymeric matrix, for example, Fe nanoparticles were melt blended into methyl methacrylate (MMA) monomer at 210 °C.

In order to control the particle size and distribution within the polymer matrix, a method of *in-situ* seed-mediated growth of magnetite Fe_3O_4 nanoparticles in a block copolymer has been demonstrated.[64] In this case, [styrene-b-ethylene/butylene-b-styrene] (SEBS) was used as a matrix for the templating of the seeds of Fe_3O_4 nanoparticles. The concentration ratio of surfactant to iron-precursor was adjusted to control the nucleation and growth of Fe_3O_4 nanoparticles *in-situ*.

2.4 Metamaterials Based on Polymer/filler Composites for Electromagnetic Applications

Practical applications aspire to large-scale, simple, cheap, deformable and efficiently processable metamaterials. For the above reasons, polymeric based metamaterials are compelling as they may have advantage over precisely designed patterns, or metal and ceramic based materials. For microwave applications with wavelengths of centimetres or longer, precise micron/nano-resolution control of the microstructure is also unlikely to be necessary. The desired macroscopic electromagnetic parameters of the metamaterials are caused by inclusions or "fillers", and the polymers involved are used as "inert" insulating hosts. In this section, manipulation of permittivity and permeability by this type of composite are discussed.

2.4.1 Mixing Rules for Composites

To predict the approximate dielectric (ε_{com}) or magnetic (μ_{com}) properties of composite mixtures without having to consider microscopic fields, macroscopic mixing rules have been developed, and the most widely validated and employed are those due to Lichtenecker,[65-68] Maxwell–Garnett,[69] and Bruggeman.[70-72] The logarithmic Lichtenecker mixing rule is given by,

$$\log \varepsilon_{com} = (1 - f) \log \varepsilon_m + f \log \varepsilon_f \qquad (2.22)$$

where f is the volume fraction of the filler; ε_m and ε_f are the relative permittivites of the polymer matrix and the filler, respectively. The formula has proven to be a useful practical formulation for determining the effective permittivity and permeability of composite media. It has long been regarded as semi-empirical in nature, although recently was derived from Maxwell's equations by Simpkin.[73]

The Maxwell–Garnett equation [Eq. (2.23)] and Bruggeman's [Eq. (2.24)] effective medium theory are two mixing rules that are also frequently used:

$$\varepsilon_{com} = \varepsilon_m + 3f\varepsilon_m \frac{\varepsilon_f - \varepsilon_m}{\varepsilon_f + 2\varepsilon_m - f(\varepsilon_f - \varepsilon_m)} \qquad (2.23)$$

$$f\frac{\varepsilon_f - \varepsilon_{com}}{\varepsilon_f + 2\varepsilon_{com}} + (1-f)\frac{\varepsilon_m - \varepsilon_{com}}{\varepsilon_m + 2\varepsilon_{com}} = 0 \qquad (2.24)$$

The Maxwell-Garnett model[69] has been adopted when the isotropic host material contains a collection of spherical, homogeneously distributed inclusions. The Maxwell-Garnett equation is especially suitable for filler loading levels below the percolation threshold, i.e. particles are considered isolated within the host matrix. Bruggeman[70] further extended the mixing equation to a form in which the inclusions no longer serve as mere perturbation to the host but assume both inclusion materials and host matrix as the similarly shaped particles imbedded in an effective medium of the composite, which is more relevant at high loading levels. Another mixing equation [Eq. (2.25a)], which combined the above mixing rules with the characteristics of the Maxwell-Garnett rule at low filling levels yet approaches the Bruggeman equation as the filler loading increases, was introduced recently by Jylhä and Sihvola:[72]

$$\frac{d\varepsilon_{com}}{d\varepsilon_f} = \frac{3\varepsilon_m(\varepsilon_f - \varepsilon_{com})}{\varepsilon_f + 2\varepsilon_{com} - f\varepsilon_{com}} \qquad (2.25a)$$

With the solution for the inverse function $df/d\varepsilon_{com}$ of the differential equation:

$$f = 1 - \frac{1}{3}\frac{\varepsilon_f - \varepsilon_{com}}{\varepsilon_f - \varepsilon_m}\left(2 + \left(\frac{\varepsilon_f - \varepsilon_{com}}{\varepsilon_f - \varepsilon_m}\right)^{\varepsilon_f/\varepsilon_m - 1}\right) \qquad (2.25b)$$

for the condition that $\varepsilon_m < \varepsilon_{com} < \varepsilon_f$.

An effective mixed medium approximation of permeability can also be calculated using the same equations but by replacing the permittivity with permeability.

2.4.2 Composites Comprising Polymers and Inorganic Fillers

The introduction of inorganic particles into the polymer matrix provides the opportunity to produce a composite with desired permittivity and permeability.[74,75] The choice of polymer matrix is manifold, depending on the applications, and can include industrial plastics (nylon 6, polymide, polypropylene), conducting polymers (polypyrrole, polyaniline), and transparent polymers (polymethylmethacrylate, polystyrene). For example, polyphenylene sulfide (PPS) has been chosen as one matrix candidate due to its high melting temperature (280°C) enabling solder joints onto the composite substrate.[76] Cyclic olefin copolymer (COC) with glass-like clarity has been used in optical applications such as medical devices.[76] Frequently used inorganic fillers include metals and metal alloys (Au, Ag, Fe, Pt, CoPt), semiconductors (ZnO, PbS,

CdSe), oxides (ferric oxide), and carbon-based materials (carbon nanotube, graphite, graphene). The electromagnetic properties of the composites are effected by the composing phases and microstructures. Parameters such as size, distribution, shape, as well as the loading levels of the fillers are also very important in determining the properties of the compound.[77]

The optical applications of polymers are limited due to their relatively narrow range of the refractive index, which is typically between 1.3 and 1.7. In contrast, inorganic materials can have refractive index far below 1 (e.g. Au) or above 3 (e.g. PbS).[78] Thus, polymeric composites with more useful variations in refractive index can be achieved by introducing inorganic nanoparticles into a polymer matrix. A refractive index of 2.5-3.2 was obtained for a polymeric composite with additives of PbS, silicon, or iron sulphide. By introducing a ZnS content of 50wt% into poly(N,N-dimethylacrylamide), the refractive index of the nanocomposite was increased from 1.54 to 1.63.[79] An ultralow refractive index of 1 was achieved by the incorporation of 90 wt% Au nanoparticles into gelatine.[80]

2.4.2.1 Dielectric Composites

The dielectric properties of materials can be described by the complex permittivity ($\varepsilon' + i\varepsilon''$) which is related to a variety of physical phenomena and are dependent on frequency. At low frequencies (< 100 MHz), the imaginary part of permittivity ε'' is dominated by the influence of ion conductivity.[81] However, polymer-ceramic

composites exhibit an intrinsic dielectric relaxation that gives rise to dielectric loss at high frequencies, which is a challenge in developing composite structures for high-frequency applications.[82] The permittivity and dielectric loss tangent of composites generally increase with increasing filler loading levels. There have been attempts to develop and produce composites with high relative permittivity and low losses with different combinations and structures. For example, in a 60 vol.% BiO_2-ZnO-Nb_2O_5 – 40 vol.% polytetrafluoroethylene (PTFE) composite, a relative permittivity of 12.5 and dielectric loss of 0.001 at 800 MHz has been reported;[83] While for a $Ba_{0.55}Sr_{0.45}Ti_{1.01}O_3$ (BST) /polyphenylene sulphide (PPS) composites with 70 vol.% loading, a relative permittivity of 13.5 with dielectric loss of 0.0025 at 1GHz was obtained.[84] For BST/ polypropylene-graft-poly(styrene-stat-divelbenzen) (ER140) composites with 37 vol.% loading, a relative permittivity of 15 with a dielectric loss tangent of 0.008 was achieved at 1 GHz.[76]

Ferroelectric ceramic materials such as $BaTiO_3$, $Pb(Zr,Ti)O_3$ (PZT), $Pb(Mg_{1/3}Nb_{2/3})O_3$ (PMNT) and $PtTiO_3$ have been widely used as fillers in dielectric composites due to their high inherent permittivities. Polymer-ceramic composites with increased permittivity and sufficiently low loss were demonstrated for microwave applications such as patch antenna and coupled line filters.[85] For example, $BaTiO_3$ (BT), Bi-Ba-Nd-Titanate (BBNT), and Mg-Ca-Ti (MCT) powders were chosen as fillers to disperse into a polydimethylsiloxane (PDMS) polymer matrix which is pliable and thermally stable. A high relative permittivity up to ε_r = 20 with losses of tan δ < 0.04 were obtained for a 25% BT volume mixture in the measured window 100 MHz – 1 GHz.

MCT/PDMS and BBNT/PDMS 25% mixtures exhibited low losses, tan $\delta < 0.009$, but lower dielectric permittivities of $\varepsilon_r < 8.5$.[85]

Negative permittivity is one of the key parameters for realizing left-handed metamaterials (LHMs). It has been reported that negative permittivity can be obtained from a polyetherimide(PEI)/polyimide (PI) nanocomposite filled with carbon nanofibers (CNFs) in the frequency range of 0.1 kHz – 3 MHz.[86] The negative permittivity was dependent on the CNF fraction, aspect ratio and the chemical structures of the polymer matrix materials. This negative permittivity behaviour was supposed to be owing to the CNFs forming a 3D network which is equivalent to the thin metallic wires in Pendry's studies.[32] Such systems are, however, expected to be very lossy for real applications.

The dielectric properties of composites not only depend on the physical properties of both filler and polymer, but also the interactions that take place at the interface between filler and polymer. Thus, the morphology of the filler can be important.[87] For example, radial ZnO nanowires were grown on hexagonal prism tips forming nanowire clusters,[88] and in a poly(vinylidene fluoride) (PVDF) matrix showed a high relative permittivity > 100 at comparatively low filler content.[88]

The efficiency of nanoadditives to enhance the dielectric properties of high frequency composites without increasing filler loading has been investigated.[89] A small addition (1-6 vol.%) of nanoadditives such as nanosize conductive (Ag), semiconductive (Si)

and dielectric (Al_2O_3) were added into the composites as a third phase, where the first and second phases refer to the polymer matrix and primary fillers. These polymer composites showed a significant increase of relative permittivity with all nanoadditives but the dielectric losses and frequency dispersion levels remained similar to those of the polymer without nanoadditives. In such cases, the enhancement of the permittivity was suggested to be primarily due to the higher permittivity values of the nanoadditives, and secondly because of the improved coupling of the matrix and primary particles.[89] The relative permittivity of a ceramic-metal (BST+BCB-Ag) composite was increased from 50 to 450 by changing the volume fraction of Ag from 0 to 0.14.[90] The effect of nanoadditives was also studied in polymer-ceramic composites, where a 2 vol.% addition of nano-Ag improved the relative permittivity of the nanocomposite from 8.1 to 12.2 without affecting the dielectric loss (tan δ = 0.0047 for no Ag, and tan δ = 0.0042 at 2 vol.% Ag).[76]

2.4.2.2 Magnetic Composites

The magnetic behaviour of materials is frequency dependent: although at low frequencies (<1 MHz), magnetic properties do not vary with frequency, in a higher frequency range 1MHz - 100 MHz, the real part of permeability μ' decreases while the imaginary part μ'' increases rapidly. Ferromagnetic resonance usually takes place between 100 MHz and 10 GHz.[81]

For magnetic applications, metals and alloys such as Fe[91,92] and CoPt,[93] oxides such as ferric oxide,[94,67] and ferrite[68] have often been employed as fillers. For $Ba_3Co_2Fe_{23}O_{41}$ (Co_2Z ferrite)-polyvinylidene fluoride (PVDF) composites with filler loading of 60 vol.%, a relative permeability of 3.5 with a magnetic loss factor of 0.2 were achieved at 500 MHz.[74] A composite consisting of iron nanoparticles (20 nm in size) embedded in poly(methylmethacrylate) (PMMA) was demonstrated to have excellent potential for electromagnetic device applications such as electromagnetic interference suppression, and were synthesized using melt blending technique. Magnetic properties, the remnant magnetization M_r and the saturation magnetization M_s, showed a systematic change with iron fraction.[63]

The size effect of nanoparticles on the electromagnetic properties of a polymeric composite was also studied at radio frequencies. Surfactant-modified Fe_3O_4 nanoparticles of various sizes were firstly synthesized by seed-mediated growth method.[64] A copolymer of SEBS was then utilized as a matrix and the dielectric permittivity ε' of the composite increased modestly from 2.4 to 3.0 with increasing fraction of Fe_3O_4 doping from 0 to 16 wt%, and was not affected by nanoparticle size. However, the magnetic permeability μ_r of the composites did not increase systematically with Fe_3O_4 fraction, and was significantly influenced by the nanoparticle size. Larger nanoparticles have higher anisotropy energies, which are needed to overcome the thermal energy fluctuations raised from the nanoparticle surroundings to sustain a high magnetization, and hence provide higher magnetic permeabilities.[64]

The magnetic permeability of composites is affected greatly by the shape distribution of the filler particles.[95] Many papers have reported on composites filled with flake-shaped fillers, such as carbonyl iron,[96] FeSiAl,[97] FeNi,[98] and where, for example, with volume concentration of Fe flake inclusions of approximately 65%, the static permeability can be as high as 15-25 but is associated with a high dielectric loss (up to $\delta_\varepsilon \approx 0.5$).[96] Composites with tiny magnetic fibres and rods,[99,100] and hollow magnetic inclusions[101,102] made by plating thin magnetic films onto hollow glass microspheres have also attracted recent interest.

Negative permeability is required for designing LHMs, and as previously described, structured Cu spilt-ring resonators have been widely used to obtain negative μ in the microwave region.[5] However, Chui and Hu[47] firstly proposed an alternative approach by using the intrinsic magnetic resonance of magnetic metals such as Fe, Co, and Ni. In bulk metal, the effect of the negative real part of permeability μ' cannot be observed due to the high eddy current loss. Therefore, insulating the magnetic metal nanoparticles in a non-magnetic polymer matrix is theoretically feasible in order to realize LHMs in the microwave region. The magnetic permeability of nanocomposite films containing 8 nm diameter Ni particles with various volume fractions was theoretically simulated, where μ' strongly depended on the volume fraction and the distribution (randomness) of the nanoparticles. As the randomness of the particle increased, the region of the negative permeability became broader and with decreased negative permeability values, which is advantageous for broadband LHMs.[103] A recent

study on a 3D all-dielectric composite consisting of an array of $Ba_{0.5}Sr_{0.5}TiO_3$ (BST) cubes in a Teflon substrate was experimentally and numerically demonstrated to have isotropic negative permeability from 8.53 to 8.85 GHz by Zhao *et al*.[104] Distinct from the mechanism in metallic resonators, the negative permeability of the non-metallic structure was attributed to strong sub-wavelength magnetic resonance by the enhancement of the displacement current inside each dielectric cube, where the resonance depends on the size and permittivity of the cubes.[104]

2.4.3 Periodic Composite Structures

The properties of periodic composite structures have been explored for microwave applications.[105] Structures with different dielectric layers were constructed from a BST - cyclo–olefin copolymer (COC) composite material manufactured by a hot lamination approach.[106] The "horizontal" structure in which the layers were parallel to an applied electric field exhibited enhanced high frequency dielectric properties, meanwhile, the introduced structure with combined ductile and brittle layers also offered improved mechanical properties.

The optical properties of multi-layered metal-dielectric metamaterials has also been studied. In this case, the typical layer thickness is at the nanometer size, which is much smaller than the free space wavelength, so that surface plasmon polarions propagating on different metal-dielectric interfaces are strongly coupled to each other.[107] An epsilon near zero (ENZ) metamaterial that operated at visible wavelengths near 660 nm was experimentally demonstrated with a multilayer stack composite of alternating

layers of 16 nm thick Ag and 54 thick nm TiO_2,[108] where Ag was chosen for its low dielectric loss and TiO_2 was chosen for the positive component as it is non-absorbing through the visible region.[108]

2.5 Summary

Metamaterials are a new class of artificial materials with designed sub-structures that exhibit unusual electromagnetic responses. The resulting effective permittivity and permeability are two key macroscopic electromagnetic parameters used to describe the performance of metamaterials. Various structures have been designed, among which resonance was considered to be the main mechanism to realize negative or desired values of permittivity and permeability. Metamaterials based on nm-resonant nanocomposites with spatially varying properties offer weaker interactions with EM waves but are considered to be competitive for practical applications because they are light-weight, deformable and can be fabricated in large-scale. Key challenges in these "all-dielectric" approaches include accurate control of active filler volume fraction, control of permittivity and permeability separately and possibly in different directions, and interface engineering between fillers and the matrix to provide an acceptable dispersion, rheological properties (e.g. low viscosity) to facilitate processing, and high volume fractions to maximise permittivity and permeability.

Bibliography

[1] D. R. Smith, J. B. Pendry, and M. C. K. Wiltshire, Science **305**, 788 (2004).

[2] S. E. Mendhe and Y. P. Kosta, Int. J. Inform. Tech. Know. Manag. **4**, 85 (2011).

[3] N. Engheta and R. W. Zuilkowski, *Metamaterials: Physics and Engineering Explorations*. (John Wiley & Sons & IEEE Press, 2006).

[4] V. G. Veselago, Usp. Fiz. Nauk. **92**, 517 (1967).

[5] D. R. Smith, Willie J. Padilla, D. C. Vier, S. C. Nemat-Nasser, and S. Schultz, Phys. Rev. Lett. **84**, 4184 (2000).

[6] R. A. Shelby, D. R. Smith, and S. Schultz, Science **292**, 77 (2001).

[7] A. F. de Baas, *Nanostructured metamaterials*. (Research *eu, European Commission, 2010).

[8] J. B. Pendry, Phys. Rev. Lett. **85**, 3966 (2000).

[9] J. B. Pendry and D. R. Smith, Sci. Am. **295**, 60 (2006).

[10] A. V. Kabashin, P. Evans, S. Pastkovsky, W. Hendren, G. A. Wurtz, R. Atkinson, R. Pollard, V. A. Podoskiy, and A. V. Zayats, Nat. Mater. **8**, 867 (2009).

[11] Z. Jakšić, S. Vuković, J. Matovic, and D. Tanasković, Materials **4**, 1 (2011).

[12] D. Schurig, J. B. Pendry, and D. R. Smith, Opt. Express **14**, 9794 (2006).

[13] D. Schurig, J. J. Mock, B. J. Justice, S. A. Cummer, J. B. Pendry, A. F. Starr, and D. R. Smith, Science **314**, 977 (2006).

[14] W. Tang, C. Argyropoulos, E. Kallos, W. Song, and Y. Hao, IEEE Trans. Antennas Propag. **58**, 3795 (2010).

[15] D Bao, K. Z. Rajab, Y. Hao, E. Kallos, W. Tang, C. Argyropoulos, Y. Piao, and S. Yang, New. J. Phys. **13**, 103023 (2011).

[16] T. Ergin, N. Stenger, P. Brenner, J. B. Pendry, and M. Wegener, Science **328**, 337 (2010).

[17] N. Landy and D. R. Smith, Nat. Mater. **12**, 25 (2013).

[18] J. B. Pendry, D. Schurig, and D. R. Smith, Science **312**, 1780 (2006).

[19] E. Kallos, C. Argyropoulos, and Y. Hao, Phys. Rev. A **79**, 063825 (2009).

[20] H. Föll, *Electronic Materials,* University of Kiel (2007).

[21] A. Moliton, *Basic Electromagnetism and Materials*, 1st ed., Springer, New York (2007).

[22] B. M. Moskowitz, *Hitchhiker's Guide to Magnetism,* Environmental Magnetism Workshop, Institute for Rock Magnetism, University of Minnesota (1991).

[23] J. B. Tatum, *Electricity and Magnetism*, University of Victoria (2012).

[24] W. J. Padilla, D. N. Basov, and D. R. Smith, Mater. Today **7**, 9 (2006).

[25] A. Ali and Z. Hu, IET Microw. Antenna P **2**, 15 (2008).

[26] H. S. Chen, L. X. Ran, J. T. Huangfu, X. M. Zhang, K. S. Chen, T. M. Grzegorzyk, and J. A. Kong, J. Appl. Phys. **96**, 5338 (2004).

[27] Y. Yao and X. P. Zhao, J. Appl. Phys. **101**, 124904 (2007).

[28] A. Alù, F. Bilotti, N. Eegheta, and L. Vegni, IEEE Trans. Antennas. Propag. **54**, 1632 (2006).

[29] C. Rockstuhl and F. Lederer, Phys. Rev. B **76**, 125426 (2007).

[30] Q. Wu and W. Park, Appl. Phys. Lett. **92**, 153114 (2008).

[31] J. B. Pendry, A. Holden, D. Robbins, and W. J. Stewart, IEEE Trans. Microwave Theory Tech. **47**, 2075 (1999).

[32] J. B. Pendry, A. Holden, D. Robbins, W. J. Stewart, and I. Youngs, Phys. Rev. Lett. **76**, 4773 (1996).

[33] R. Wangberg, J. Elser, E. E. Narimanov, and V. A. Podolskiy, J. Opt. Soc. Am. B **23**, 498 (2006).

[34] M. G. Silveirinha, P. A. Belov, and C. R. Simovski, Phys. Rev. B **75**, 035108 (2007).

[35] L. Menon, W. T. Lu, A. L. Friedman, S. P. Bennett, D. Heiman, and S. Sridhar, Appl. Phys. Lett. **93**, 123117 (2008).

[36] J. Yao, Z. Liu, Y. Liu, Y. Wang, C. Sun, G. Bartal, A. M. Stacy, and X. Zhang, Science **321**, 930 (2008).

[37] S. Zhang, W. Fan, K. J. Malloy, S. R. J. Brueck, N. -C. Panoiu, and R. M. Osgood, Opt. Exp. **13**, 4922 (2005).

[38] A. V. Kildishev, W. Cai, U. K. Chettiar, H. -K. Yuan, A. K. Sarychev, V. P. Drachev, and V. M. Shalaev, J. Opt. Soc. Am. **B23**, 423 (2006).

[39] S. Zhang, . W. Fan, N. C. Panoiu, K. J. Malloy, R. M. Osgood, and S. R. J. Brueck, Opt. Express **14**, 6778 (2006).

[40] J. Valentine, S. Zhang, T. Zentgraf, E. Ulin-Avila, D. A. Genov, G. Bartal, and X. Zhang, Nature **355**, 376 (2008).

[41] C. Helgert, C. Menzel, C. Rockstuhl, E. Pshenay-Severin, E. -B. Kley, A. Chipouline, A. Tünnermann, F. Lederer, and T. Pertsch, Opt. Lett. **34**, 704 (2009).

[42] C. L. Holloway, E. F. Kuester, J. Baker-Jarvis, and P. Kabos, IEEE Trans. Antennas Propag. **51**, 2596 (2003).

[43] A. Pimenov, A. Loidl, P. Przyslupski, and B. Dabrowski, Phys. Rev. Lett. **95**, 247009 (2005).

[44] X. L. Chen, M. He, Y. X. Du, W. Y. Wang, and D. F. Zhang, Phys. Rev. **B72**, 113111 (2005).

[45] A. L. Adenot-Englvin, C. Dudek, P. Toneguzzo, and O. Acher, J. Eur. Ceram. Soc. **27**, 1029 (2007).

[46] Y. X. He, P. He, S. D. Yoon, F. J. Rachford, Y. G. Harris, and C. Vittoria, J. Magn. Magn. Mater. **313**, 187 (2007).

[47] S. T. Chui and L. Hu, Phys. Rev. **B65**, 144407 (2002).

[48] C. Lederer Rockstuhl, F. Etrich, C. Pertsch, T. Scharf, T., Phys. Rev. Lett. **99**, 017401 (2007).

[49] C. Rockstuhl and T. Scharf, Microscopy **229**, 281 (2008).

[50] M. S. Aitchison Wheeler, J. S. Mojahedi, M., Phys. Rev. B **73**, 045105 (2006).

[51] N. Liu, H. Guo, L. Fu, S. Kaiser, H. Schweizer, and H. Giessen, Nat. Mater. **7**, 31 (2008).

[52] A. Di Falco, M. Ploschner, and T. F. Krauss, New J. Phys. **12**, 113006 (2010).

[53] I. Bergmair, B. Dastmalchi, M. Bergmair, A. Saee, W. Hilber, G. Hesser, C. Helgert, E. Pshenay-Severin, T. Pertsch, E. B. Kley, U. Hübner, N. H. Shen, R. Penciu, M. Kafesaki, C. M. Soukoulis, K. Hingerl, M. Muehlberger, and R. Schoeftner, Nanotechnology **22**, 325301 (2011).

[54] C. Ciracì, X. Chen, J. J. Mock, F. McGuire, X. Liu, S. H. Oh, and Smith D. R., Appl. Phys. Lett. **104**, 023109 (2014).

[55] H. Liu, X. Zhao, Y. Yang, Q. Li, and J. Lv, Adv. Mater. **20**, 2050 (2008).

[56] M. K. Hedayati, M. Javaherirahim, B. Mozooni, R. Abdelaziz, A. Tavassolizadeh, V. S. K. Chakravadhanula, V. Zaporojtchenko, T. Strunkus, F. Faupel, and M. Elbahri, Adv. Mater. **23**, 5410 (2011).

[57] C. B. Murray, C. R. Kagan, and M. G. Bawendi, Annu. Rev. Mater. Sci. **30**, 545 (2000).

[58] M. Nagel, S. G. Hickey, A. Frömsdorf, A. Kornowski, and H. Weller, J. Phys. Chem. **221**, 427 (2007).

[59] H. Yoshimura, Coll. Surf. A **282-3**, 464 (2006).

[60] S. Salvatore, A. Demetriadou, S. Vignolini, S. S. Oh, S. Wuestner, N. A. Yufa, M. Stefik, U. Wiesner, J. J. Baumberg, O. Hess, and Steiner. U., Adv. Mater. **25**, 2713 (2013).

[61] S. Prayakarao, S. Robbins, N. Kinsey, A. Boltasseva, V. M. Shalaev, U. B. Wiesner, C. E. Bonner, R. Hussain, N. Noginova, and M. A. Noginov, Opt. Mater. Express **5**, 1316 (2015).

[62] K. M. Lim, K. A. Lee, M. C. Kim, and C. G. Park, J. Non-Cryst. Solids **75**, 351 (2005).

[63] J. L. Wilson, P. Poddar, N. A. Frey, H. Srikanth, and K. Mohomed, J. Appl. Phys. **95**, 1439 (2004).

[64] T. I. Yang, R. N. C. Brown, L. C. Kempel , and P. Kofinas, **329**, 2714 (2008).

[65] K. Lichtenecker and Rother K., Phys. Z. **32**, 255 (1931).

[66] T. Hu, J. Juuti, H. Jantunen, and T. Vilkman, J. Eur. Soc. **27**, 3997 (2007).

[67] Z. M. Dang, H. Y. Wang, and H. P. Xu, Appl. Phys. Lett. **89**, 112902 (2006).

[68] M. Kobune, K. Takasaki, and T. Yazawa, Jpn. J. Appl. Phys. **45**, 7371 (2006).

[69] J. C. Maxwell Garnett, Phil. Trans. R. Soc. Lond. A **203**, 385 (1904).

[70] D. A. G. Bruggeman, *Annalen der Physik* **416**, 636 (1935).

[71] Y. Rao, J. Qu, T. Marinis, and C. P. Wong, IEEE Trans. Compon. Packag. Technol. **23**, 680 (2000).

[72] L. Jylhä and A. Sihvola, J. Phys. D: Appl. Phys. **40**, 4966 (2007).

[73] R. Simpkin, IEEE Trans. Microwave Theory Techn. **58**, 3 (2010).

[74] B. W. Li, Y. Shen, Z. X. Yue, and C. W. Nan, J. Appl. Phys. **99**, 123909 (2006).

[75] Y. Shen, Z Yue, M. Li, and C. W. Nan, Adv. Funct. Mater. **15**, 1100 (2005).

[76] M. Teirikangas, Acta Univ. Oul. C **398** (2011).

[77] H. D. Choi, K. Y. Cho, S. Han, H. G. Yoon, and T. J. Moon, J. Appl. Polym. Sci. **67**, 363 (1998).

[78] S. H. Li, M. M. Lin, M. S. Toprak, D. K. Kim, and M. Muhammed, Nano Rev. **1**, 5214 (2012).

[79] C. Lü, Y. Cheng, Y. Liu, F. Liu, and B. Yang, Adv. Mater. **18**, 1188 (2006).

[80] L. Zimmermann, M. Weibel, W. Caseri, U. W. Suter, and P. Walter, Polym. Adv. Technol. **4**, 17 (1993).

[81] L. F. Chen, C. K. Ong, C. P. Neo, V. V. Varadan, and V. K. Varadan, *Microwave electronics: Measurement and materials characterization*. (Wiley, 2004).

[82] R. Popielarz, C. K. Chiang, R. Nozaki, and J. Obrzut, Macromolecules **34**, 5910 (2001).

[83] F. Xiang, H. Wang, and X. Yao, J. Eur. Soc. **26**, 1999 (2006).

[84] T. Hu, J. Juuti, and H. Jantunen, J. Eur. Soc. **27**, 2923 (2007).

[85] S. Koulouridis, G. Kiziltas, Y. Zhou, D. J. Hansford, and J. L. Volakis, IEEE Trans. Microwave Theory Tech. **54**, 4202 (2006).

[86] B Li, G. Sui, and W. H. Zhong, Adv. Mater. **21**, 4176 (2009).

[87] Z. M. Dang, Y. H. Zhang, and S. C. Tjong, Synth. Met. **146**, 79 (2004).

[88] G. S. Wang, Y. Deng, Y. Xiang, and L. Guo, Adv. Funct. Mater. **18**, 2584 (2008).

[89] R. Vaia and H. Wagner, Mater. Today **7**, 32 (2004).

[90] S. George, N. I. Santha, and M. T. Sebastian, J. Phys. Chem. Solids **70**, 107 (2009).

[91] L. Li, X. M. Chen, and X. C. Fan, J. Eur. Ceram. Soc. **26**, 3265 (2006).

[92] M. Valant, A. Dakskobler, M. Ambrozoc, and T. Kosmac, J. Eur. Ceram. Soc. **26**, 891 (2006).

[93] X. Liu, F. Gao, J. Liu, and C. Tian, J. Alloy Compd. **470**, 269 (2009).

[94] J. A. Otero, R. Rodrigues-Ramos, G. Monsivais, and R. Perez-Alvarez, **37**, 33 (2005).

[95] K. N. Rozanov, A. V. Osipov, D. A. Petrov, S. N. Starostenkoa, and E. P. Yelsukov, J. Magn. Magn. Mater. **321**, 738 (2009).

[96] S. S. Kim, S. T. Kim, Y. C. Yoon, and K. S. Lee, J. Appl. Phys. **97**, 10F905 (2005).

[97] S. Yoshida, S. Ando, Y. Shimada, K. Suzuki, K. Nomura, and K. Fukamichi, J. Appl. Phys. **93**, 6659 (2003).

[98] P. H. Zhou, L. J. Deng, J. L. Xie, D. F. Liang, L. Chen, and X. Q. Zhao, J. Magn. Magn. Mater. **292**, 325 (2005).

[99] J. R. Liu, M. Itoh, M. Terada, T. Horikawa, and K. I. Machida, Appl. Phys. Lett. **91**, 093101 (2007).

[100] M. Wu, Z. Zhao, H. He, and X. Yao, J. Magn. Magn. Mater. **217**, 89 (2000).

[101] S. S. Kim, S. T. Kim, J. M. Ahn, and K. H. Kim, J. Magn. Magn. Mater. **271** (1), 39 (2004).

[102] J. Wei, J. Liu, and S. Li, J. Magn. Magn. Mater. **312**, 414 (2007).

[103] C. Mitsumata and S. Tomita, Appl. Phys. Lett. **91**, 223104 (2007).

[104] Q. Kang Zhao, L. Du, B. Zhao, H. Xie, Q. Huang, X. Li, B. Zhou, J. Li, L., Phys. Rev. Lett. **101**, 027402 (2008).

[105] O. V. Sherman, A. K. Tagantsev, and N. Setter, J. Appl. Phys. **99**, 074104 (2006).

[106] M. Teirikangas, J. Juuti, and H. Jantunen, Ferroelectrics **387**, 210 (2009).

[107] J. Elser, V. A. Podolskiy, I. Salakhutdinov, and I. Avrutsky, Appl. Phys. Lett. **90**, 191109 (2007).

[108] G. Subramania, A. J. Fischer, and T. S. Luk, Appl. Phys. Lett. **101**, 241107 (2012).

Chapter 3

Experimental

This chapter describes the manufacturing approaches and characterization techniques used for electromagnetic polymer-based composite materials studied in this thesis. The main manufacturing approaches explored for convenient spatially varying arrangement of materials according to spatial transformation based designs are casting, spray deposition and 3D printing (additive manufacture). More detailed information on each specific material and the experimental procedures developed are described in the subsequent chapters, while the information here describes the general experimental approaches relevant to all materials/processes studied.

3.1 Fabrication

3.1.1 Casting

Casting is a straightforward and widespread manufacturing process by which a liquid material is solidified in a suitably-shaped mould to form an object. Because of its convenience, low-cost and capability of making complex shapes, casting has been

introduced to fabricate polymer-based bulk composite materials, as shown in Fig. 3.1. The electromagnetic properties of the composites are achieved by loading the polymer with high permittivity and permeability particles. In the experiments, micro-size fillers are typically blended into epoxide monomers assisted with magnetic stirring and ultrasonication to ensure adequate homogeneity of filler dispersion in the polymer matrix. The composite paste was consequently poured into a silicone mould and cured for solidification at an elevated temperature (~ 60 °C) overnight. The cast composites can then be machined for designed applications.

FIG. 3.1. Photographs of the silicone mould, casted epoxy and epoxy-NiZn ferrite composite samples. The samples were subsequently machined into two identical pieces for permittivity and permeability measurements.

Ball milling, which is a method to grind material through the high-energy impact of grinding balls in rotating jar, was used in some cases to pre-grind the inorganic filler particles for particle size reduction or shape changes. In this case, a planetary ball mill was used with at least one grinding jar that was arranged eccentrically on a so-called sun wheel that rotated in an opposite direction to that of the grinding jar, as shown in Fig. 3.2. The difference in speeds between the balls and jar generated high kinetic energies of the balls used to grind the materials. The ball milling treatment was performed at room temperature under air atmosphere using a high-energy planetary mill (Pulvrtisette 6, Fritsch GmbH, Germany). The feedstock, normally ferrite

powders, were loaded in a ceramic jar together with ZrO_2 10 mm diameter milling balls at a ball-to-powder weight ratio of 10:1. The milling rotation speed and milling time were investigated. During the milling process, the planetary mill was set to mill and rest alternatively for every 30 min to avoid overheating. More details are given later.

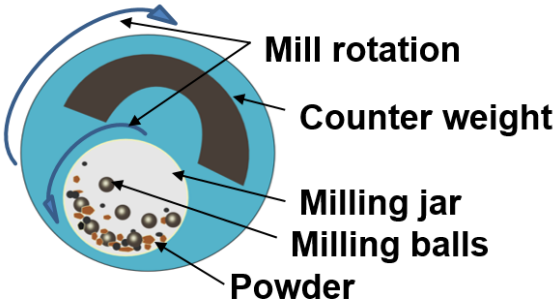

FIG. 3.2. Schematic of planetary ball milling motion.

3.1.2 Spray Deposition

Spray deposition provides a flexible and scalable manufacturing approach for the fabrication of composite films, with the potential to form patterned patches of dielectric or magnetic composites over a curved surface. An out-of-vacuum spray deposition facility designed and built by the group,[1] has progressively been developed into two variants, as shown in Figs. 3.3 and 3.4. During the process, a pre-prepared stable suspensions of polymer and filler particles were syringe or peristaltic pumped at a controlled rate into a compressed air atomizer to form a myriad of fine (< 50 μm) droplets that were sprayed onto a heated substrate, where the suspension liquid carrier evaporates almost immediately. In this study, thermopolymers were used and the as-

sprayed films were then cured in a belt furnace (Dek Model840), where the molten polymer engulfed and incorporated the fillers particles into a robust composite film of 10-100 μm thickness. The spray parameters such as compressed air pressure (140 - 400 kPa), suspension flow rate (2-8 ml/min), spray distance (9-18 cm above substrate), traverse nozzle speed (100-350 mm/s), and substrate temperature (90-110^{o} C for aqueous based, and 70-90^{o}C for ethanol based) were investigated for different material systems to ensure successful deposition. The key to successful manufacture was developing stable suspensions of the various materials suitable for spraying. In general, the suspensions were prepared by dispersing nanoparticles with high power ultrasonication (600 W, 20 kHz) in a liquid carrier, where water was generally preferred, but organic liquids such as ethanol were also necessarily used. Surfactants were also used to prevent particle agglomeration and to improve suspension stability. More details are given later.

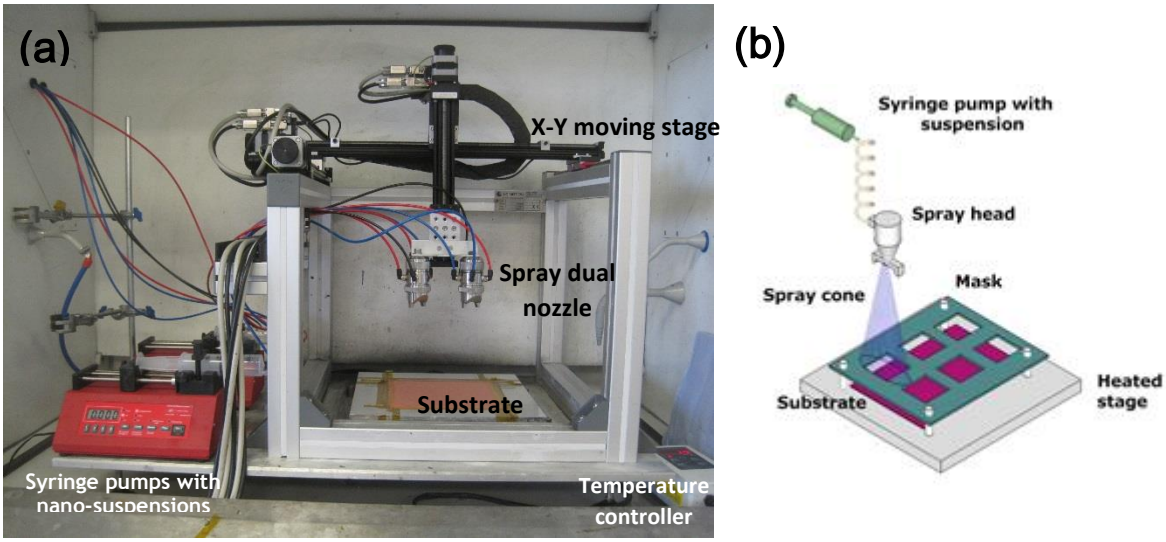

FIG. 3.3. (a) Photograph and (b) schematic of the spray apparatus for flat, large area spray deposition of composite films. The spray nozzles move in the *x-y* plane according to a pre-programmed path.

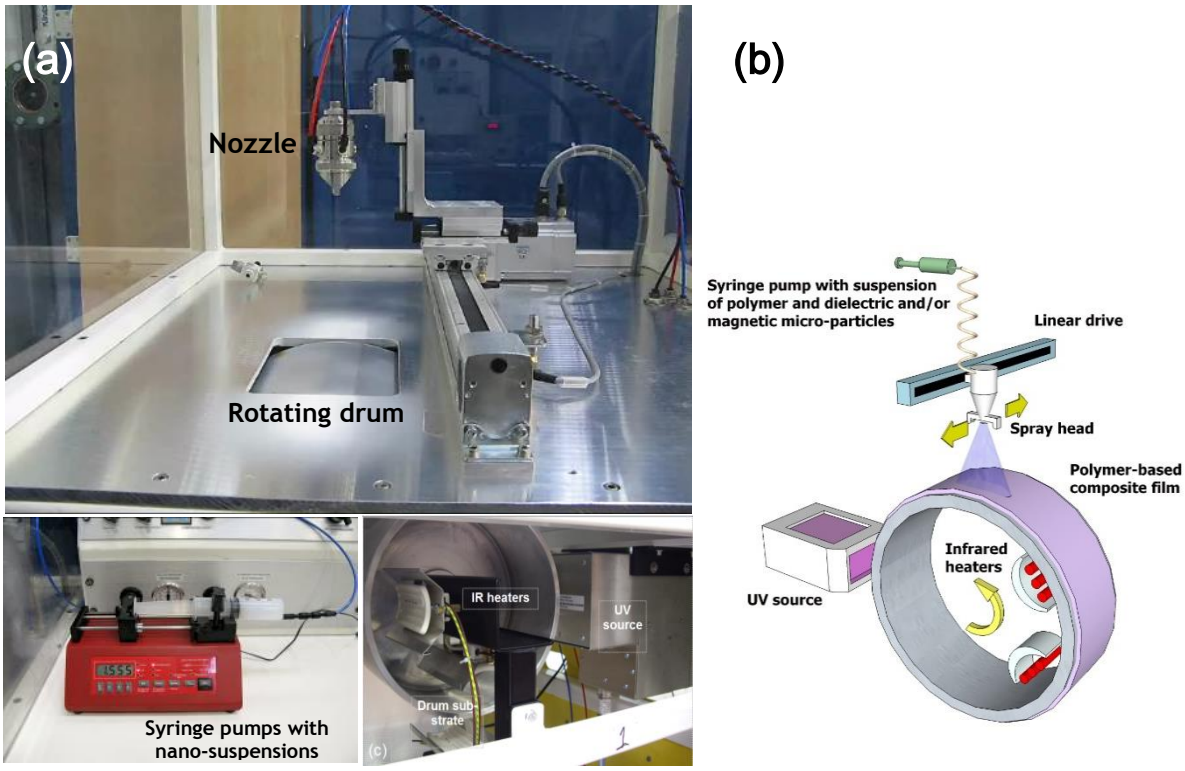

FIG. 3.4. (a) Photograph and (b) schematic of the spray apparatus for flexible large area deposition. The substrate involves a rotating drum with a controlled, internal IR heater arrangement, as well as a UV source that enables *in-situ* curing of monomers during manufacture to produce large area nanocomposite films.

3.1.3 3D Printing

Some metamaterial applications require spatial variations of permittivity and permeability, which can be difficult to achieve by conventional manufacturing technologies especially in 3D. Additive manufacture, or 3D printing, may provide an advantage because it is capable of placing different materials in three dimensions

directly from a computer aided design, and has been recently demonstrated for the fabrication of electromagnetic devices that operate at microwave frequencies.[3-6] Fused deposition modelling (FDM) – a form of 3D printing- is an additive manufacturing process that uses a polymer-based filament feedstock. In this study, a commercially available FDM machine – Makerbot Replicator – was used, and the setup is shown in Fig. 3.5. The thermoplastic filament was fed into the printer head through a motorised drive system at a controlled rate, where it was melted and then extruded continuously through the moving head to deposit a layer onto the top surface of a build platform. Objects were created by depositing the polymer (and polymer composite) layer by layer according to a pre-programmed designed pattern, with the build platform lowering by a pre-set amount (typically 100 μm) after each layer, corresponding to the thickness of the extruded polymer layer.

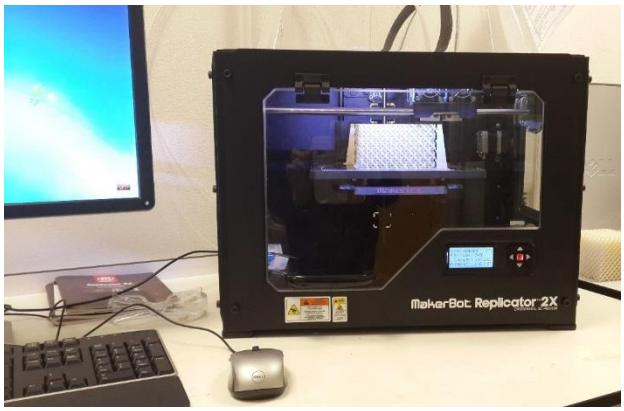

FIG. 3.5. Photograph of the 3D printing, or additive manufacture, setup with 100 μm layer resolution and up to 28.4 × 15.5 × 15.2 cm build volume.

However, the conventionally used polymer feedstocks, such as acrylonitrile butadiene styrene (ABS) have a relative permittivity of approximate 3 and a relative permeability of 1, limiting design to all-dielectric devices of low "dielectric contrast" (variation

between maximum and minimum permittivities achievable in a single printed structure). The key challenge therefore to employ this technique usefully for electromagnetic devices is to develop and fabricate printable composite filament with well-controlled dielectric and magnetic properties. The magnetic composite filaments used in this thesis were fabricated by dispersing ferrite particles into a dissolved ABS polymer solution, then evaporating the solvent and extruding the "dried" solid composite into feedstock filaments of the correct diameter. The printing parameters, e.g. nozzle temperature, nozzle head size, feed rate, and printing speed, needed to be re-optimized for printing different composite material systems. More details are given later.

3.2 Characterisation

A wide variety of techniques have been employed for materials and electromagnetic properties characterization. Those widely used throughout the thesis are described here; more specific analyses and characterization details are given later in the appropriate chapter.

3.2.1 X-Ray Diffraction (XRD)

The X-ray diffraction (XRD) patterns of filler particles (NiZn ferrite, Fe_3O_4, etc.) were characterized using a Siemens D5000 X-ray diffractometer with Cu Kα radiation (λ = 1.5406 Å), which were used to identify materials crystalline structures and compound

stoichiometry by comparing the diffraction traces to standard databases compiled by the International Centre for Diffraction Data (ICDD).

3.2.2 Laser Diffraction Analysis

Particle size distributions were measured by laser diffraction using a Mastersizer 2000 Analyser (Malvern Instruments Ltd.) for materials in the diameter range 0.02 μm to 2000 μm. Measurements were carried out by passing a laser beam through a dilute aqueous suspension of particles that scattered the light, as demonstrated in Fig. 3.6. The light scattering angle relative to the laser beam is inversely proportional to the particle size, based on which the particle size distribution can be calculated from the angular scattering intensity data from a stream of particles recirculated through the measurement cell. The measured particle size distribution were generated based on a volume equivalent sphere diameter for each data point.

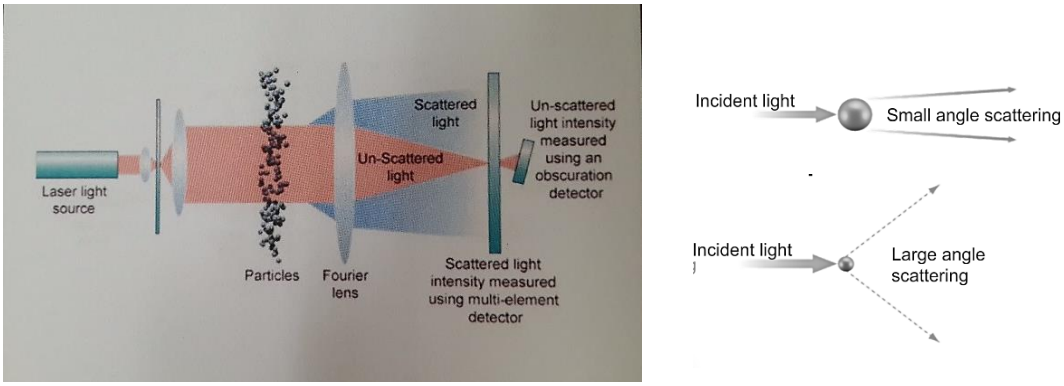

FIG. 3.6. Schematics of the working principle of the laser diffraction technique for particle size measurement. Light is scattered at a small angle for large particles and at a large angle for small particles. Taken from [7].

3.2.3 Surface Profilometer

The thickness of sprayed composite films was measured by a Dektak 6M stylus surface profilometer (Bruker UK Ltd.). The measurement was carried out by riding a diamond-tipped stylus over the sample surface according to a user-programmed scan length, speed and stylus force. The stylus movement in the vertical direction (ranging from 5 nm to 130 μm) caused by the sample surface variations were recorded along the scan length. The film thickness was measurement by a vertical "step height" between a smooth substrate and the film top surface. Glass was normally used as the smooth substrate to level and zero the profile. For each film sample, measurements were taken from 5 different positions to obtain an average thickness.

3.2.4 Confocal Microscopy

The surface morphologies and roughness of sprayed polymer films before and after curing were characterised by an optical confocal profilometer NanoFocus μSurf (NanoFocus AG Ltd.). As shown in Fig. 3.7, the confocal microscope consisted of a light source, a rotating multi-pinhole disc, a piezo-driven confocal measuring head with objective lens, and a CCD camera detector. Images are formed only when light beams are focused on the detector. All other unfocused beams, i.e. which are not at the same height, are filtered out by the operation of the multi-pinhole disc, enabling high *z*-resolution of the confocal microscope in the nanometer range. The sample is positioned on an *x*-*y* stage, and the objective lens moved precisely in the vertical

direction (z-axis) by means of a piezo drive to capture images at various focal heights, which can then be reconstructed into a 2D or 3D topographical maps. The average surface roughness S_a was calculated from the scanned surface profile.

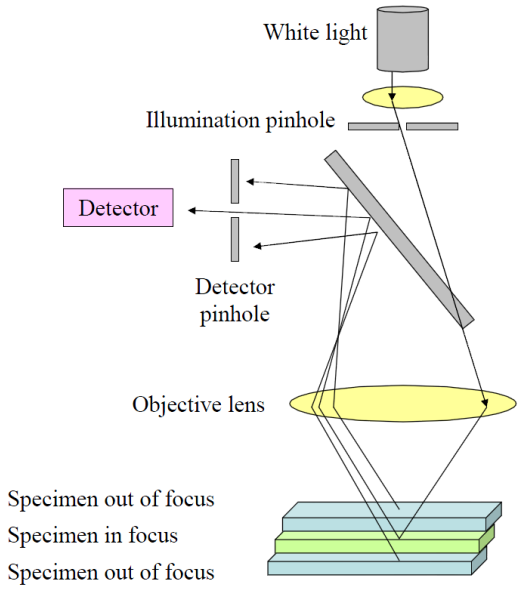

FIG. 3.7. Schematic of working principle of the confocal measurement. Taken from[8].

3.2.5 Scanning Electron Microscopy (SEM)

The morphologies of various filler particles and the microstructures of composite cross-sections were characterised by a field emission scanning electron microscope (FESEM, JEOL 840 F). Images were taken at 5 kV. Non-conductive material samples, e.g. ceramic particles and polymer based composites, were sputter coated with a thin layer of platinum (~ 2 nm) in a sputter coater (Cressington 208HR) to avoid electron charging. For bulk samples, silver conducting paste was applied between the sample

and the mounting stub to further reduce charging. Microtome cutting (Reichert-Jung Ultracut E) was used to prepare cross-section samples of composite materials.

3.2.6 Transmission Electron Microscopy (TEM)

The morphology and crystalline structure of ferrofluid nanoparticles were characterised by a transmission electron microscopy (TEM, JEOL 2000FX) operating at a voltage of 200kV. The ferrofluid nanoparticle samples for TEM were prepared by diluting the ferrofluid suspensions in water, pipetting and drying on a carbon film-coated copper grid (400 mesh, Agar Scientific Ltd., UK).

3.2.7 Impedance Analyser

The dielectric complex permeability of polymer nanocomposite films at low frequencies in the range 100 Hz to 1 MHz were measured using a Solartron SI 1260 impedance analyser at room temperature. The impedance analyser was interfaced and controlled by a PC running Solartron Analytical SMaRT software. The film samples were prepared by evaporating gold layers (70 nm thick) on both bottom and top sides of the sprayed film using an Edwards auto 306 vacuum evaporator to form simple parallel-plate capacitors, and measurements obtained with the samples placed in a Faraday cage. For the measurement, an AC voltage of 1 V was applied across the film, 25 measured data points per decade were recorded on a logarithmic scale, and each measurement was integrated over 100 cycles to reduce noise.

3.2.8 Vibrating Sample Magnetometer (VSM)

The magnetic magnetization of polymer-composite films was measured using a Lakeshore 7400 series vibrating sample magnetometer (VSM). The working principle of the VSM is based on the flux change in a nearby pickup coil when a sample is vibrated sinusoidally inside a uniform magnetic field near it. The oscillating magnetic field of the moving sample induces voltage changes in the pickup coil, which are proportional to the sample's magnetic moment. The typical setup is shown in Fig. 3.8: the sample was attached to the end of a non-magnetic rod, the other end of which was driven by mechanical vibrator (e.g. loudspeaker cone). The measurements were taken by applying a uniform magnetic field from 0.5 T to -0.5 T; 250 measured data points at 3 s/point were recorded for one hysteresis curve from each sample.

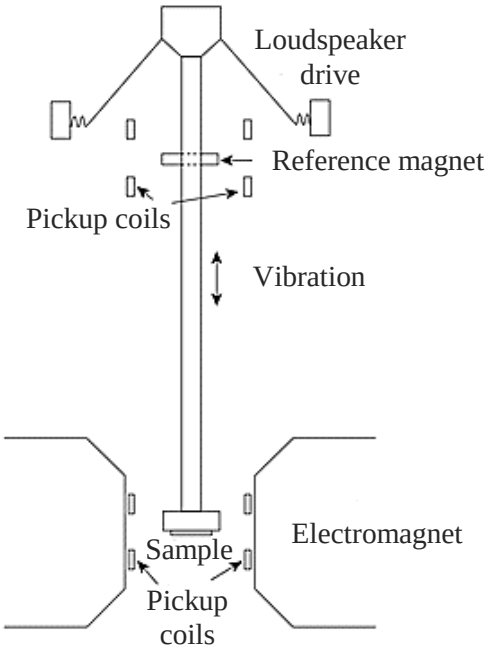

FIG. 3.8. Schematic of the operation of a vibrating sample magnetometer. Taken from[9].

3.2.9 Vector Network Analyser (VNA)

The broadband complex permittivity and permeability of composite materials at high frequencies (1 MHz to 18 GHz) were measured using a vector network analysers (VNA) (Anritsu MS4644A and Rohde & Schwarz ZNB 20) using a transmission/reflection method. A VNA consists of a signal source, a receiver and a display, as shown in Fig. 3.9. In the measurement, the source generates a single frequency signal to the material under test, and the receiver detects the transmitted and reflected signals which are also known as scattering parameters (*S*-parameters) from the material at that frequency. The source is then stepped to the next frequency at which the measurement is repeated to record the *S*-parameters as a function of frequency.

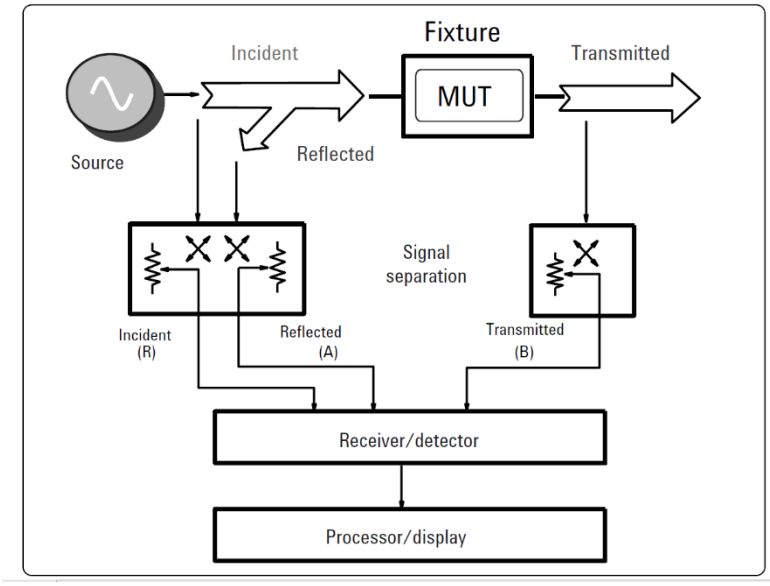

FIG. 3.9. Schematic of vector network analyser arrangement. Taken from [10].

Before measurements, calibration of the VNA is used to eliminate systematic error, which is a crucial step for accurate measurements. VNAs were calibrated using a SOLT method (acronym for Short, Open, Load, Thru). As the name suggests, this involved connecting known standards with a short circuit, open circuit, a precise 50 ohms load to both cables that are connected to two test ports, and then a through connect by connecting the two cables together. In the transmission/reflection method, the sample under test is inserted into a segment of a transmission line jig, such as a co-axial line or a stripline, which is connected to the VNA. The choice of the measurement jig depends on the measurement frequency range and the processibility of material under test. In the stripline measurement (1 MHz – 5 GHz), two identical rectangular samples were needed and were placed symmetrically above and below the conducting line with a dimension fitted tightly within the stripline jig, as shown in Fig. 3.10. In the co-axial line measurement (1 MHz – 18 GHz), a toroidal sample with an outer diameter of 7 mm and an inner diameter of 3 mm was inserted between the inner and outer conductors of the co-axial line jig, as shown in Fig. 3.11. From the frequency-swept *S*-parameter measurement from the sample-loaded stripline or co-axial line fixture, the complex permittivity and permeability can be calculated according to the standard Nicolson-Ross-Weir (NRW) algorithm.[11-13]

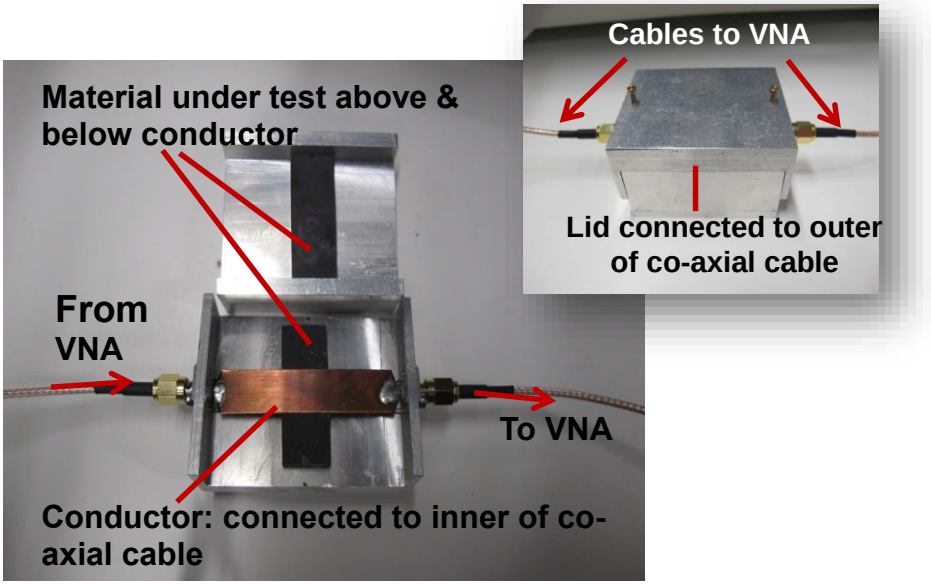

FIG. 3.10. Photographs of the stripline measurement jig with materials under test placed above and below the copper stripline conductor.

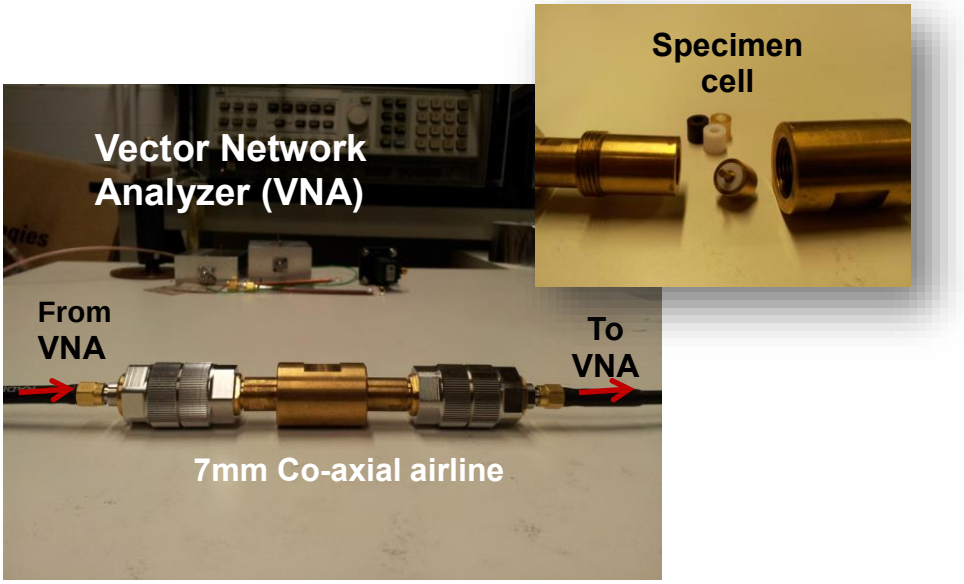

FIG. 3.11. Photographs of the co-axial measurement jig with ring-shaped sample under test inserted in between inner and outer conductor of the co-axial line.

Bibliography

[1] H. Hinchliffe, DPhil Thesis, University of Oxford, Oxford, UK (2006).

[2] X. Zhao, DPhil Thesis, University of Oxford, Oxford, UK (2009).

[3] M. Ahmadloo, IEEE 22nd Conference on Electrical Performance of Electronic Packaging and Systems (EPEPS), 29 (2013).

[4] C. R. Garcia, J. Correa, D. Espalin, J. H. Barton, R. C. Rumpf, R. Wicker, and V. Gonzalez, Prog. Electromagn. Res. **34**, 75 (2012).

[5] M. Liang, W. R. Ng, K. Chang, M. E. Gehm, and H. Xin, Proc. IEEE Int. Microw. Symp., 1 (2011).

[6] I. M. Ehrenberg, S. E. Sarma, and B.-I. Wu, J. Appl. Phys. **112**, 073114 (2012).

[7] K. Powers, Understanding laser diffraction particle size analysis, Malvern Webinar, Malvern Instruments Limited (2014).

[8] NanoFocus μSurf Operating Manual, 1st edition, NanoFocus AG, Oberhausen. (2003).

[9] B. D. Cullity and C. D. Graham, *Introduction to Magnetic Materials*. (Wiley, New Jersey, 2009).

[10] *Basic of Measuring the Dielectric Properties of Materials Application Note*. (Agilent Technologies).

[11] A. M. Nicolson and G. F. Ross, IEEE Trans. Instrum. Meas. **19** (4), 377 (1970).

[12] W. B. Weir, Proc. IEEE **62** (1), 33 (1974).

[13] L. F. Chen, C. K. Ong, C. P. Neo, V. V. Varadan, and V. K. Varadan, *Microwave electronics: Measurement and materials characterization*, Wiley, West Sussex (2004).

Chapter 4

Polymer based Ferrite Composites by Casting

This chapter describes the casting of electromagnetic composites by embedding filler particles in an epoxy matrix. This approach was used to show how impedance matched materials with relatively high and equal permittivity and permeability that are promising for applications in telecommunications could be achieved using NiZn ferrite composites, and how a useful magnetic response of the easy-to-process composite could be maintained to higher frequency with a controlled combination of soft magnetic ferrites and metallic magnetic filler materials.

4.1 Scalable Polymer based Ferrite Composites with Matching Permeability and Permittivity

4.1.1 Introduction

Materials that allow no reflection and complete power transmission of incident radiation at discontinuities or interfaces are in demand for advances in stealth technology, anti-reflection coating, and antenna miniaturization.[1,2] To realize zero reflection, materials used in device construction must have impedance ($Z = Z_0\sqrt{\mu'/\varepsilon'}$, where Z and Z_0 are the impedance of the material and free space respectively, μ' and ε' are the real parts of the relative permeability and permittivity of the materials) match to that of free space, so that μ' and ε' must be equal. However, no naturally occurring monolithic materials have been found so far that satisfy impedance matching conditions.

Whilst it has been suggested that a chessboard structure comprising a periodic array of magnetic and dielectric media could provide equal values of relative real permeability and permittivity,[3,4] these approaches present practical manufacturing and scaling difficulties so that technological implementation has been limited. Alternatively, impedance-matched materials can be achieved through control of the microstructural porosity and grain size of complex nano-ferrites with compositions such as $Ni_{0.35}Zn_{0.35}Co_{0.2}Mn_{0.05}Cu_{0.05}Fe_{1.98}O_4$,[5] $Ni_{0.5}Zn_{0.3}Co_{0.2}Fe_2O_4$,[6,7] and $Ni_{0.855}Cu_{0.1}Zn_{0.025}$-

$Co_{0.02}Fe_{1.98}O_4$[8] via appropriate heat treatment. Similarly, manipulations of the stoichiometry of $Ni_{0.95-x}Zn_xCo_{0.05}Fe_{1.90}Mn_{0.02}O_4$ ferrites can achieve variations in relative permeability and the impedance can be matched with x = 0.10-0.25, but only for frequencies between 2-30 MHz.[9] These studies confirm the possibility of realizing impedance matched materials artificially but rely on the use of sintered ceramics with often complex and difficult to control compositions, prepared by intricate co-precipitation and heat treatments that leads to comparatively high-cost.

As an alternative, polymer composites are considered attractive owing to their light-weight, deformability, and ease of tunable physiochemical properties. It has been demonstrated that through smart manipulation of the composition, size, and morphology of the fillers in composites, improved electromagnetic absorption behaviour can be achieved.[10-12] In this chapter, a simple polymer-based composite approach to achieving matching permeability and permittivity is shown to be attractive because of the potential for large-scale manufacturing, and the ability to fabricate various 3D shapes and thus real components, overcoming the disadvantages of complex composition ferrite ceramics. Ferrite composites of refractive index ~ 6 are developed that are broadband impedance matched to free space, with more than 96% power transmission and less than 0.03% power reflection, up to approximately 100 MHz. Measurements of the frequency-dependent complex permeability and permittivity of these epoxy based composites using a stripline technique[13] for frequencies between 5 MHz to 2 GHz, are discussed, and both impedance-matching for a ferrite loading of 53 vol.%, and the ability to produce practical antenna geometries with ease are demonstrated.

4.1.2 Experimental

The polymer matrix for the composites was commercial epoxy embedding medium (Epon™ 812 substitute) with two different hardeners of 2 dodecenylsuccinic anhydride (DDSA) and methylnadic anhydride (MNA) (Sigma Aldrich Ltd. UK). The ferrite filler was sintered NiZn ferrite powder (F16 MagDev Ltd. UK) with composition $Ni_{0.4}Zn_{0.6}Fe_2O_4$ (standard pattern ref. No. 01-077-9718) by X-ray diffraction (Simens D5000) operated by Dr. Philip Holdway. The range of particle sizes spanned from 1 μm to 10 μm determined by laser diffraction (Mastersizer 2000, Malvern Instruments Ltd.). NiZn ferrite powder and epoxy were mixed together using 5 min ultrasonication in an ice bath and then cured at 60 °C overnight. Prolonged stirring and ultrasonication in an ice bath were necessary to disperse the highest ferrite loadings into an acceptably uniform distribution of particles within the epoxy matrix. Composites with 0, 11, 32, 53 and 61 vol.% NiZn ferrite filler were prepared, with 61 vol.% the highest loading that could be easily cast due to increasing viscosity. For an even higher loading, cold-pressing can achieve up to 80 vol.% ferrite in a polymer matrix, but has greater geometric restrictions.[14]

The magnetic and dielectric properties of the composites were measured using a standard stripline technique in which a central flat conducting line is symmetrically bounded by two ground planes and supports a transverse electromagnetic (TEM) waveguide mode. The stripline rig was connected to a calibrated vector network analyzer (VNA, Anritsu MS4644A) and used to measure the complex reflection and transmission amplitude coefficients of two identical blocks of materials placed

symmetrically above and below the conducting line. The complex permeability and permittivity of the material were then extracted according to the method of Nicolson, Ross and Weir.[15,16] The dimensions of the samples were length = 43 mm, width = 15 mm, and thickness = 4.8 mm. In order to fit tightly within the stripline rig to avoid air gaps all samples were machined with extra care. Standard polytetrafluoroethylene (PTFE) samples with known permittivity and permeability values ($\varepsilon = 2$, $\mu = 1$) were used to validate calibration before experimental measurements. The electromagnetic wave propagated along the direction of sample width during measurements.

4.1.3 Results and Discussion

Fig. 4.1 shows the X-ray diffraction (XRD) pattern of the as-supplied ferrite powder in which all peaks are readily fitted to a cubic spinel structure with composition $Ni_{0.4}Zn_{0.6}Fe_2O_4$ (standard pattern ref. No. 01-077-9718), indicating a negligible fraction of any unreacted constituents or impurities. Fig. 4.2(a) is an SEM image of the NiZn ferrite powders with polyhedral faceted particle shape, likely to be surface planes (111) and (100) that are characteristic of the spinel structure.[17,18] The powder particle size distribution determined by laser diffraction is shown in Fig. 4.2(b) with typical particle dimensions from 1 to 10 μm and a small fraction of particles with diameters as large as a few hundreds of microns.

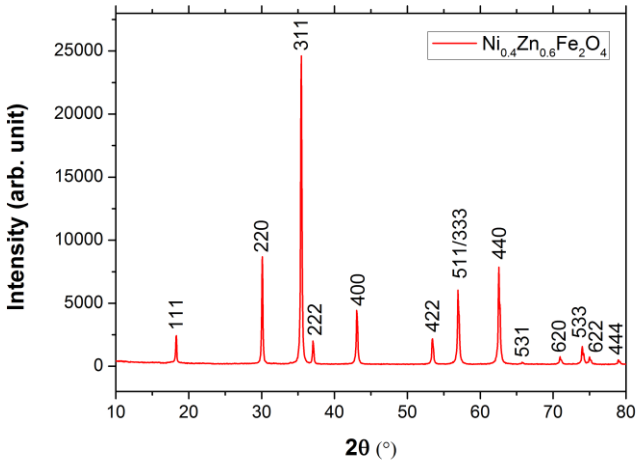

FIG. 4.1. XRD pattern of the as-supplied $Ni_{0.4}Zn_{0.6}Fe_2O_4$ ferrite power

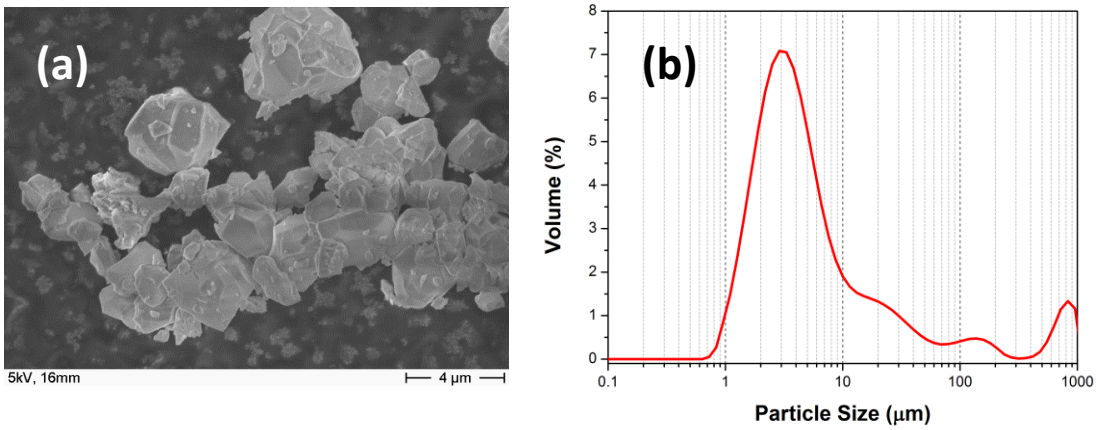

FIG. 4.2. (a) SEM image of the NiZn ferrite powders; and (b) the NiZn ferrite particle size distribution determined by laser diffraction.

An SEM image of a cross-section of a 53 vol. % ferrite casting is shown in Fig. 4.3. Consideration of many such cross-sections indicated an adequate homogeneity of ferrite filler dispersion with no large agglomerates; the cross-sections also suggested that while there were entrapped air bubbles, they were comparatively rare.

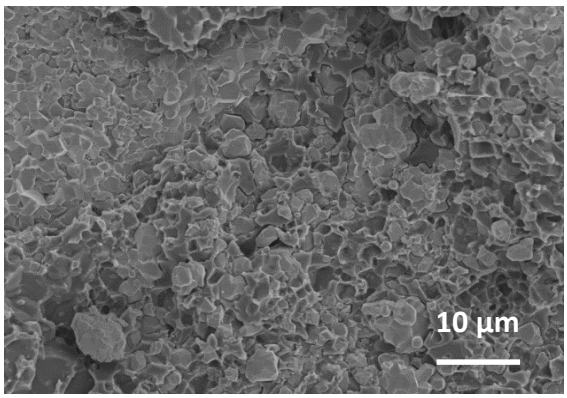

FIG. 4.3. SEM image of the fractured cross-section of a NiZn ferrite/epoxy composite with a 53 vol.% ferrite loading.

The frequency responses of the complex permeability and permittivity from 5 MHz to 2 GHz at each volume fraction are plotted in Fig. 4.4. For polycrystalline ferrite, the magnetization mechanisms are generally considered to be spin rotation in the magnetic domains and domain wall motion.[19,20] In Fig. 4.4(a) for no ferrite addition, the real permeability μ' remained at approximately 1 over the measured frequency range, as expected, and the permittivity was constant at ~ 3, in good agreement with data book values. Figs. 4.4(b-d) show the effects of 11 vol. %, 32 vol. % and 53 vol. % NiZn ferrite respectively, with the low frequency μ' response (<200 MHz) approximately constant before decreasing as the frequency increased (>200 MHz). The imaginary

permeability μ'' remained relatively low in the range 0.01 to 0.2 below several tens of MHz, but increased at higher frequencies to form a broad peak with a maximum at around the frequency at which μ' dropped to approximately half its plateau value (Figs. 4.4(b-d)).[5,21] The increase of μ'' was mainly due to domain wall motion no longer following the applied alternating magnetic field.[22]

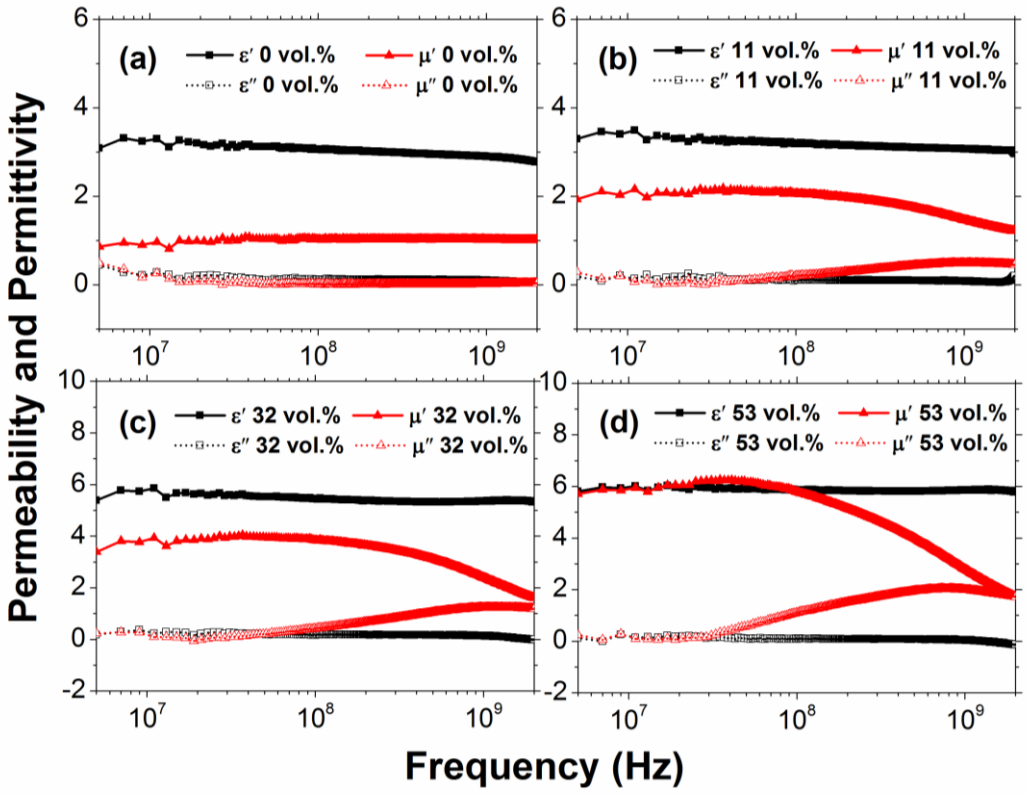

FIG. 4.4. Frequency dispersions of complex permeability and permittivity for samples with (a) 0 vol.% , (b) 11 vol.% , (c) 32 vol.%, and (d) 53 vol.% of NiZn ferrite. The slight drop in permittivity at the lowest frequency was due to the measurement instrument at its lower working frequency limit.

In order to consider if these variations conform to expected behaviours, a magnetic circuit model[23] was applied. This model accounted for the way in which the non-

magnetic matrix creates magnetic poles on the surface of ferrite grains/particles under an applied magnetic field, thus producing demagnetizing fields, which lead to a decrease in permeability. The magnitude of the demagnetizing field is closely related to the ferrite grain/particle size and non-magnetic phase characteristic. The composite static permeability μ_s that corresponds to the real permeability at frequencies far below any resonant response is assumed to vary according to:[23]

$$\mu_s = \frac{\mu_i(1+(\delta/D))}{1+\mu_i(\delta/D)} = 1 + \frac{\mu_i - 1}{1+\mu_i(\delta/D)} \tag{4.1}$$

where μ_i is the intrinsic static permeability of a ferrite without any defects, δ is the distance between grains/particles (in other words, it is the thickness of non-magnetic phases), and D is the grain/particle size. With increasing vol.% of ferrite, the corresponding decrease in adjacent particle distance δ will lead to a decrease in the ratio δ/D, thus increasing static permeability μ_s. Assuming that the ferrite particles were spherical and homogeneously distributed in the epoxy matrix (a reasonable but not perfect assumption, consistent with the observed microstructure), the experimentally derived value of μ_s taken at a frequency of 10 MHz can be plotted against the δ/D ratio derived from the volume fraction of ferrite, as shown in Fig. 4.5. Using a best-fit of $\mu_i = 40$ (which is a sensible reduction from the ferrite manufacturer's supplied value of $\mu_i = 120$ for identical material but in sintered "bulk"[24-26]), Fig. 4.5 shows that static permeability increased with decreasing adjacent particle distance, in close agreement with Eq. (4.1).

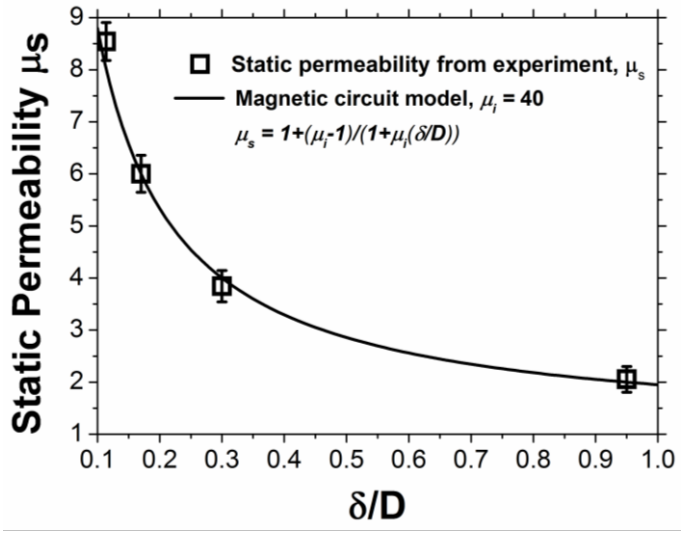

FIG. 4.5. The experimentally measured static permeability μ_s (as obtained from Fig. 4.4) as a function of the particle separation ratio δ/D, assuming homogeneously dispersed, spherical ferrite filler particles.

The permittivity response of NiZn ferrites is provided by atomic and electronic polarization, which was largely independent of frequency in the range 5 MHz to 2 GHz used here, with both real and imaginary permittivities almost constant over the range.

Because permeability increased more rapidly than permittivity due to the greater inherent permeability of the ferrite filler, at 53 vol.% ferrite in Fig. 4.4(d) the permeability and permittivity were approximately equal, and remained so until a cut-off frequency of ~100 MHz, beyond which μ' began to reduce.

As described in Chapter 2, the Lichtenecker mixing formula[27] has proven to be a flexible and widely applicable approach for estimating the effective permeability and permittivity medium of composite systems. It provided reasonable agreement to the

data here and identified the ferrite fraction for impedance matching. The general formula for a two-component mixture is:

$$\log(\psi_{eff}) = f \log(\Psi_i) + (1-f)\log(\Psi_m) \tag{4.2}$$

where Ψ_{eff}, Ψ_m and Ψ_i represent either the complex permeability or permittivity of the effective medium, the matrix and the fillers respectively, and f is the volume fraction of filler. Fig. 4.6 shows a direct comparison of the experimental data for μ'_{eff} and ε'_{eff} for the ferrite composites at 10 MHz along with their predicted values using Eq. (4.2) by substituting into the matrix and filler properties $\mu'_m = 1$, $\varepsilon'_m = 3$, $\mu'_i = 40$ (as used in Fig. 4.5) and $\varepsilon'_i = 13$, which were based on data supplied by the ferrite manufacturer. A frequency of 10 MHz was chosen because the measured complex permeability and permittivity were largely non-dispersive at this frequency. Experiment and theory show reasonable agreement over the range. Deviations from theory may arise due to agglomeration effects, limited porosity (air bubbles), and lack of precise control over volume fraction. Fig. 4.6 shows the real permeability and permittivity curves predicted by the Lichtenecker formula were coincident at ~ 6 for a ferrite volume around 50 vol.%, which was in accord with the experimental results obtained at 53 vol.%.

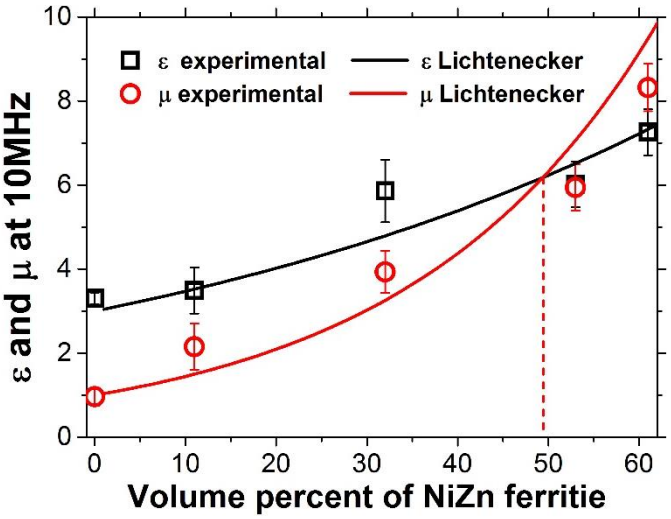

FIG. 4.6. The effective real permeability and permittivity at 10 MHz as a function of volume percent NiZn ferrite in an epoxy matrix and the predicted dependence with volume fraction of ferrite using the Lichtenecker approximation.

Fig. 4.7 shows the experimentally measured reflectivity and transmissivity from the $Ni_{0.4}Zn_{0.6}Fe_2O_4$/epoxy composite with a 53 vol. % loading as a function of frequency. The material transmitted more than 96% of the incident power, while maintaining a reflection coefficient of less than 0.03% for frequencies up to 100 MHz, showing superior performance over a recent report on array structured impedance matched materials that have 80% transmission and 0.3% reflection at 100 MHz for only orthogonal linear polarized radiation.[28] The transmission reduced significantly above 100 MHz due to losses caused by magnetic resonance.

The extracted values of refractive index, reduced impedance, and magnetic and dielectric loss tangents for a 53 vol. % ferrite loading composite are plotted in Fig. 4.8. The permeability and permittivity were almost equal up to a frequency of

approximately 100 MHz, which resulted in an impedance ($Z = \sqrt{\mu_0 \mu' / \varepsilon_0 \varepsilon'} = Z_0 \sqrt{\mu' / \varepsilon'} = Z_0$) close to that of free space and a refractive index of approximately 6.

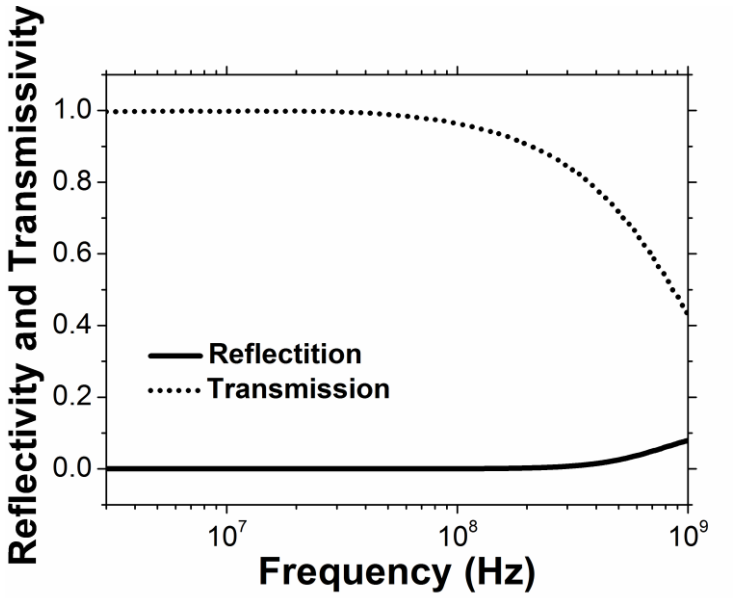

FIG. 4.7. Experimentally determined reflectivity and transmissivity from an epoxy/53 vol.% $Ni_{0.4}Zn_{0.6}Fe_2O_4$ composite.

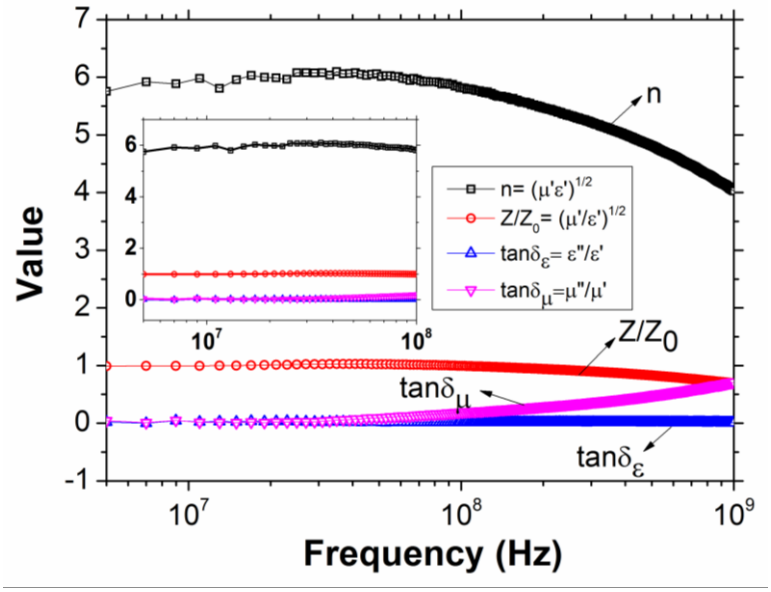

FIG. 4.8. Refractive index, reduced impedance, dielectric and magnetic loss tangents of a 53 vol. % ferrite/epoxy composite. The inset shows the results in the range 5-100 MHz.

For antenna miniaturization applications, broadband impedance matched materials with high refractive index $n=(\mu\varepsilon)^{1/2}$ are preferable since the electrical length of an antenna is the product of its physical length and the antenna medium refractive index.[2] Hence, the physical dimension of an antenna made from this material could be reduced by a factor of ~ 6 over materials with n = 1 without changing the effective electrical length. In addition, the materials with equal permeability and permittivity minimize the antenna problems of strong field confinement[29] and mismatched impedance with free space.

Any electrically small antenna will tend to have a narrow operational bandwidth, and in order to maximize the bandwidth, the antenna can be enclosed within a spherical volume such that it efficiently diminishes the fields within the radiation sphere

circumscribing the antenna.[30,31] There have been a wide variety of novel geometrical designs enabling resonant antenna elements to be encased within such an electrically small volume,[32 -35] but easily processable materials with acceptable mechanical properties become crucial in realizing these designs in practice. In particular, it is difficult and expensive to achieve various curved surface designs using comparatively brittle and difficult to machine bulk ferrites. In contrast, it was straight-forward to cast the composites into desired geometries, even at high ferrite loadings. For example, Fig. 4.9 shows an impedance-matched epoxy-53 vol.%NiZn ferrite cast into hemispheres according to the design of an electrically small folded spherical helix antenna.[32]

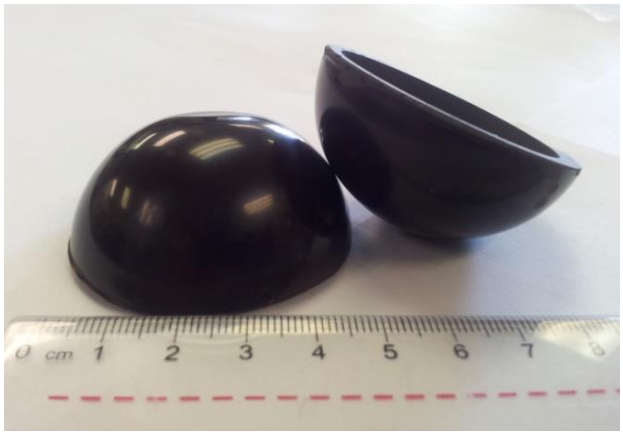

FIG. 4.9. Hemisphere shells with 5 cm diameter and 5 mm wall thickness, cast from an impedance-matched epoxy-53 vol.% NiZn ferrite composite.

4.1.4 Conclusions

A simple mould casting method for producing ferrite/epoxy composites has been developed that allows materials with a matched permeability and permittivity of ~ 6 and reflection less than 0.03% over the frequency range 5-100 MHz to be produced using 53 vol.% $Ni_{0.4}Zn_{0.6}Fe_2O_4$ powder. The experimental results for both permeability and permittivity accord well with the Lichtenecker formula, enabling it to be used to explore impedance matched materials with a variety of different filler materials via a composite approach. The epoxy based composites were easy to process, scalable, machinable and could be directly cast into 3D geometries, with similar or improved performance over monolithic, complex composition sintered ferrites, providing more freedom for antenna miniaturisation. The results show the utility of a generic approach for achieving impedance matched materials, without the need for subtle thermal manipulations of complex composition materials. Further it is suggested that any magnetic material with permeability higher than permittivity can provide an impedance match by tuning of the material fractions in the composite fabrication route.

4.2 NiZn ferrite/Fe Hybrid Epoxy-based Composites: Extending Magnetic Properties to High Frequency

4.2.1 Introduction

As previously described, the ever-increasing demand for smaller, longer lasting and novel design portable electronic devices has accelerated the development of multifunctional materials with low energy losses and high permeability for miniaturizing electronic components such as antennas, magnetic inductors[36] and current convertors.[37-39] Many of these devices operate in the very high frequency (30-300 MHz) range, such as television broadcasting, land-based mobile telephone stations and air traffic control communications, and therefore materials with low energy losses and high permeability that are able to operate at these and higher frequencies are in high demand, both for conventional and possible metamaterial applications.[40-42] Following the results described in the previous section, which showed encouraging performance of cast epoxy/ferrite composites, but only in a frequency band somewhat at the lower end of that required commercially, options to extend attractive behavior to higher frequency were explored.

According to Snoek's law $\mu f_r \propto M_s$ (where μ is the real permeability, f_r is the ferromagnetic resonant frequency and M_s is the saturation magnetization), magnetic materials with high M_s are favored for high permeability at high frequencies.

Therefore, metallic magnetic materials that are known to have high saturation magnetization have been investigated as fillers embedded in easy-to-process non-conducting polymer matrix – magnetic composites. The magnetic properties of metallic fillers has been improved by using planar, anisotropic morphologies, extending useful operation characteristics up to a few gigahertz, such as those based on carbonyl iron flakes,[43,44] planar $Fe_{50}Ni_{50}$ powder,[45] $Fe_{65}Co_{35}$ thin films,[46] and $Fe_{74}Cr_2Mo_2Sn_2P_{10}Si_4B_4C_2$ flakes.[47] However, these composites have tended to have high dielectric losses ($\tan\delta_\varepsilon \geq 0.1$), which is generally considered undesirable for device applications.

Soft magnetic ferrites have low dielectric losses ($\tan\delta_\varepsilon \sim 10^{-2}$) but magnetic properties are degraded or even absent (i.e. materials with permeability close to 1) as the frequency approaches the range 100 MHz to 1 GHz,[14] due to ferromagnetic resonant behaviour, which limits the device operating frequency – as explored in the previous section. Metallic magnetic materials generally have higher resonant frequency than ferrites due to their larger saturation magnetization, but suffer from high energy losses because of induced eddy currents, creating difficulties in the design and engineering of practical devices using these materials.[48] Merging the characteristics of these two kinds of magnetic materials might produce an attractive balance of properties, depending on the frequencies at which magnetic response might be maintained while at comparatively low loss.

In this section, the simple mould casting method described in the precious section to fabricate epoxy based NiZn ferrite/Fe hybrid composites is extended by investigating

electromagnetic properties of two series of hybrid composites composed of ball milled and un-milled $Ni_{0.4}Zn_{0.6}Fe_2O_4$ ferrite and Fe particles, with various composition ratios. A co-axial air-line technique is used to characterize the complex permittivity and permeability of the composites in the frequency range 10 MHz to 4 GHz. Ball milling is shown to reduce dielectric loss dramatically, compensating for the losses normally associated with introducing Fe. The electromagnetic properties of an optimized hybrid epoxy-based composite with ball milled 15 vol.% NiZn ferrite and 38 vol.% Fe fillers is demonstrated to be significantly better than similar ferrite-only containing composites, suggesting promise for magnetic applications in the high frequency range.

4.2.2 Experimental

The same sintered $Ni_{0.4}Zn_{0.6}Fe_2O_4$ ferrite powder (F16 MagDev Ltd. UK) was used, but this time together with Fe powder (<10 μm, Alfa Aesar Ltd. UK), and were ball milled for 4 hours in a high-energy planetary mill (Pulverisette 6, Fritsch GmbH, Germany) at a rotational speed of 300 rpm with a ball-to-powder weight ratio of 10:1 in ethanol, and then dried. Table 1 shows the range of ferrite/Fe mass ratios investigated.

Magnetic composites were again prepared using an epoxy matrix (Epon™ 812 substitute) with two different hardeners: 2 dodecenylsuccinic anhydride (DDSA) and methylnadic anhydride (NMA) (Sigma Aldrich Ltd. UK), by casting route previously described. By changing the ratio of the two hardeners, the hardness and brittleness of the final cured epoxy could be adjusted. After extended magnetic stirring of the epoxy

mixture, the accelerator 2,4,6-tris(dimethylaminomethyl) phenol (DPM-30) was added, and then the filler powders (see Table 4.1) under stirring, followed by 5 min ultrasonication in an ice bath. The composite slurry was then degassed under low vacuum and poured into a silicone mould to produce a ring-shaped casting with an outer diameter of 7.0 mm, an inner diameter of 3.04 mm, and a thickness of 7.0 mm. These dimensions were chosen to fit tightly within a co-axial air-line jig for electromagnetic measurements. The composites were cured at 60 °C overnight.

Table 4.1. Compositions of epoxy-based composites containing both ball milled and as-supplied powder fillers.

Sample	Composition	Fe/(Fe + NZ) Vol. ratio
53NZ	53 vol.% NiZn ferrite	0
48NZ5Fe	48 vol.% NiZn ferrite/5 vol.% Fe	0.094
42NZ11Fe	42 vol.% NiZn ferrite/11 vol.% Fe	0.207
38NZ15Fe	38 vol.% NiZn ferrite/15 vol.% Fe	0.283
26.5NZ26.5Fe	26.5 vol.% NiZn ferrite/26.5 vol.% Fe	0.5
15NZ38Fe	15 vol.% NiZn ferrite/38 vol.% Fe	0.717
11NZ42Fe	11 vol.% NiZn ferrite/42 vol.% Fe	0.793
5NZ48Fe	5 vol.% NiZn ferrite/48 vol.% Fe	0.906
53Fe	53 vol.% Fe	1

Scanning electron microscopy (SEM) images were taken using a JEOL JSM-840F field emission electron microscope after microtome (Ultracut E, Reichert, Inc.) cross-sectioning. The reflection and transmission amplitude coefficients were measured from 10 MHz to 4 GHz in the co-axial air-line jig by a calibrated vector network analyser (MS4644A, Anritsu). The complex permittivity and permeability of the material were then again extracted from the reflection and transmission coefficients using the Nicolson-Ross-Weir equation.

4.2.3 Results and Discussion

Figs. 4.10(a) and (b) show SEM images of the as-supplied Fe powder and the NiZn ferrite powder respectively, with comparable particle dimensions of 1 to 10 μm. After ball milling, as shown in Fig. 4.10(c), the spherical Fe particles were deformed into flakes with lateral dimensions of a few micrometers and sub-micrometer thickness. The NiZn ferrite particles were ground to sub-micrometer diameter and became distributed evenly on the surface of Fe flakes, as "satellites". Fig. 4.10(d) shows a typical fractured cross-section of a 15 vol.% NiZn ferrite and 38 vol.% Fe hybrid composite, indicating an adequate homogeneity of filler particle dispersion with no large agglomerates or excessive air bubbles.

The complex permittivity and permeability of the NiZn ferrite/Fe epoxy-based composites with as-received fillers, and that with ball milled fillers, with different volume ratios are shown in Fig. 4.11 and Fig. 4.12 respectively. The real part (ε') and imaginary part (ε'') of relative permittivity for the composites with as-supplied and milled fillers increased with Fe volume ratio, most notably at low frequencies for composites with a high Fe fraction (> 38 vol. % for as-supplied, > 42 vol.% for ball milled) due to the high electrical conductivity of Fe and the charge accumulation at the interfaces between the Fe and the matrix, which is known as interfacial polarization.[48] At the lower frequencies, the charges had sufficient time to accumulate at the interfaces and tended to orientate fully along the applied field direction, enhancing charge movement and increasing energy dissipation. At low Fe fraction, the permittivities of both types of composites were almost constant at < 20 in the 10

MHz to 4 GHz frequency range. In general, the values of ε' and ε'' for composites with milled fillers were lower and less dispersive than those of composites with as-supplied fillers at the same composition, because for the ball milled filler composites the smaller sub-micrometer ferrite particles that decorated the Fe flakes acted as physical "spacers" that improved the partial insulation of Fe by facilitating the ingress of the epoxy matrix between the Fe flakes, as suggested by the microstructural observations in Fig. 4.10(d). On the other hand, without milling, the aggregated as-supplied Fe particles were generally not well-separated or isolated, and the similarly sized as-supplied NiZn ferrites did not form satellites on the Fe, thus there was no effective physical mechanism to inhibit a greater extent of Fe agglomeration. The composites based on as-supplied powder therefore showed a higher complex permittivity and were more "lossy".

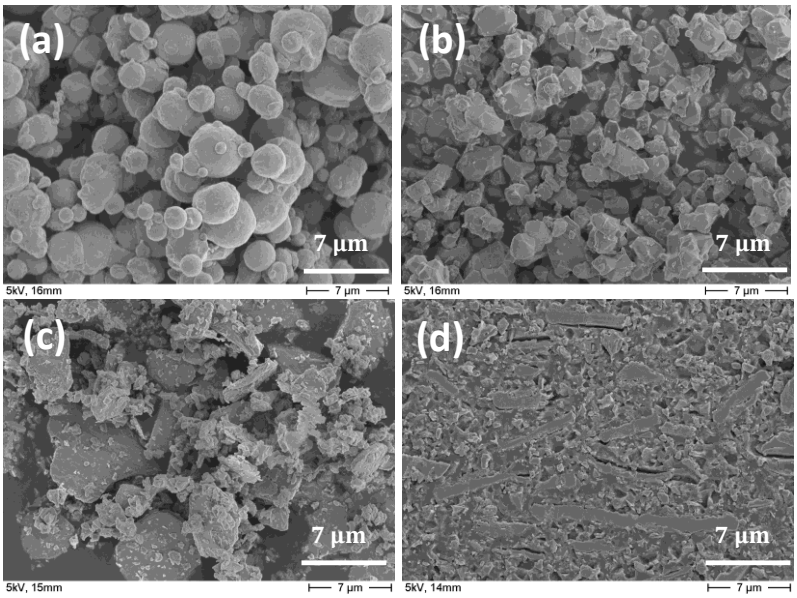

FIG. 4.10. SEM images of (a) as-supplied Fe particles; (b) as-supplied NiZn ferrite; (c) 15 vol.% NiZn ferrite/38 vol.% Fe powder mixture after ball milling; and (d) a cross-section of a 15 vol.% NiZn ferrite/38 vol.% Fe hybrid composite.

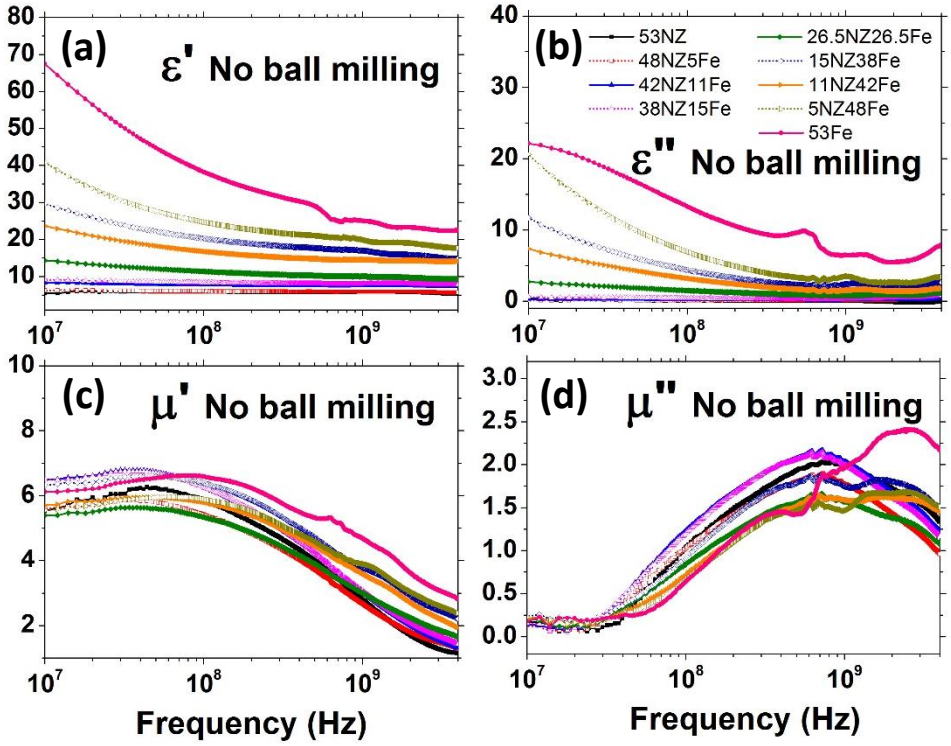

FIG. 4.11. Complex permittivity and permeability spectra for composites with un-milled NiZn ferrite/Fe fillers in various volume ratios: (a) real and (b) imaginary part of complex permittivity; and (c) real and (d) imaginary part of complex permeability.

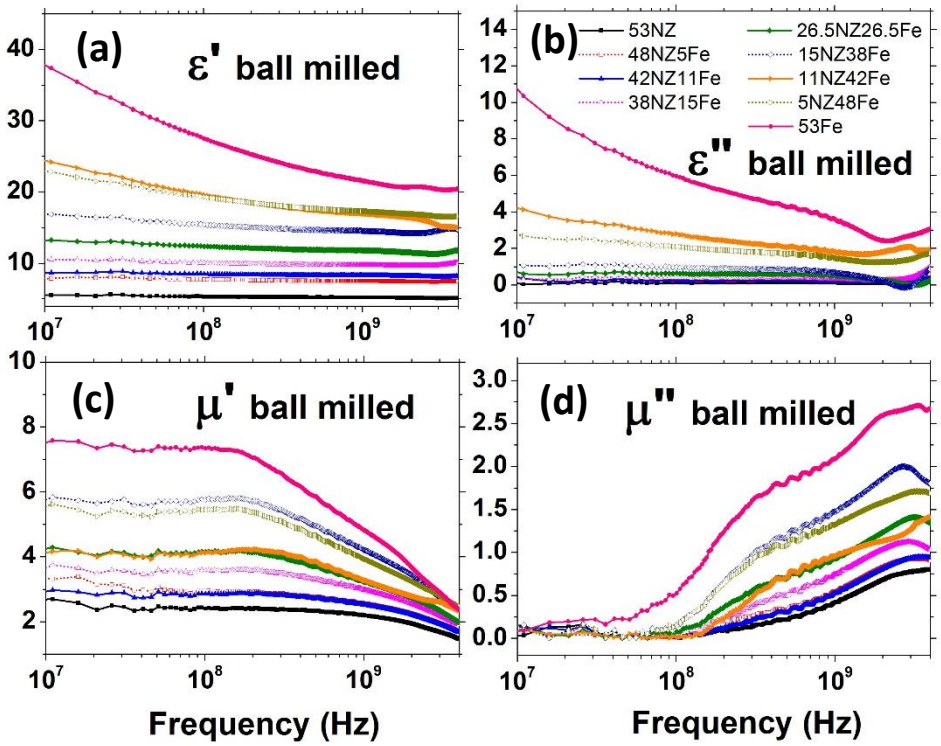

FIG. 4.12. Complex permittivity and permeability spectra for composites with ball milled NiZn ferrite/Fe fillers in various volume ratios: (a) real and (b) imaginary part of complex permittivity, and (c) real and (d) imaginary part of complex permeability.

In general, the real part of complex permeability μ' for both types of composites with various filler ratios responded similarly, with a flat response at low frequency before gradually decreasing as frequency increased. The imaginary part of complex permeability μ'' remained relatively low at 0.01 to 0.3 below several tens of MHz, but increased to form a broad peak around the resonant frequency, where as previously described, domain wall motion was no longer able to follow the applied alternating magnetic field and magnetic loss increased.[20]

The real permeability of all the epoxy-based composites containing as-supplied NiZn ferrite/Fe fillers were comparable at ~ 6 at low frequency, but decreased more rapidly for composites with higher NiZn ferrite volume fractions because of the smaller saturation magnetization of the NiZn ferrite (see Fig. 4.11(c)). At a frequency of 4 GHz, the 53 vol.% Fe composite had the highest permeability of 3, whereas the real permeability of the 53 vol.% NiZn ferrite composite had reduced to 1.5.

For the composites with ball milled fillers, the real permeability decreased from ~ 7.5 to ~ 2.5 with increasing NiZn ferrite fraction, as shown in Fig. 4.12(c), which was attributed to the lower permeability of the smaller NiZn ferrite particles: smaller ball milled ferrite particles have lower permeability because they contain more defects that pin domain walls.[24] The effective permeability may also have been lowered by a higher demagnetizing field in the composite evoked by the larger gaps between smaller particles when compared with larger particles at the same volume fraction.[24] The real permeability of the 53 vol. % milled Fe composite was ~ 7.5 before resonance occurred, compared with ~ 6 for the 53 vol.% as-supplied Fe composite, and was ascribed to the thin (< 1 μm) flake morphology after milling that has previously been suggested to reduce eddy current loss.[49]

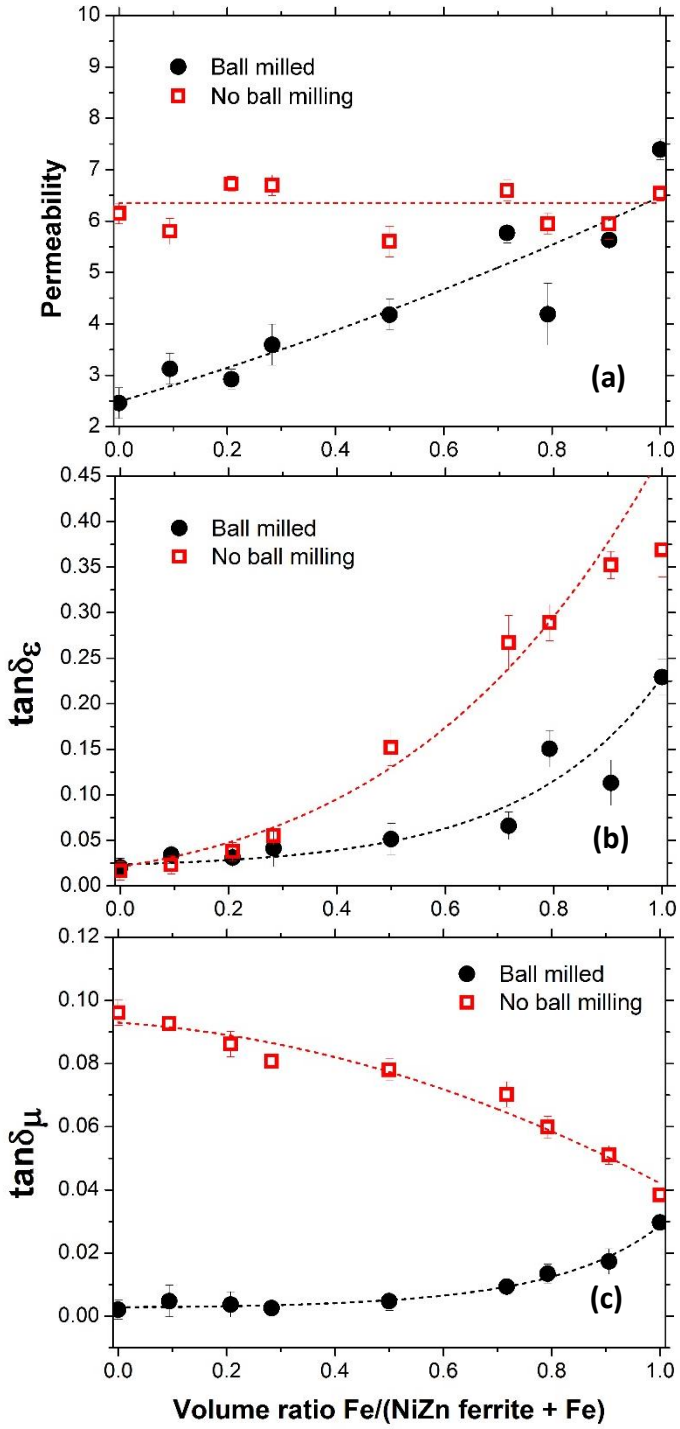

FIG 4.13. The (a) real part of complex permeability, (b) dielectric loss tangent, and (c) magnetic loss tangent of epoxy-based composites with ball milled and un-milled NiZn ferrite/Fe fillers in various volume ratios at 50 MHz.

Fig. 4.13 shows the real permeability, dielectric loss tangent ($tan\delta_\varepsilon = \varepsilon''/\varepsilon'$) and magnetic loss tangent ($tan\delta_\mu = \mu''/\mu'$) of composites with milled and as-supplied fillers at various Fe/total filler volume ratios at 50 MHz. In all cases the total amount of filler was 53 vol.% of the epoxy-based composite, but the Fe/(Fe+NiZn ferrite) ratio changed systematically. The values of μ', $tan\delta_\varepsilon$ and $tan\delta_\mu$ for as-supplied powders were almost constant at ~ 6, increased from 0.016 to 0.370, and decreased from 0.096 to 0.038 respectively as the Fe/(Fe+NiZn ferrite) ratio increased from 0 to 1. After ball milling, μ', $tan\delta_\varepsilon$ and $tan\delta_\mu$ increased from 2.5 to 7.5, 0.02 to 0.22, and 0.002 to 0.03 respectively over the same range. Therefore, both dielectric and magnetic losses were reduced systematically when a ball milling pre-treatment was used.

For electronic device components and especially antennas, low dielectric and magnetic losses combined with high permeability are especially desirable, but become more mutually exclusive as frequency increases for monolithic materials. However in the case of the composites investigated here, an optimum balance between high permeability ($\mu' = 5.8$) and low energy losses ($tan\delta_\varepsilon = 0.06$ and $tan\delta_\mu = 0.009$) can be identified at a Fe/(Fe+NiZn ferrite) volume ratio of 0.717 (15 vol.% NiZn ferrite and 38 vol.% Fe) for the ball milled filler composites.

A direct comparison of the complex permittivity and permeability spectra for epoxy-based composites with ball milled and as-supplied fillers of 15 vol.% NiZn ferrite/38 vol.% Fe are shown in Figs. 4.14(a) and (b) respectively, where the ε' and ε'' response decreased and flattened after the ball milling process, as previous described. The slightly more frequency-independent permeability of the composite with milled

powders reduced from 6.6 to 5.8 as frequency increased, but dielectric and magnetic loss tangents were suppressed to $\leq 10^{-2}$ up to 150 MHz, providing a wider practical operating bandwidth than composite variants containing as-supplied powders only at the same ratio, or for the ferrite-only containing composite.

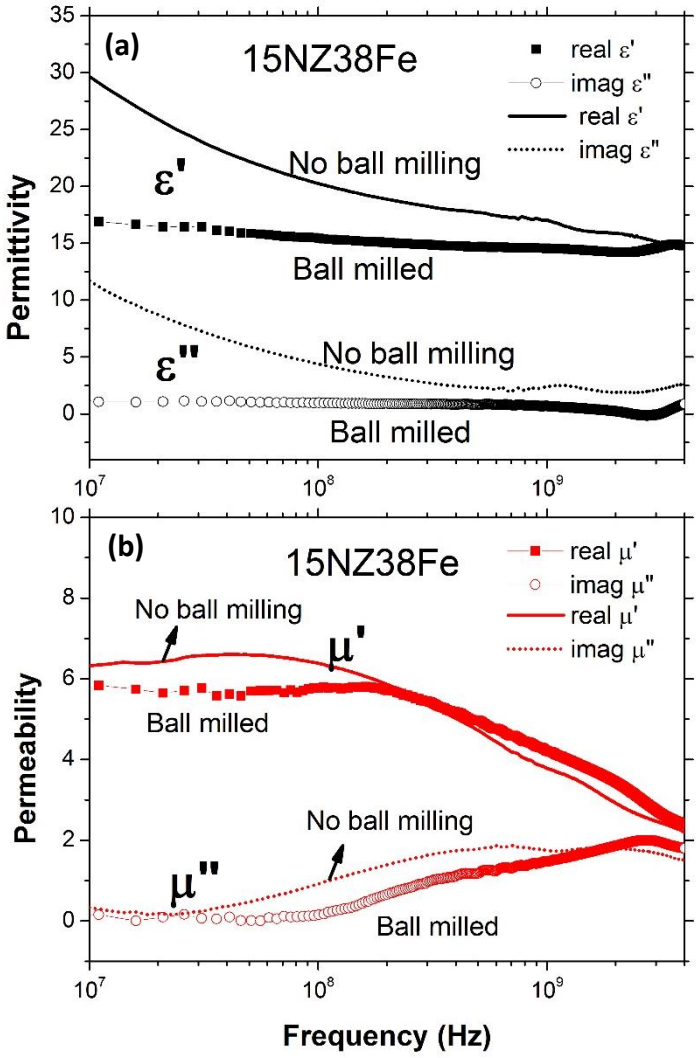

FIG. 4.14: Frequency dispersions of (a) complex permittivity and (b) complex permeability for epoxy-based composites with ball milled and un-milled particle fillers of 15 vol.% NiZn ferrite/38 vol.% Fe.

To further assess the benefit of the hybrid 15 vol.% NiZn ferrite/38 vol.% Fe hybrid composite over a similar composite containing only as-supplied NiZn ferrite with same overall filler fraction, their magnetic properties are shown in Fig. 4.15. Both composites have a comparable real permeability of ~ 6 up to 30 MHz, but whereas permeability then reduced for the NiZn ferrite only composite, the hybrid composite maintained a higher permeability to ~ 300 MHz.

Although the real permeability of the ball milled 15 vol.% NiZn ferrite/38 vol.% Fe hybrid composite was slightly lower than un-milled 53 vol.% NiZn ferrite alone at lower frequency, an important figure of merit is the magnetic quality factor $Q = \mu'/\mu''$, which is plotted as a function of frequency in Fig. 4.16. Q was significantly improved over the measured frequency range in the case of the hybrid composite, indicating a more practical balance of permeability and loss behaviour, especially at higher frequencies.

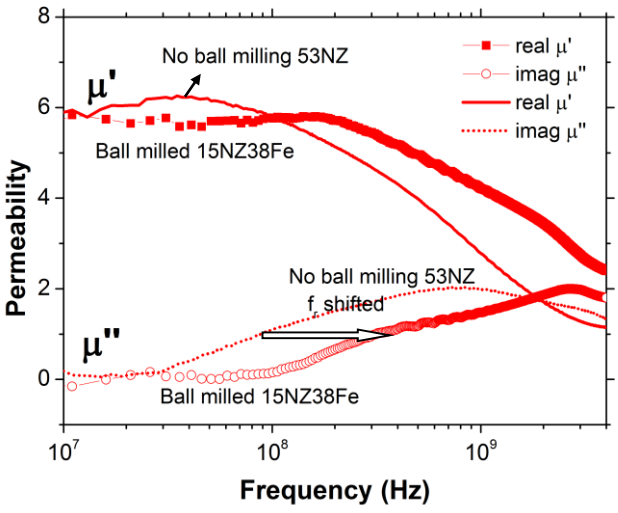

FIG. 4.15. Frequency dispersions of complex permeability for epoxy-based composites with a un-milled 53 vol.% NiZn ferrite loading and a ball milled 15 vol.% NiZn ferrite/38 vol.% Fe loading. The hybrid composite showed permeability similar to the ferrite only composite, but with extended operating bandwidth.

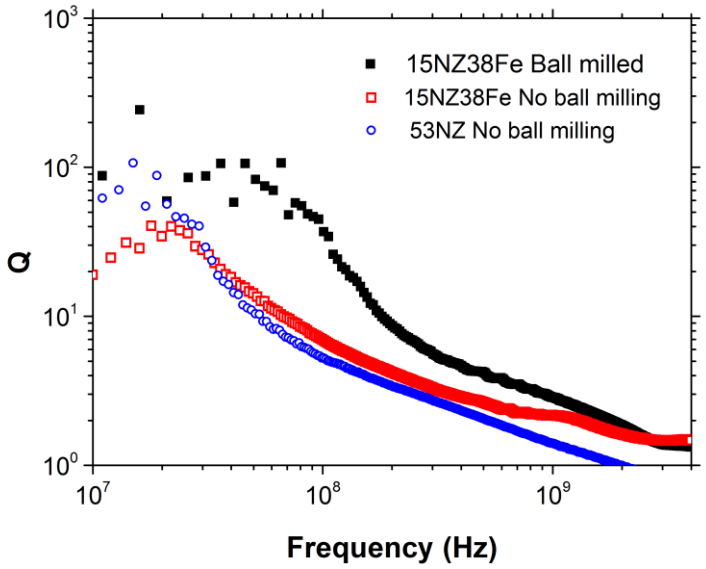

FIG. 4.16. Quality factor Q versus frequency for epoxy-based composites with ball milled 15 vol.% NiZn ferrite/38 vol.% Fe, un-milled 15 vol.% NiZn ferrite/38 vol.% Fe, and un-milled 53 vol.% NiZn.

4.2.4 Conclusions

The electromagnetic properties of epoxy-based composites containing both ball milled and un-milled NiZn ferrite and Fe particulate fillers were investigated over the frequency range 10 MHz - 4 GHz. The changes in size and morphology of the particles that were introduced by the ball milling process suppressed dielectric and magnetic losses of the NiZn ferrite/Fe hybrid composites to higher frequencies due to reduced eddy current loss. A hybrid composite with a filler loading of ball milled 15 vol.% NiZn ferrite/38 vol.% Fe showed an almost one order of magnitude improvement in operating frequency with low loss when compared with a similar but un-milled 53 vol.% NiZn ferrite composite, with only a slight reduction in permeability. The striking

points of the hybrid composites were a relatively high permeability (~ 6) and low magnetic and dielectric losses (~ 10^{-2}) over the high frequency range of interest, which suggested they may be well-suited for applications in electrically small devices operating in this frequency range. The addition of Fe to NiZn ferrite can also be expected to lower the fabrication cost for a given filler content, and improved loss performance over solely ferrite containing composites. The ease of casting these epoxy based composites into a range of shapes and sizes further enhances the attractiveness of these materials. The concept of manipulating permeability and permittivity of easy-to-process composites by introducing multi-phase ferromagnetic materials with contrived morphologies and size ratios may also help to advance applications such as cloaking, energy transfer, sensors and security according to the theory of spatial transformations, which relies on the provision of bespoke dielectric and magnetic properties in practical materials.

Bibliography

1 L. B. Kong, Z. W. Li, G. Q. Lin, and Y. B. Gan, J. Am. Ceram. Soc. **90**, 3106 (2007).

2 M. L. S. Teo, L. B. Kong, Z. W. Li, G. Q. Lin, and Y. B. Gan, J. Alloy Compd. **459**, 557 (2008).

3 W. Yu, R. Mittra, and D. H. Werner, IEEE Microw. Guided Wave Lett. **9**, 496 (1999).

[4] W. Yu, D. H. Werner, and R. Mittra, IEEE Microw. Guided Wave Lett. **10**, 128 (2000).

[5] A. Thakur, P. Thakur, and J. -H. Hsu, Scripta Mater. **64**, 205 (2011).

[6] A. Thakur, A. Chevalier, J. -L. Mattei, and P. Queffélec, J. Appl. Phys. **108**, 014301 (2010).

[7] D. Souriou, J. -L. Mattei, A. Chevalier, and P. Queffélec, J. Appl. Phys. **107**, 09A518 (2010).

[8] H. Su, X. Tang, H. Zhang, Y. Jing, F. Bai, and Z. Zhong, J. Appl. Phys. **113**, 17B301 (2013).

[9] L. B. Kong, Z. W. Li, G. Q. Lin, and Y. B. Gan, IEEE Trans. Magn. **43**, 6 (2007).

[10] Q. He, T Yuan, X. Zhang, X. Yan, J. Guo, D. D. Ding, M. A. Khan, D. P. Young, A. Khasanov, Z. Luo, J. Liu, T. D. Shen, X. Liu, S. Wei, and Z. Guo, J. Phys. Chem. C **118**, 24784 (2014).

[11] J. Zhu, S. Wei, N. Haldolaarachchige, D. P. Young, and Z. Guo, J. Phys. Chem. C **115**, 15304 (2011).

[12] Z. Guo, S. Park, H. T. Hahn, S. Wei, M. Moldovan, A. B. Karki, and D. P. Young, J. Appl. Phys. **101**, 09M511 (2007).

[13] W. Barry, IEEE Trans. Microwave Th. Tech. **34**, 80 (1986).

[14] L. Parke, I. R. Hooper, R. J. Hicken, C. E. J. Dancer, P. S. Grant, I. J. Youngs, J. R. Sambles, and A. P. Hibbins, APL Mater. **1**, 042108 (2013).

[15] W. B. Weir, Proc. IEEE **62** (1), 33 (1974).

[16] A. M. Nicolson and G. F. Ross, IEEE Trans. Instrum. Meas. **19** (4), 377 (1970).

[17] M. J. Lancaster, J. Powell, and A. Porch, Supercond. Sci. Technol. **11**, 1323 (1998).

[18] N. Gupta, A. Verma, S. C. Kashyap, and D. C. Dube, J. Magn. Magn. Mater. **308** (1), 137 (2006).

[19] A. Globus, J. Phys. Colloques. **38**, C1 (1977).

[20] H. Su, H. Zhang, X. Tang, and Y. Jing, J. Appl. Phys. **103**, 093903 (2008).

[21] R. E. Alley Jr., Bell Syst. Tech. J. **32**, 5 (1953).

[22] H. Dawoud and S. Shaat, An-Najah Univ. J. Res. (N.Sc). **20**, 87 (2006).

[23] M. T. Johnson and E. G. Visser, IEEE Trans. Magn. **26**, 1987 (1990).

[24] M. Anhalt, J. Magn. Magn. Mater. **320**, 366 (2008).

[25] Z. W. Li, G. Q. Lin, Y. P. Wu, and L. B. Kong, J. Magn. Magn. Mater. **321**, 734 (2009).

[26] N. E. Kazantseva, J. Vilcakova, V. Kresalek, P. Saha, I. Sapurina, and J. Stejskal, J. Magn. Magn. Mater. **269**, 30 (2004).

[27] K. Lichtenecker and Rother K., Phys. Z. **32**, 255 (1931).

[28] L. Parke, I. J. Youngs, A. P. Hibbins, and J. R. Sambles, Appl. Phys. Lett. **104**, 221905 (2014).

[29] H. Mosallaei and K. Sarabandi, IEEE Trans. Antennas Propagat. **52**, 1558 (2004).

[30] L. J. Chu, J. Appl. Phys. **10**, 1163 (1948).

[31] H. A. Wheeler, Proc. IRE **47**, 1325 (1959).

[32] S. R. Best, IEEE Trans. Antennas Propag. **52**, 953 (2004).

[33] S. R. Best, IEEE Antennas Propag. Mag. **46**, 9 (2004).

[34] S. R. Best, IEEE Trans. Antennas Propag. **53**, 502 (2005).

[35] S. R. Best, IEEE Antennas Propag. Mag. **53**, 1047 (2005).

[36] J. F. Godsell, S. Kulkarni, and T. O'Donnell, *J. Appl. Phys.* **107** (2010).

[37] M. Yamaguchi, Y. Miyazawa, K. Kaminishi, H. Kikuchi, S. Yabukami, K. I. Arai, and T. Suzuki, **268**, 170 (2004).

[38] Y. Hayakawa, A. Makino, H Fujimori, and A. Inoue, J. Appl. Phys. **81**, 3747 (1997).

[39] M. E. McHenry, M. A. Willard, H. Iwanabe, R. A. Sutton, Z. Turgut, A. Hsiao, and D. E. Laughlin, Bull. Mater. Sci. **22**, 495 (1999).

[40] T. Kasagi, T. Tsutaoka, and K. Hatakeyama, IEEE Trans. Magn. **35**, 3424 (1999).

[41] Y. W. Zhao, T. Zhang, and J. Q. Xiao, J. Appl. Phys. **93**, 8014 (2003).

[42] Y. W. Zhao, C. Y. Ni, D. Kruczynski, X. Zhang, and J. Q. Xiao, J. Phys. Chem. B **108**, 3691 (2004).

[43] R. B. Yang and W. F. Liang, J. Appl. Phys. **109**, 07A311 (2011).

[44] F. S. Wen, L. Qiao, H. B. Yi, D. Zhou, and F. S. Li, Chin. Phys. Lett. **25**, 751 (2008).

[45] J. Q. Wei, Z. Q. Zhang, R. Han, T. Wang, and F. S. Li, Chin. Phys. B **21**, 037601 (2012).

[46] Y. Wang, H. Geng, J. B. Wang, D. Nie, L. S. Wang, Y. Chen, and D. L. Peng, Appl. Phys. A, 569 (2013).

[47] K. H. Liu, T. C. Liu, J. L. Liu, L. Zhang, H. H. Zhang, D. R. Li, Z. C. Lu, and S. X. Zhou, Sci. China Ser. E **53**, 1056 (2010).

[48] J. R. Brauer, *Z. J.* Cendes, B. C. Beihoff, and K. P. Phillips, IEEE Trans. Ind. Appl. **36**, 1132 (2000).

Chapter 5

Electromagnetic Nanocomposite Films

This chapter introduces an approach to manufacture nanocomposite polymer-based films with tailored electromagnetic properties by spray deposition, which provides a thin, flexible format material for potential use in spatial transformation approaches to metamaterials devices. Multi-layer structured nanocomposite films with various nano-fillers are produced and their structures and properties are investigated. A polymer film permittivity and permeability measurement technique operating across a broadband microwave regime is developed based on a simple co-axial line method.

5.1 Spray Deposition of Nanocomposite Films

5.1.1 Introduction

As described in Chapter 4, one approach to produce materials with controlled ε and/or μ values involve controlling the positioning of inclusions in a matrix. Here, as an alternative to relatively large 3D "bulk" castings, a scalable spray processing approach

is used to form polymer-based nanocomposite films with well controlled dielectric and magnetic properties by embedding controlled and variable fractions of high dielectric permittivity and magnetic permeability particles in a polymer matrix.

For the spray deposition process, stable suspensions of nanoparticles with chosen ε or μ values are syringe-pumped at a controlled rate, atomized into droplets with compressed air and then continuously deposited onto a heated substrate, where the fugitive liquid is continually evaporated and there is no liquid build-up on the substrate. The photos and schematics of the spray deposition apparatus used in this thesis were previously shown in Chapter 3 (Figs. 3.3 and 3.4.) It was previously demonstrated in the group that using this spray deposition approach, polydiacrylate/$BaTiO_3$ nanocomposite films with moderate $BaTiO_3$ filler loadings of 10 – 30 vol.% could be fabricated, and a highest permittivity of ~ 39 was achieved but at relatively low frequency of ~ 1 kHz.[1] Fluoropolymer/multi-walled carbon nanotube composite films were also spray formed successfully that had high permittivity ~10^3 at a very low percolation threshold filler volume fraction of ~10^{-4},[2] but simultaneously showed a non-linear jump in loss and electrical conductivity close to the percolation threshold.

In this section, polymer-based nanocomposite films involving the assembling of nanoscale fillers and dielectric matrix materials into alternating multi-layer structures is undertaken, as shown in Fig. 5.1, rather than dispersing fillers in the matrix as was previously studied. The spray deposition route is explored for possibilities to vary electromagnetic properties through the thickness, and in concept, in-plane. The overall objective is to investigate, understand and demonstrate the platform process capability

of spray deposition with respect to the potential for tailoring of local permittivity and permeability in films by manipulating nanofiller concentration.

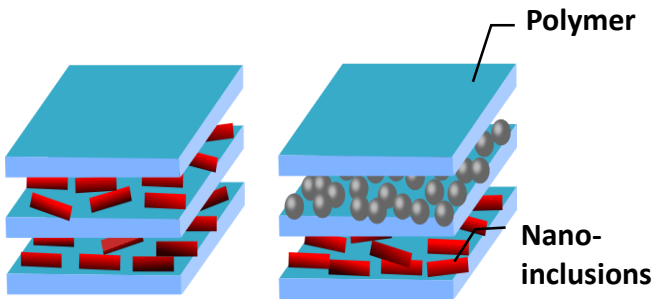

FIG. 5.1. Schematic of possible multi-layer nanocomposites.

5.1.2 Experimental

Fluoropolymer perfluoro alkoxy (PFA) (T_g = 306 °C, where T_g is the glass transition temperature) was chosen as the non-conductive polymer matrix into which dielectric and/or magnetic fillers could be added. PFA offers high temperature stability and mechanical robustness.[3] Most importantly, the as-supplied PFA was an aqueous suspension, allowing for ease of processing and handling in the spray deposition process. As-received PFA (Dyneon^{TM} PFA 6910GZ) according to the supplied datasheet comprised a 50 wt% solid aqueous dispersion with an average PFA particle size of 90 nm. The various suspensions (see later) were delivered to the spray nozzle by a syringe pump at a volumetric flow rate around 5 ml/min, atomised at a maximum pressure of 400 kPa, and sprayed onto a preheated glass substrate (95°C) using spray heights in the range 9.5 to 17.5 cm. The nozzle moved back and forth at 350 mm/s in a pre-programmed zig-zag pattern that repeated many times for deposition onto the heated substrate. The atomized droplets dried and formed a white powdery film on the

glass substrate that was then cured into a transparent film at 380°C for 30 min in a belt furnace (Dek Model840). A parametric study was carried out to investigate the optimum spray conditions to form relatively uniform and robust pure PFA films, before filler particles were subsequently added. Smoothness of the films was found to be a sensitive measure of the overall robustness and quality of the subsequently cured films. Two key spray parameters of atomising gas pressure and liquid volumetric flow rate were set to 140 kPa, 260 kPa and 400 kPa; and 2 ml/min, 5 ml/min and 8 ml/min, respectively, and 9 process combinations were studied in total. The thickness and surface roughness of the cured films were measured by surface profilometer (Dektak 6M) and confocal microscopy (NanoFocus μSurf) at 4 different positions.

Dispersions of multiwall carbon nanotubes (MWCNTs) that can provide a high permittivity[2] were chosen as a preliminary material to form a high permittivity layer sandwiched between two polymer-only layers. Although known to be lossy, the sandwich structure may inhibit current percolation across the film thickness; otherwise highly absorbing behavior might also be useful in some applications. The 1 mg/ml MWCNT suspensions suitable for spray forming were prepared by dispersing the MWCNTs (Baytubes C150P) in 1 wt% sodium dodecyl benzene sulfonate (SDBS) aqueous solution by ultrasonication (600W, 20 kHz) in an ice bath. The PFA/MWCNT/PFA nanocomposite films were then produced by initially spraying a layer of PFA only on the preheated slide glass substrate (95°C), followed by a layer of MWCNTs at a higher substrate temperature (110°C) and then a last layer of pure PFA again when the substrate was cooled (95°C), to form a "sandwich" structure. The resulting powdery gray-white film was cured into a translucent black film of thickness

60-70 μm at 380°C for 30 min in a belt furnace. Typically the thickness of each PFA layer and the MWCNT layer was 30 μm and 500 nm respectively.

As an extension of the permittivity effects of MWCNT additions, magnetite (Fe_3O_4) particles can induce a magnetic response in composite systems, and were introduced as a magnetic interlayer in a similar fashion, and were investigated for possible magnetic applications of polymer films. Fe_3O_4 nano-suspensions were prepared from ferrofluid (EMG 700, Ferrotec, USA). The ferrofluid comprised magnetic particles of 10 nm diameter dispersed in water at a particle concentration of 5.8 vol%. This as-received ferrofluid was 1:20 diluted with distilled water followed by ultrasonication to form low viscosity, sprayable suspensions, and PFA/Fe_3O_4/PFA multi-layer nanocomposite films then fabricated. The typical thickness of each pure PFA layer and the Fe_3O_4 nanoparticle layer were 30 μm and 300 nm respectively.

5.1.3 Results and Discussion

5.1.3.1 Parametric Study of Spray Process

Fig. 5.2 shows quantitatively the effect of atomising gas pressure and suspension flow rate on the thickness and surface roughness of pure PFA films after curing respectively. The error bars include the film thickness and roughness variations measured at four different positions (see Fig. 5.3) across each sample, which indicate the film uniformity under each single spray condition. The spray condition with smaller error bars on both film thickness and roughness is preferred for producing more uniform film. The film thickness at a 2 ml/min varied by up to 20 μm across the specimen,

because the relatively low flow rate produced intermittent atomisation "sputtering" and irregular deposition. Film uniformity was improved by using higher atomizing pressures so that atomisation was effectively continuous. The higher suspension flow rates resulted in more uniform films with well-controlled thickness. However, as the flow rate increased further to 8 ml/min, atomisation again became unstable and inconsistent because there was insufficient kinetic energy in the gas to atomize effectively the high suspension flow rate. In addition, the flow rate was so high that the fugitive water carrier could no longer be evaporated progressively and in balance with the rate of arriving liquid. Flaking occurred at the deposit edges where the excessive liquid tended to pool or "flood". A further problem was the blocking of the spray nozzle with the PFA particles at the highest flow rates. The thickness of the resulting films tended to be non-uniform after curing, and air bubbles started to present in thicker areas. Overall, the near-optimum suspension flow rate was chosen as 5 ml/min.

According to Fig. 5.2(b), the film surface roughness S_a, which is the arithmetic average of the 3D roughness, in different spray conditions was around 0.17 μm. Except for the case of high suspension flow rate (8 ml/min) with unstable atomisation, higher atomizing pressures reduced droplet diameter, and helped to form more uniform films.

Figs. 5.4 and 5.5 show confocal micrographs of two typical examples of PFA films at various positions, labelled 1 to 4 as indicated in Fig. 5.3, sprayed under near-optimum conditions of flow rate F=5 ml/min, and pressure P=400 kPa and far from optimum conditions of F=8 ml/min, P=140 kPa respectively.

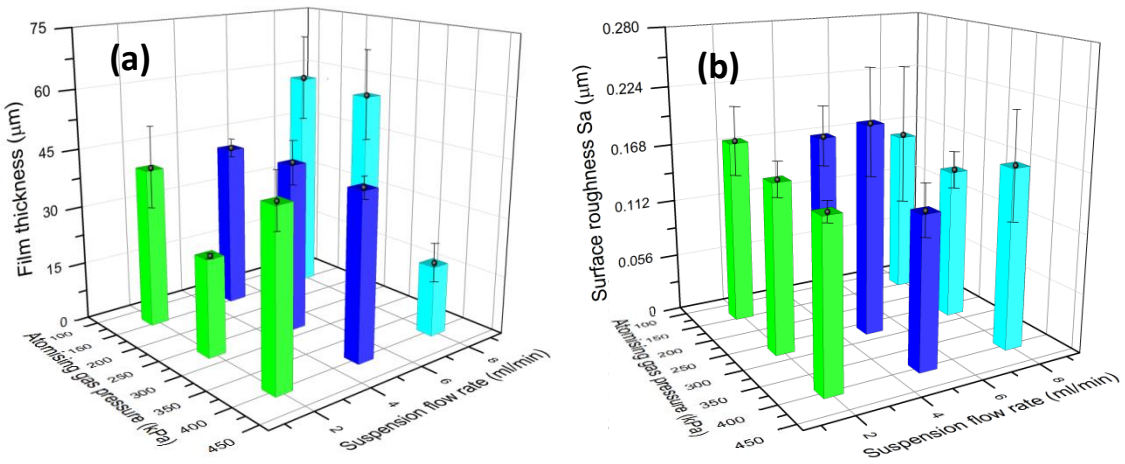

FIG. 5.2. The effect of atomizing gas pressure (kPa) and suspension flow rate (ml/min) on the PFA film (a) thickness and (b) surface roughness after curing.

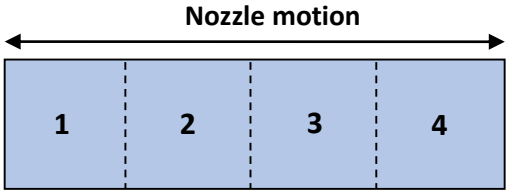

FIG. 5.3. A schematic to show positions of 1 to 4 on the glass slide.

***F*=5 ml/min, *P*=400 kPa**	
Uncured	**Cured**
Position 1, Sa=12.242 μm 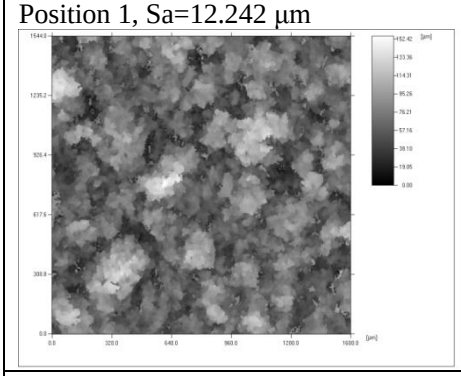	Position 1, Sa=0.117 μm, Thickness=41.52 μm 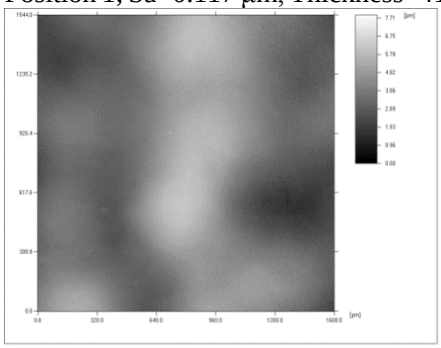
Position 2, Sa=12.710 μm 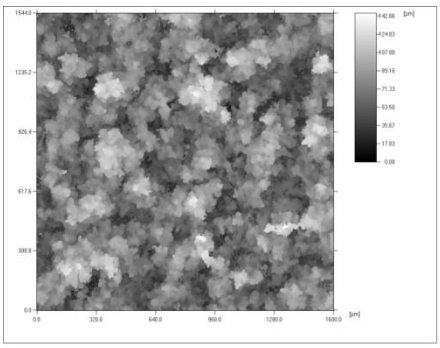	Position 2, Sa=0.175 μm, Thickness=38.80 μm 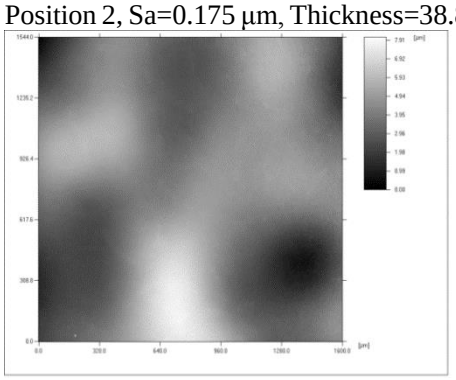
Position 3, Sa=13.797 μm 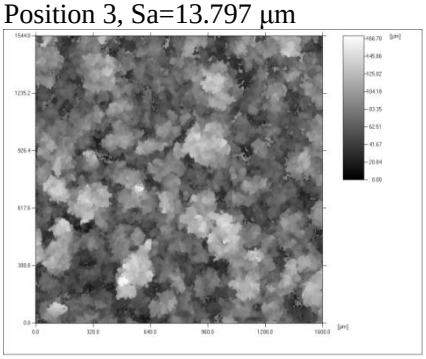	Position 3, Sa=0.141 μm, Thickness=45.10 μm 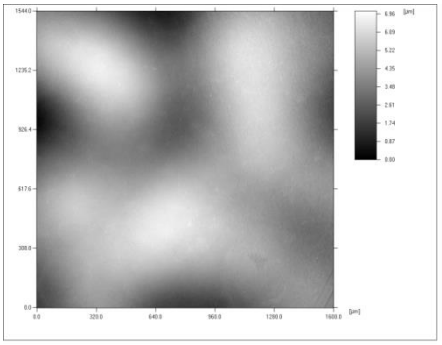
Position 4, Sa=14.398 μm 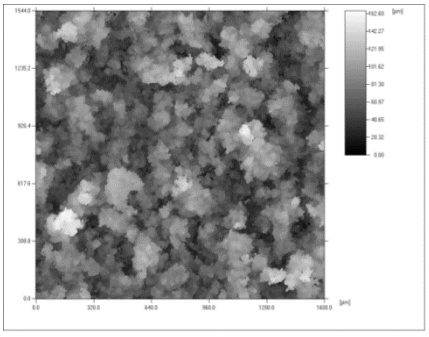	Position 4, Sa=0.140 μm, Thickness=43.20 μm 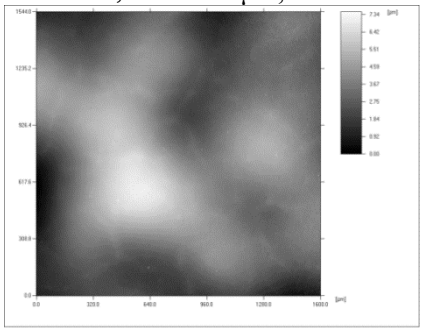

FIG. 5.4. A series of confocal micrographs across a sprayed PFA film before and after curing, manufactured at *F*=5 ml/min, *P*=400 kPa.

***F*=8 ml/min, *P*=1.4 bar**	
Uncured	**Cured**
Position 1, Sa=14.742 µm 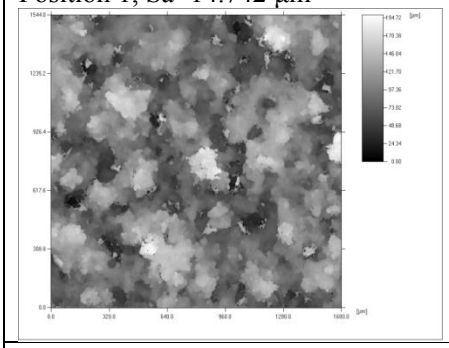	Position 1, Sa=0.267 µm, Thickness=50.1-135 µm 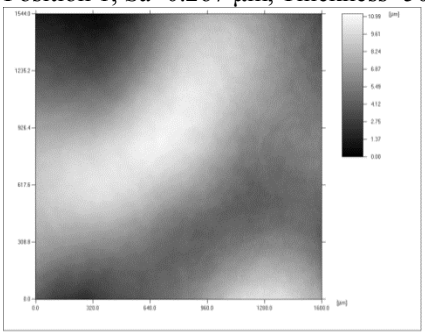
Position 2, Sa=18.615 µm 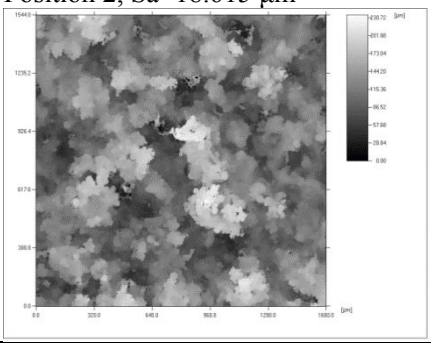	Position 2, Sa=0.124 µm, Thickness=48.7-91.6 µm 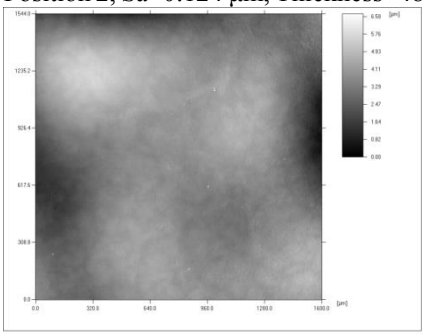
Position 3, Sa=16.601 µm 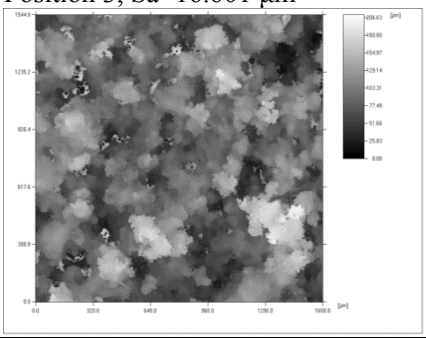	Position 3, Sa=0.130 µm, Thickness=58.5-88.0 µm 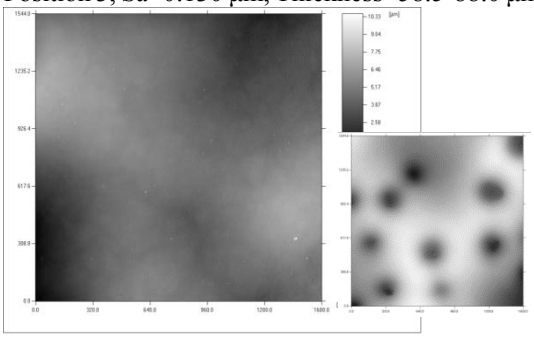
Position 4, Sa=12.092 µm 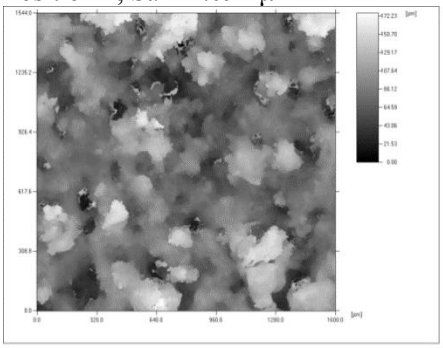	Position 4, Sa=0.122 µm, Thickness=73.6-83.6 µm 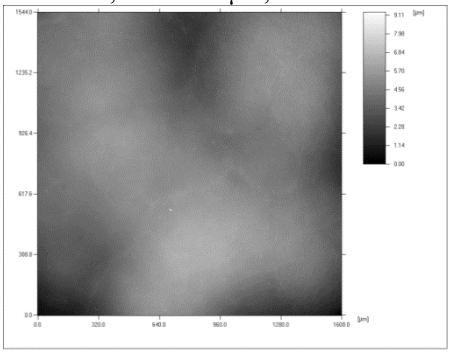

FIG. 5.5. A series of confocal micrographs across a sprayed PFA film before and after curing, manufactured at *F*=8 ml/min, *P*=140 kPa. The inset in position 3 of the cured film shows the presence of bubbles in thick areas.

The above experiments were carried out at a nozzle position vertical height of 17.5 cm above the glass substrate. Experiments were then also conducted at a lower height of 9.5 cm, but in this case, the resulting films were particularly uneven due to excessive liquid blowing over the surface before drying was complete, as shown in Fig. 5.6. The films had poor quality with cracking, flaking and non-uniform thickness. Increasing the atomizing pressure and substrate temperature did not solve this "flooding" that develops because the spray area is too small, and the liquid of the spray confined to a relatively small area i.e. the rate of water arrival per unit area exceeded the rate at which it could be evaporated.

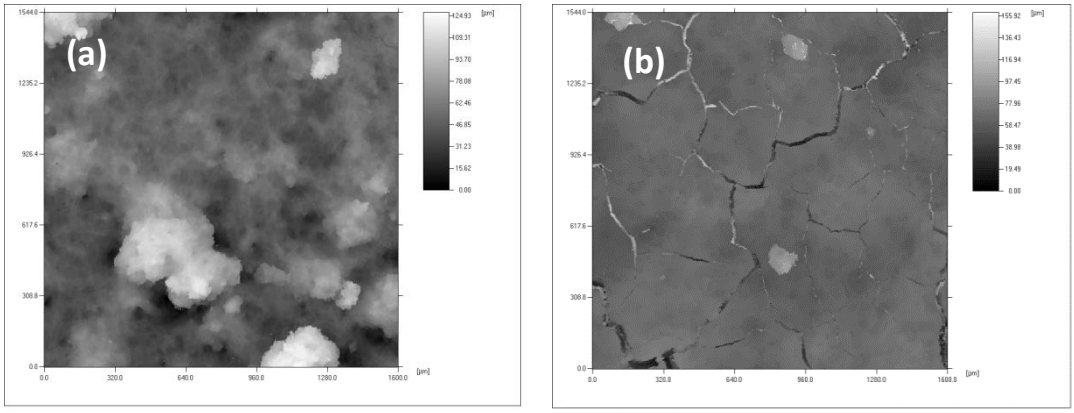

FIG. 5.6. Confocal micrographs across a sprayed PFA film (a) before and (b) after curing, manufactured at F=8 ml/min, P=140 kPa.

5.1.3.2 PFA/MWCNT/PFA Multi-layer Nanocomposite Films

Scanning electron microscopy (840F SEM, JEOL) images of the multiwall carbon nanotubes (MWCNTs) and the cured PFA/MWCNT/PFA nanocomposite film cross-section were taken to visualise the MWCNT morphology and their distribution in the PFA matrix, as shown in Figs. 5.7(a) and (b) respectively. Along with many such cross-sections, there were no obvious MWCNT bundles and MWCNTs were judged well-dispersed in the PFA "sandwich". The thickness of the as-sprayed MWCNT layer was intended to be 500 nm before curing, suggesting MWCNTs wetted within the PFA matrix and some movement of MWCNTs occurred during the curing process as the PFA melted and particles flowed together. Although fluoropolymers might present difficulties in dispersing CNTs due to their low surface tension,[4] the use of anionic surfactant SDBS in preparation of the aqueous solution of MWCNTs was suggested to be efficient in promoting wetting and eliminating large-scale agglomeration of MWCNTs during encapsulation by the PFA matrix. The high shear rates imparted during the atomisation step and at deposition may also have been beneficial in helping to break-up any MWCNT agglomerates persisting after the ultrasonication preparation.

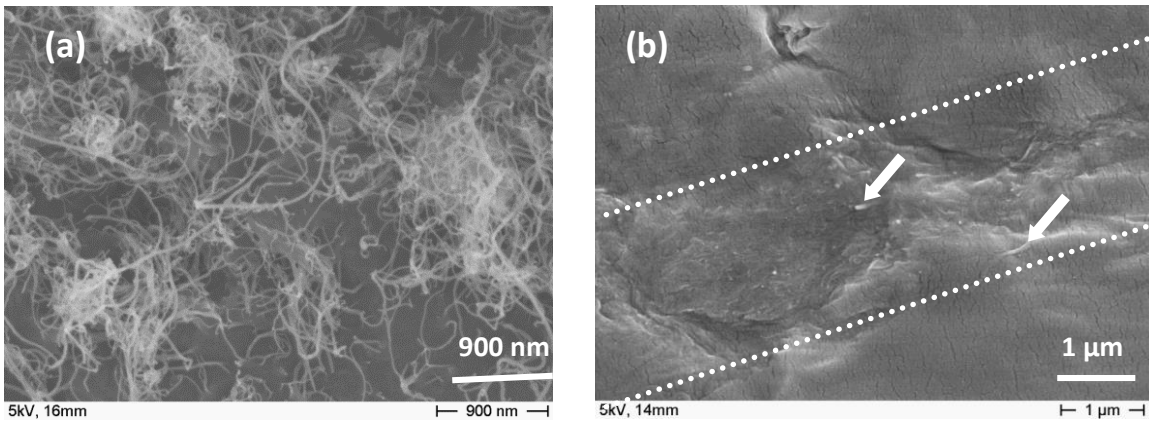

FIG. 5.7. SEM images of (a) as received MWCNTs and (b) the cross-section of cured PFA/MWCNT/PFA multi-layer nanocomposite film. Arrows indicate MWCNTs. Dashed lines indicate the approximate position of the interface between the MWCNTs and the encapsulating PFA layers.

To measure the electrical properties of the nanocomposite film, 90 nm of gold was thermally evaporated onto both sides of the film, as shown in Fig. 5.8. The film permittivity was investigated by an impedance analyzer (Solartron SI 1260) in the frequency range 100 Hz to 1 MHz at room temperature. The real and imaginary permittivities of the PFA/MWCNT/PFA and PFA films as a function of frequency at temperature 25°C are shown in Fig. 5.9(a) and (b), respectively. The real permittivity of PFA films (that relate to the stored energy) was nearly independent of frequency over the measured range at 2.1, which was consistent with the manufacturer's data. The permittivity of the PFA/MWCNT/PFA multi-layered nanocomposite increased significantly at low frequencies, which was ascribed to charge accumulation at the interfaces between the MWCNTs and the matrix, known as interfacial polarization.[5] At high frequencies, the permittivity decreased because the rate of charge accumulation and reorientation cannot keep up with the rapid change of applied field. The imaginary permittivity that related to the dissipation of energy within the medium

was extremely high at lower frequencies. This is because at low frequency, the charges have sufficient time to accumulate at the interfaces and tend to orientate fully along the applied field direction which enhanced the charge movements and hence increased the energy dissipation. Although the dielectric permittivity was high, the dielectric loss was also high below 10 kHz, and the films were highly lossy, effectively acting as an efficient absorber. Such materials are frequently useful in metamaterial based applications, such as an electromagnetic "black hole"[6,7] that can be used to trap and absorb all waves with a major impact in the thermal emission[8] devices. Carbon containing polymer-based coatings are also implicated in various radar absorbing applications.[9]

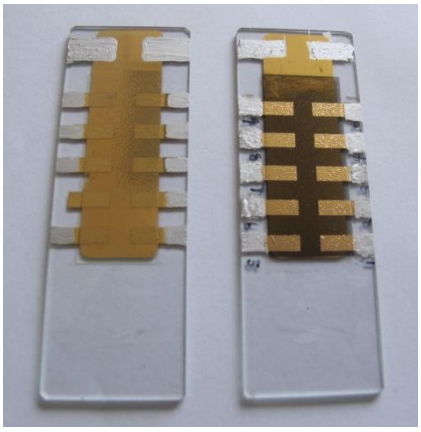

FIG. 5.8. Photographs of PFA and PFA/MWCNT/PFA nanocomposite films coated with gold to form an array of near-identical micro-capacitors for impedance testing.

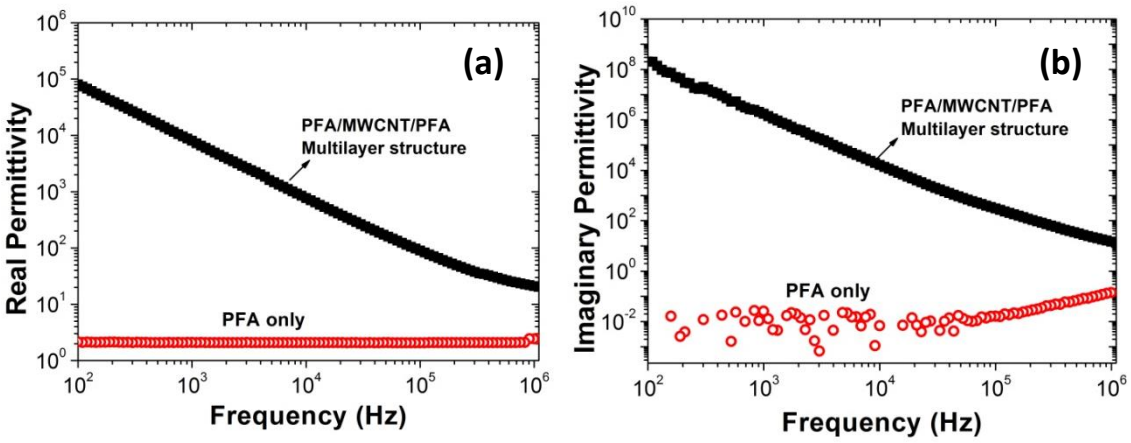

FIG. 5.9. Dependence of (a) the real permittivity and (b) the imaginary permittivity of PFA/MWCNT/ PFA multi-layer films and PFA only polymer films with frequency.

5.1.3.3 PFA/Fe_3O_4/PFA Multi-layer Nanocomposite films

Ferrofluid is commercially supplied colloidal liquid made of nanoscale magnetic particles suspended in water, which becomes strongly magnetized in the presence of a static magnetic field, as shown in Fig. 5.10(a). Dry ferrofluid nanoparticles were characterized by transmission electron microscopy (TEM, JEOL 2000FX). Samples for TEM were prepared by dropping dilute ferrofluid dispersions on an amorphous carbon-coated copper grid and dried under ambient conditions. Fig. 5.10(b) shows a bright field TEM image of the ferrofluid nanoparticles, which were spherical with a narrow diameter distribution of average diameter ~ 10 nm. Fig. 5.10(c) is a selected area electron diffraction (SAED) pattern acquired from the nanoparticle assembly with multiple diffraction rings. The calculated lattice *d*-spacings based on the diffraction rings was consistent with the known lattice spacing for bulk Fe_3O_4 along with their

respective *hkl* indexes from the standard Fe_3O_4 powder diffraction data,[10] as given in Table 5.1.

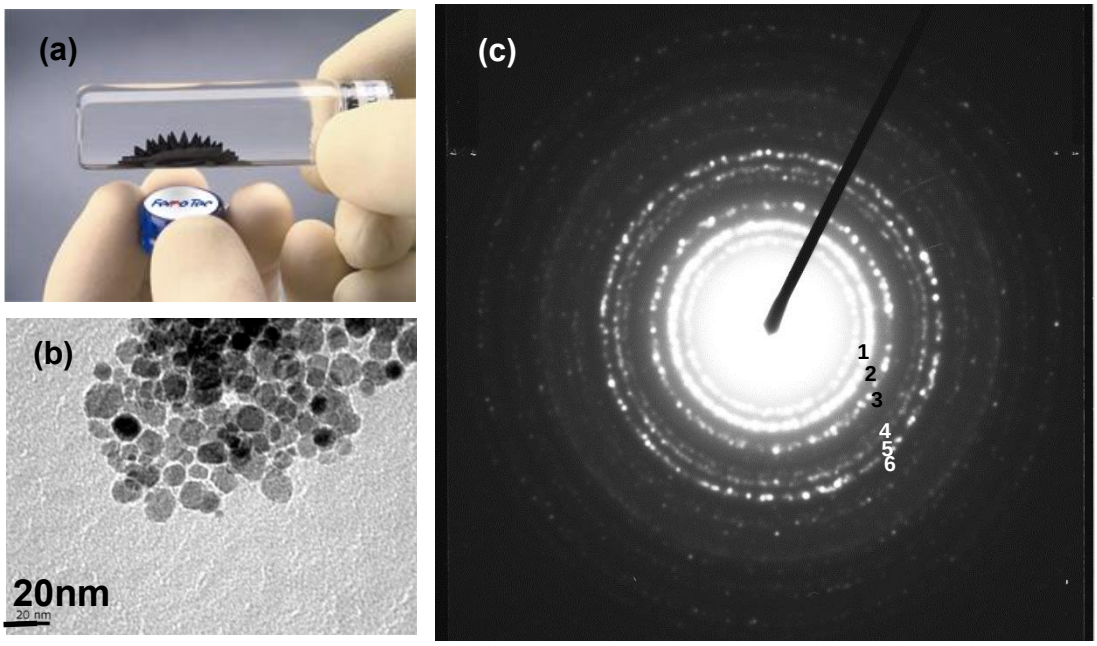

FIG. 5.10. (a) Ferrofluid in a glass tube, with a magnet outside (*FerroTec*). (b) Bright field TEM image of ferrofluid nanoparticles. The average size of the particles was 10 nm. (c) Selected area electron diffraction pattern acquired from ferrofluid nanoparticle assembly.

Table 5.1. Measured lattice spacing, *d* (Å), based on the rings in Fig. 5.10(c) and standard atomic spacing for Fe_3O_4 along with their respective *hkl* indexes from database.[10]

Ring	**1**	**2**	**3**	**4**	**5**	**6**
d	2.97	2.52	2.08	1.73	1.63	1.50
Fe_3O_4	2.97	2.53	2.10	1.71	1.62	1.48
hkl	220	311	400	422	511	440

The phase chemistry of Fe_3O_4 was also confirmed by X-ray diffraction (XRD), as shown in Fig. 5.11. The position and relative intensity of diffraction peaks again matched well with standard Fe_3O_4 powder diffraction data. Although Fe_3O_4 can be oxidized to non-magnetic hematite (Fe_2O_3) at high temperature, XRD patterns of the ferrofluid nanoparticles after 380 °C for 30 min under air atmosphere to mimic the curing process showed little change (Fig. 5.11).

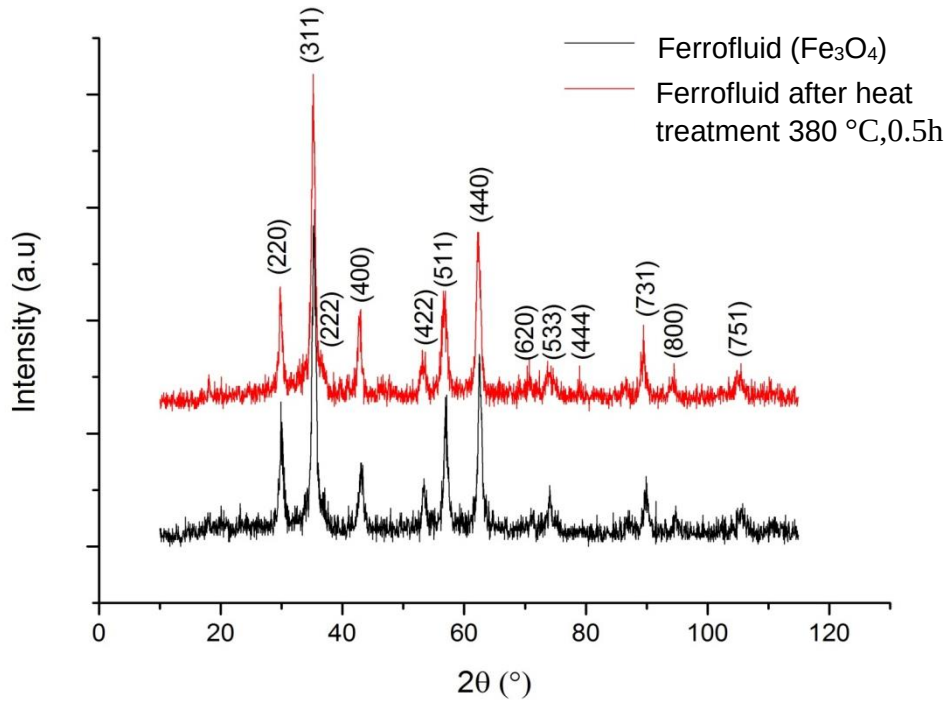

FIG. 5.11. X-ray Diffraction pattern traces of ferrofluid (Fe_3O_4) nanoparticles before and after heat treatment at 380°C for 0.5 hour.

The nanocomposite films could be easily detached by hand from the glass substrates after curing. To demonstrate scalability, large scale PFA/Fe_3O_4 (ferrofluid)/PFA nanocomposite films with size of 13×13 cm were manufactured successfully by the spray deposition technique, as shown in Fig. 5.12.

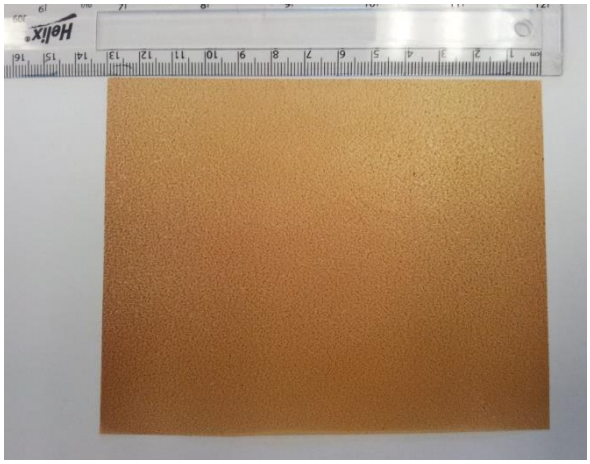

FIG. 5.12. Photographs of 13 × 13 cm PFA/Fe_3O_4(ferrofluid)/PFA nanocomposite films.

Fig. 5.13 shows the magnetization curves of the Fe_3O_4 nanocomposite films measured by vibrating sample magnetometer (VSM, Lakeshore 7400 series), in which the nanoparticles (NPs) were deposited in layers of 110 – 350 nm thickness, between ~ 30 μm thick PFA layers. The thicker the nanoparticle layer, the stronger the magnetic response of the composite film.

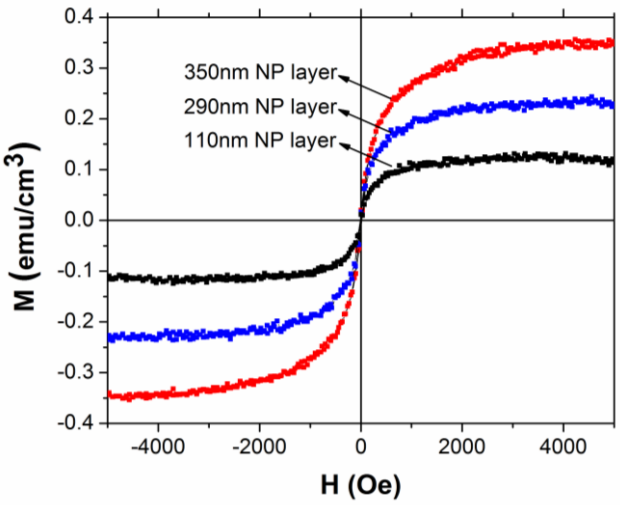

FIG. 5.13. Magnetization curves for PFA/Fe_3O_4 (ferrofluid)/PFA nanocomposite films with various nanoparticle layer thickness.

In the subsequent section, a technique to investigate the magnetic response of these films at high frequency is described, and applying this technique subsequently showed that while the Fe_3O_4 films have a static magnetic field response, this was effectively dissipated at microwave frequencies. Addition of ferrites as described in the previous chapter instead of Fe_3O_4 was considered and explored initially, but was discontinued because: (i) the larger NiZn ferrites were hard to suspend stably; (ii) effort was judged better spent on anisotropic cast magnetic materials and additive manufacture, as described in later Chapters. Nonetheless, no significant barrier is envisaged for future work to successfully develop a spray deposition route for the manufacture of magnetic, flexible polymer-based films.

5.1.4 Conclusions

The atmospheric spray deposition technique provided the possibility to produce multi-layer nanocomposite films composing controlled thickness of nano-scale conductors, dielectrics and insulators by spray processing of nano-suspensions in a potentially low-cost and flexible way. The potential for larger-scale manufacture was demonstrated and the coating of complex curved surfaces could also be contemplated. The key to the manufacture of robust and reproducible films was to develop stable suspensions of the various materials suitable for spray deposition. A parametric optimisation of PFA spray conditions was carried out and then using optimum conditions, sandwiched PFA/MWCNT/PFA and PFA/Fe_3O_4/PFA nanocomposites were produced. The electromagnetic properties of these nanocomposite films were characterized in static magnetic fields and the low frequency range.

The electromagnetic properties of the nanocomposites are most interesting in the broadband microwave regime. However, measurement of permittivity and permeability of thin films in microwave regime is not particularly well-established and can be problematic, not least because thin films give only very limited perturbation to the microwave signal, which results in a very high noise to signal ratio. The next section therefore describes the development of a film permittivity and permeability measurement technique using a broadband co-axial line approach.

5.2 Thin Film Measurement with a Broadband Co-axial Line Technique

5.2.1 Introduction

Thin films with tailored permittivity and permeability properties are used in microwave communication devices,[11,12] for applications such as electromagnetic interference shielding,[13,14] electromagnetic compatibility,[15] field sensors,[16] and magnetic recording.[17,18] Consequently, convenient techniques for broadband electromagnetic characterization of these films in the microwave domain are required. However, broadband measurements on films above 1 GHz can sometimes be relatively restrictive.[19,20] Resonant cavities whose resonance frequency and quality factor *Q* are changed by introduction of a thin film sample and from which the permittivity or permeability tensor can be derived, are straightforward but are limited to discrete frequencies.[21] Shorted micro-stripline perturbation techniques have been developed for broadband thin film measurement up to a few GHz, but a reference sample that is similar to the sample under study in both size and response is needed for accurate measurements[22 - 25] and significant errors may be introduced.[26]

The co-axial transmission line technique is a convenient approach that provides both permittivity and permeability measurement up to (typically) 18 GHz with no need for a reference sample. It is based on the measurement of the complex reflection and transmission amplitude coefficients of a co-axial line loaded with material that are recorded by a vector network analyser (VNA). From the changes in the co-axial line

reflection and transmission coefficients upon material loading, the relative complex permittivity ($\varepsilon=\varepsilon'+i\varepsilon''$) and permeability ($\mu=\mu'+i\mu''$) can be deduced by solving the very widely applied and validated Nicholson, Ross and Weir (NRW) equations.[27,28]

Measurement of the permeability of a thin film has been demonstrated in the case of one layer of film covering the inner conductor of a co-axial line or the outer surface of a dielectric torus,[29] but significant errors can arise when testing films of relatively small permittivity and permeability, which provide only small changes in the reflected and transmitted signal. Instead, the films can be wound onto the torus, generating many revolutions of winding and many concentric layers, producing a thicker, more representative "bulk" sample.[30] However, the films must be tightly wound with no air gaps but in practice the elimination of air gaps is very difficult so that the deduced permittivity and permeability of the thin film may be underestimated by an unknown amount.

In this section, an equivalent circuit model for gap correction of the co-axial line film measurement technique is developed. This analytical approach is then validated by comparison with experimental results, and by comparing reflection and transmission data to that calculated using a simple finite element based model solved using Comsol Multiphysics RF module software. Finally, the relative impact of the air gap and other parameters on the permittivity and permeability are discussed.

5.2.2 Experimental

A standard APC-7 co-axial line with outer conductor diameter of 7 mm and inner of 3 mm was used to characterise the film samples. The co-axial line was designed and fabricated with a characteristic impedance of 50 Ω and operated in a transverse electromagnetic (TEM) waveguide mode. The co-axial cell was connected to a calibrated VNA (Anritsu MS4644A) that quantified the scattering parameters of the segment of co-axial line filled with the material under test. For demonstration, a polytetrafluoroethylene (PTFE) thin film (536-4006 RS Components Ltd) of 76 μm thickness was wound finger-tight onto an inner ring of 3 mm diameter, with sufficient revolutions to give a final external diameter of 7 mm, which was then inserted snugly into the co-axial cell.

Using the standard approach of NRW based on transmitted and reflected coefficients, Fig. 5.14(a) shows the apparent complex permittivity and permeability of the PTFE film as a function of frequency in the range 500 MHz to 10 GHz. Although there was no observable air gap in the wound film in the cell by eye, as shown in the inset of Fig. 5.14(a), the air fraction f_{air} of the sample was calculated to be around 12 vol. % according to the known length of the film used and the precisely known volume of the co-axial cell ($f_{air} = 1 - \frac{V_{film}}{V_{cell}} = 1 - \frac{l_{film} t_{film} w_{film}}{V_{cell}}$, where V_{film} and V_{cell} are the volume of film and sample cell, respectively; l_{film}, t_{film} and w_{film} are the film length, thickness (76 μm), width (7 mm), respectively). From Fig. 5.14(a), the measured real permittivity of

the PTFE film with no air gap adjustment was 1.78 over the range, compared with a supplier data sheet value of close to 2 over this frequency range.

A 3D model of the experimental co-axial line measurement arrangement was established using Comsol Multiphysics RF Module software. Wound films with thickness 76 μm were established in the model along with the air volume fraction of 12 vol. % obtained by experiment, assumed to be distributed equally between each concentric layer. As in the experiment, transmission and reflection parameters were retrieved from the model as a function of frequency and converted to real permittivity and real permeability using NRW.

The modelling approach required no implantations within the Comsol Multiphysics RF Module, and were essentially "standard" and somewhat basic simulations given the potential complexity offered by the software. As was careful grid structure for the simulated geometry, the only significant tasks were the careful attribution of the different physical properties of the film, air, co-axial components, and to ensure that simulation results were stable and grid independent. Fig. 5.14(b) shows the difference $\Delta\varepsilon$ in the simulated permittivity and the actual permittivity of films, as a function of the actual permittivity of the film: the difference increased significantly as the permittivity of the film increased, with an error of almost 50% for a material with a real permittivity of 20. This shows the necessity for applying a correction for the air content if this convenient thin film measurement technique is to be used, but to the best of the author's knowledge, a suitable approach is not available in the literature.

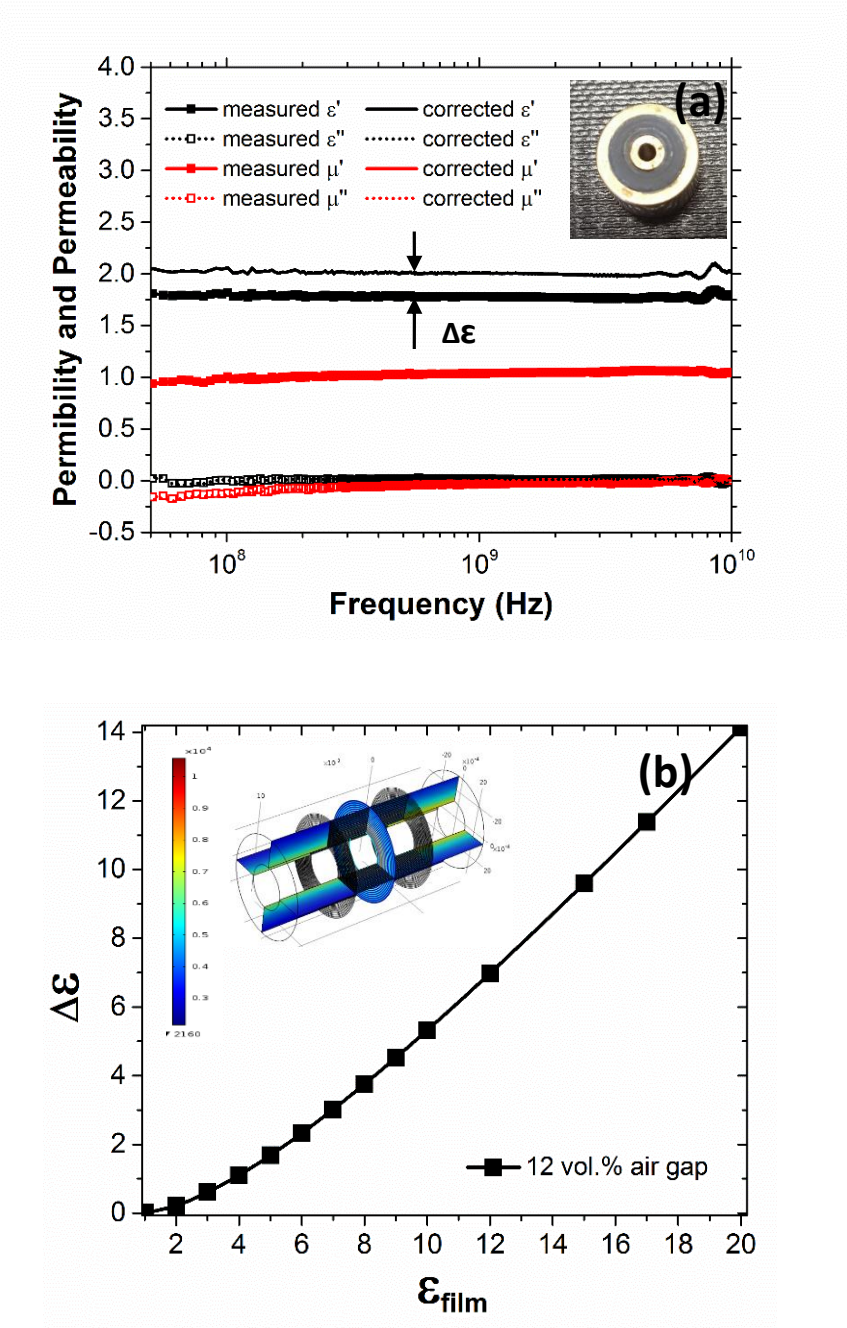

FIG. 5.14(a) Measured frequency dispersions of the complex permittivity and permeability for a 76 μm PTFE film with 12 vol. % air gap. The inset shows the photograph of the wound PTFE sample inside the co-axial cell. (b) Simulation results of the measured permittivity error ($\Delta\varepsilon$) as a function of permittivity in the case a film with a 12 vol% air gap. The inset shows the electric field magnitude of the Comsol Multiphysics model.

5.2.3 Analytical Model

The background to the correction model is based on a layered capacitor model by Baker-Jarvis[31], which is used to mitigate the uncertainties caused by the air gaps when a bulk toroidal or ring sample is measured in a co-axial cell but where they will generally be an air gap between the sample and the inner conductor, and between the sample and outer conductor. This model is now extended to the more complex case of wound thin films where there are air gaps between each winding of the film, which is simplified as a number of concentric rings, each separated by a small air gap of constant thickness, as shown in Fig. 5.15.

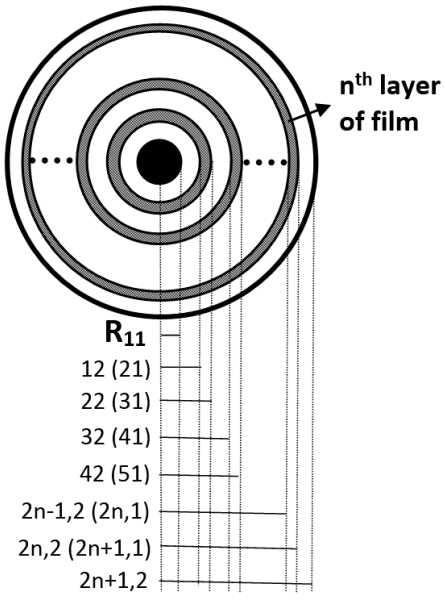

FIG. 5.15. A schematic representation of a wound film with film layers depicted as series of concentric rings, each separated by an air gap of constant thickness. The radius dimension as defined as $R_{n,j}$, where n denotes the sequence number of layer (either air or film), with n=1 is the first inner air layer. j =1 denotes the radius considered from center to the inner boundary of n^{th} layer, and j = 2 is the radius to the outer boundary of n^{th} layer.

With reference to the schematic arrangement in Fig. 5.15 for the calculation of the gap correction for permittivity, the arrangement can be considered as alternating layers of air and material each acting as a capacitor in series.[32,33]

For capacitors connecting in series:

$$\frac{1}{C}=\frac{1}{C_1}+\frac{1}{C_2}+\ldots+\frac{1}{C_n} \tag{5.1}$$

So that,

$$\frac{1}{C_{mea}}=(\frac{1}{C_1}+\frac{1}{C_3}+\ldots+\frac{1}{C_{2n-1}})_{air}+(\frac{1}{C_2}+\frac{1}{C_4}+\ldots+\frac{1}{C_{2n}})_{mat} \tag{5.2}$$

Where C_{2n-1} and C_{2n} (n=1, 2…) are capacitances considering one layer of air and one layer of film respectively and C_{mea} is the measured effective capacitance of the arrangement as a whole.

The capacitance for a cylindrical geometry is

$$C=\frac{2\pi\varepsilon l}{\ln\frac{R_{outer}}{R_{inner}}} \tag{5.3}$$

where R_{inner} and R_{outer} are the radius of inner conducting cylinder and outer conducting cylindrical shell respectively, l is the cylindrical capacitor length, and ε is the dielectric constant of the capacitor medium. Substituting Eq. (5.3) into Eq. (5.2) yields:

$$C_{mea}=\frac{1}{2\pi\varepsilon_{air}l}(\ln\frac{R_{12}}{R_{11}}+\ln\frac{R_{32}}{R_{31}}+\ldots+\ln\frac{R_{2n-1,2}}{R_{2n-1,1}})+\frac{1}{2\pi\varepsilon_{mat}l}(\ln\frac{R_{22}}{R_{21}}+\ln\frac{R_{42}}{R_{41}}+\ldots+\ln\frac{R_{2n,2}}{R_{2n,1}}) \tag{5.4}$$

where ε_{air} and ε_{mat} are the permittivities of air and material respectively. The radius dimension is defined as $R_{n,j}$, where n denotes the layer as either air or film, with n=1 at the inner conductor. j =1 denotes the radius considered from center to the inner boundary of nth layer, and j = 2 is the radius to the outer boundary of n^{th} layer.

Eq. (5.4) can be rearranged to:

$$\varepsilon_{mat} = \frac{B}{(\ln \frac{R_{2n+1,2}}{R_{11}}) / \varepsilon_{mea} - A} \tag{5.5}$$

where $\varepsilon_{mat} = \varepsilon'_{mat} + j\varepsilon''_{mat}$ is the actual material complex relative permittivity with air gap corrected, $\varepsilon_{mea} = \varepsilon'_{mea} + j\varepsilon''_{mea}$ is the measured uncorrected complex relative permittivity that includes the effect of the air gaps, and:

$$A = \sum_{i=1}^{n+1} \ln(1 + \frac{d_{air}}{R_{2i-1,1}}) \tag{5.6a}$$

$$B = \sum_{i=1}^{n} \ln(1 + \frac{d_{mat}}{R_{2i,1}}) \tag{5.6b}$$

R_{11} and $R_{2n+1,2}$ are inner and outer dimensions of the co-axial line, which are 3 mm and 7 mm respectively; d_{air} and d_{mat} are the layer thicknesses of the air layer and film layer respectively.

Similarly, for an air gap correction for the permeability, a series of inductors is considered:

$$L_{mea} = (L_1 + L_2 + \cdots + L_{2n-1})_{air} + (L_2 + L_4 + \cdots + L_{2n})_{mat} \tag{5.7}$$

where L_{2n-1} and L_{2n} (n=1, 2…) are inductances considering one layer of air and one layer of film respectively and L_{mea} is the measured effective inductance of the arrangement as a whole, yielding

$$L = \frac{1}{2\pi} \mu \ln \frac{R_{outer}}{R_{inner}} \tag{5.8}$$

where μ is the permeability of the inductor medium.

Substituting Eq. (5.8) into Eq. (5.7) gives:

$$L_{mea} = \frac{\mu_{air}}{2\pi}(\ln\frac{R_{12}}{R_{11}} + \ln\frac{R_{32}}{R_{31}} + \ldots + \ln\frac{R_{2n-1,2}}{R_{2n-1,1}}) + \frac{\mu_{mat}}{2\pi}(\ln\frac{R_{22}}{R_{21}} + \ln\frac{R_{42}}{R_{41}} + \ldots + \ln\frac{R_{2n,2}}{R_{2n,1}}) \quad (5.9)$$

that can be rearranged to:

$$\mu_{mat} = \frac{(\ln\frac{R_{2n+1,2}}{R_{11}})\mu_{mea} - A}{B} \quad (5.10)$$

where $\mu_{mat} = \mu'_{mat} + j\mu''_{mat}$ is the actual material complex relative permeability with the air gap corrected, $\mu_{mea} = \mu'_{mea} + j\mu''_{mea}$ is the measured uncorrected complex relative permeability that includes the effect of air gaps, and A and B are defined in Eq. (5.6a) and Eq. (5.6b).

5.2.4 Results and Discussion

The validity of the air gap correction approach for thin film measurement was assessed by application to measurements of previously well-characterised PTFE films with ε = 2. As well as the analytical air gap approach based on Eqs. (5.1) to (5.10) above, simulations again using the Comsol Multiphysics RF module were also performed with the air gap geometry explicitly represented.

The 76 μm thick PTFE films were wound onto a core to form a ring with a range of different tensions in order to produce deliberately different air gap contents. Fig. 5.16(a) shows the comparison of experimental air gap corrected and simulated permittivity for

different air gap volume fractions. The measured permittivities were approximately constant over the frequency range from 50 MHz up to 10 GHz, as shown in Fig. 5.14(a) and measured permittivities were lower with higher air fractions. The simulated permittivities were almost exactly coincident with the experimental data. Eq. (5.5) was then applied to the measured permittivites to account for the air gaps and the recovered "actual" or intrinsic permittivities were in excellent agreement with $\varepsilon = 2$ for PTFE at all air fractions below 50%. At 54 vol. % air, the agreement was reduced because the assumption that the air and film layers were uniformly separated becomes increasingly unrealistic as the air gap fraction increases.

Fig. 5.16(b) demonstrates the difference $\Delta\varepsilon$ in the simulated permittivity and the intrinsic permittivity as a function of air gap volume fraction for two films with an assumed permittivity of 2 and 3. Simulations could not be performed for an air fraction lower than 20 vol. % because of a minimum layer thickness restriction of 17.5 μm in the Comsol software. Fig. 5.16(b) shows that $\Delta\varepsilon$ is larger for films with higher intrinsic permittivity.

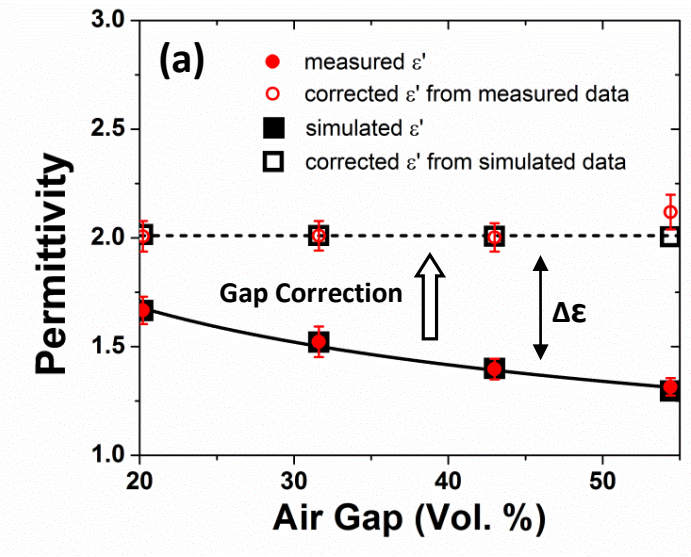

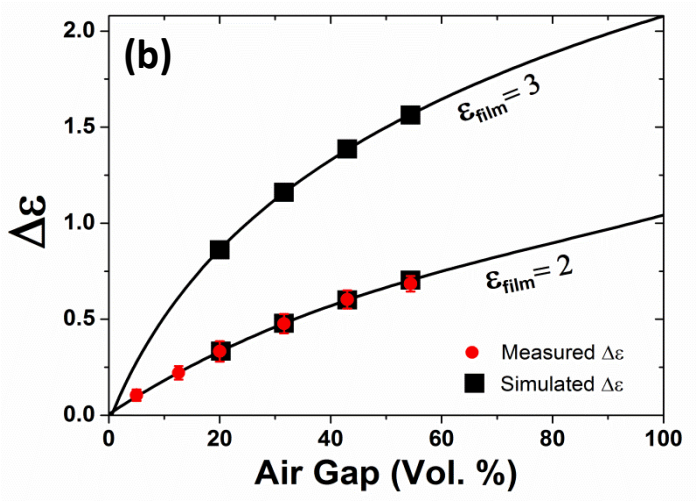

FIG. 5.16. Measured and simulated (a) permittivity of wound PTFE thin films with different air gap volume fractions by experiment and simulation, and permittivity corrected for air gaps using Eq. (5.5); and (b) permittivity adjustment $\Delta\varepsilon$ required for a range of air gap volume fractions for films with intrinsic permittivities of 2 and 3.

Although validation of the air gap correction was straightforward for permittivity, the range of available standard films with known complex permeability and frequency dispersion for validation of the permeability correction approach was very limited. After extensive searching, a 100 μm thick sheet of a dispersion of Fe flake powders in an elastomeric matrix (RS Components Ltd) was selected as the best-available option, and was again wound into a ring on a central axial core and fitted into the co-axial measurement fixture. According to the known film length used and the known volume of the co-axial cell, the air fraction of the wound magnetic film was calculated to be around 35 vol. %. The measured frequency dispersion of permeability for the wound magnetic film sample with 35 vol. % air gap is shown in Fig. 5.17. Then, following a similar procedure to permittivity, the measured data were introduced into Eq. (5.10) to account for the air gaps to obtain a corrected permeability, which is also shown in Fig. 5.17. Because there was no calibrated permeability data available for this film, the corrected permeability was assumed to reflect the intrinsic film permeability, which might be expected to sensibly lie in the range (20 - 30).[34]

Using the corrected permittivity of the film, Comsol simulations were again performed, including the air gap effect, of the co-axial line arrangement and retrieved permeabilities are also shown in Fig. 5.17, falling exactly on the measured complex permeability curves. These data demonstrate that the experimental measurements, their correction for contained gaps using an analytical approach, and the simulations show excellent self-consistency, and when taken with the excellent agreement

provided by the same approach for permittivity, suggest a convenient and robust method for permeability correction.

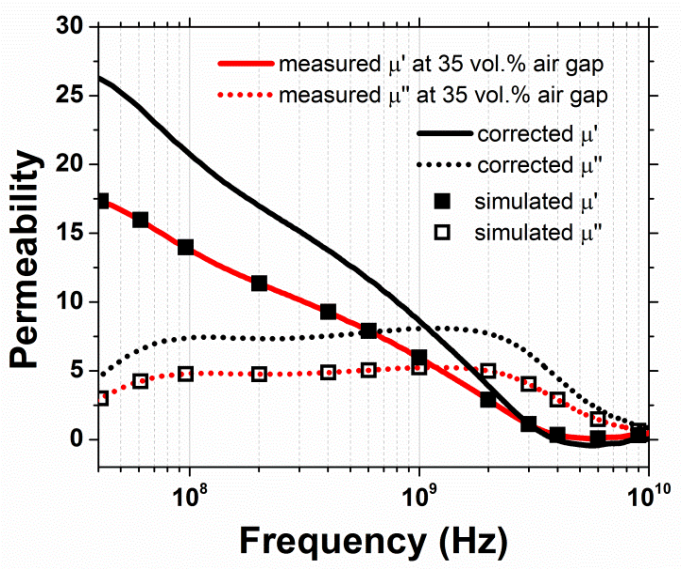

FIG. 5.17. Frequency dispersions of complex permeability for a wound elastomer + Fe particulate composite 100 μm thick magnetic film with a 35 vol. % air gap. The black solid and dotted lines are the corrected permeability from the measured permeability (red line). Corrected permeability was used in simulations that explicitly included the air gap effect, shown as the open/closed black squares.

To investigate the effect of film thickness in this technique, PTFE films with various thicknesses at different air fractions were studied analytically and by simulation, and values of $\Delta\varepsilon$ again obtained, which are shown in Fig. 5.18 for the various cases. Fig. 5.18 also shows a polynomial best-fit of $\Delta\varepsilon$ for a 76 μm thick PTFE, based on the experiments in Fig. 5.16(a). Despite changes in the film thicknesses of 25, 35, 50, 100 and 150 μm, the resulting values of $\Delta\varepsilon$ for a constant air fraction lay closely on the best-fit line through the experimental data, demonstrating that film thickness does not have a significant effect on the measured permittivity. In other words, for the same

film material, regardless of film thickness, the measured permittivity will be the same for the same overall air volume fraction.

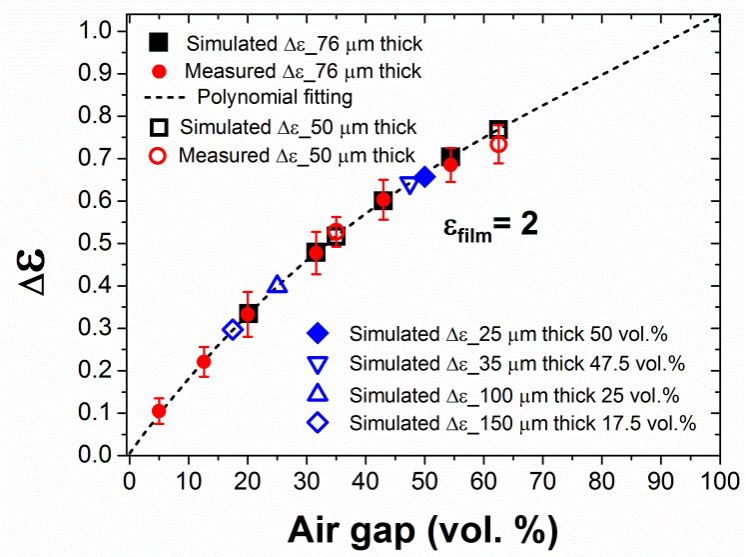

FIG. 5.18. Permittivity correction as a function of air gap volume fractions for PTFE films of various thicknesses, based on experiment, analysis and simulation.

Figs. 5.19(a) and (b) show the "correction factors" for permittivity and permeability as a function of the air gap volume fraction for different values of intrinsic permittivity and permeability. Here the correction factor is the ratio of the corrected value to the measured uncorrected value i.e. $\varepsilon'_c/\varepsilon'_m$ and μ'_c/μ'_m. Figs. 5.19(a) and (b) can be used as "maps" to estimate a film-corrected permittivity and permeability from measured values when the air volume fraction is known. The air gap effect has a more significant effect on permittivity than permeability in the co-axial line arrangement, which is shown in more detail in Fig. 5.20. In the co-axial arrangement, the azimuthal magnetic field is parallel to the plane of the discontinuity of the air gap between concentric windings of the film and therefore the air gap effect is relatively small. In contrast, the

radial electric field is normal across the air gap, resulting in a strong undermining of the measured permittivity and therefore a larger correction factor.

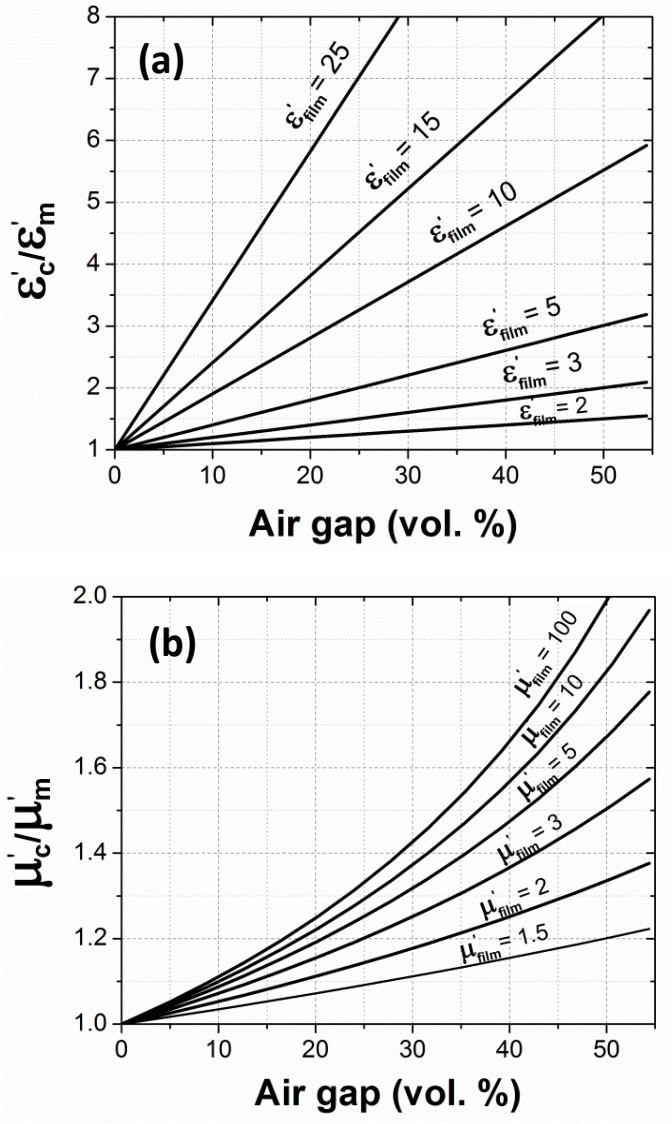

FIG. 5.19. Air gap correction factor for various values of (a) permittivity and (b) permeability.

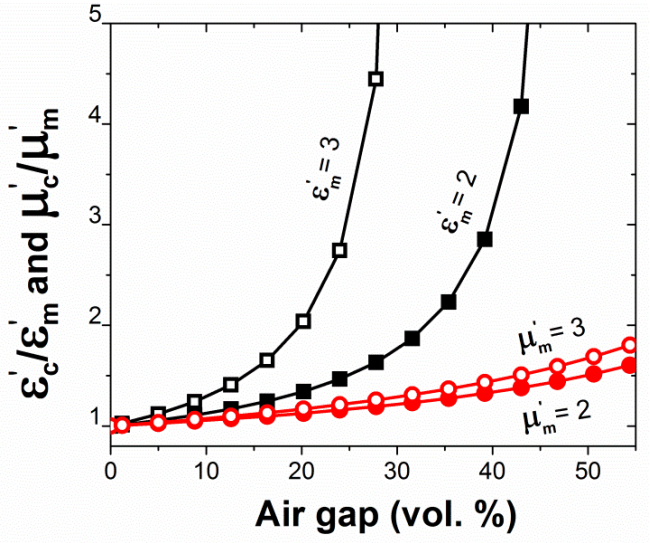

FIG. 5.20. Air gap correction factor for permittivity and permeability as a function of air gap volume fraction.

The air gap correction for thin film permittivity and permeability measurement using a co-axial line method could be further extended, for example to films that are supported on a flexible substrate such as mylar. In this case the three phase system (substrate, coated film, air) could be characterised by a similar extended equivalent circuit approach. Alternatively, for measurements made as a function of temperature, the air gap fraction may change with temperature because of the different thermal properties of air and film, which again could be accounted for readily in the analysis.

5.2.5 Conclusions

A simple broad-band (50 MHz – 18 GHz) permittivity and permeability measurement technique for thin films has been developed based on an analytical air gap correction

approach for wound samples in a co-axial arrangement. The technique has been validated for permittivity for well-characterized PTFE films, and by comparison with finite element simulations in a broad frequency range. The effect of film thickness and air gap volume fraction on the measured permittivity and permeability have been investigated and discussed. This technique may be extended to account for temperature dependent properties of wound films, and for characterization of materials deposited on flexible substrates.

Bibliography

1 X. Zhao, C. Hinchliffe, C. Johnston, P. J. Dobson, and P. S. Grant, Mat. Sci. Eng. B **151**, 140 (2008).

2 X. Zhao, A. A. Koos, B. T. T. Chu, C. Johnston, N. Grobert, and P. S. Grant, Carbon **47**, 561 (2009).

3 E. Leivo, T. Wilenius, T. Kinos, P. Vuoristo, and T. Mäntylä, Prog. Org. Coat. **49**, 69 (2004).

4 X. Chen, C. Burger, D. Fang, I. Sics, X. Wang, W. He, R. H. Somani, K. Yoon, B. S. Hsiao, and B. Chu, Macromolecules **39**, 5427 (2006).

5 R. W. Sillars, Proc. R Soc. London **169**, 66 (1938).

6 R. Alaee, C. Menzel, C. Rockstuhl, and F. Lederer, Opt. Express **20**, 18370 (2012).

[7] Q. Cheng, T. J. Cui, W. X. Jiang, and B. G. Cai, New J. Phys. **12**, 063006 (2010).

[8] X. Liu, T. Tyler, T. Starr, A. F. Starr, N. M. Jokerst, and W. J. Padilla, Phys. Rev. Lett., 045901 (2011).

[9] F. Qin and C. Brosseau, J. Appl. Phys. **111**, 061301 (2012).

[10] R. M. Cornell and U. Schwertmann, *The Iron Oxides: Structure, Properties, Reactions, Occurrences and Uses*. (Wiley-VCH, Weinheim, 1996).

[11] M. J. Lancaster, J. Powell, and A. Porch, Supercond. Sci. Technol. **11**, 1323 (1998).

[12] N. Gupta, A. Verma, S. C. Kashyap, and D. C. Dube, J. Magn. Magn. Mater. **308** (1), 137 (2006).

[13] E. Hakansson, A. Amiet, S. Nahavandi, and A. Kaynak, Eur. Polym. J. **43**, 205 (2007).

[14] S. M. Abbas, M. Chandra, A. Verma, R. Chatterjee, and T. C. Goel, Composites: Part A **37**, 2148 (2006).

[15] S. S. Kim, S. T. Kim, J. M. Ahn, and K. H. Kim, J. Magn. Magn. Mater. **271** (1), 39 (2004).

[16] A. Shalabnety and I. Abdulhalim, Sens. Actuators, A. **159** (1), 24 (2010).

[17] Y. Yang, L. Ma, and J. Wu, MRS Bull. **29** (11), 833 (2011).

[18] D. A. Thompson, L. T. Romankiw, and A. F. Mayadas, IEEE Trans. Magn. **11** (4), 1039 (1975).

[19] C. A. Grimes and J. V. Prodan, J. Appl. Phys. **73**, 6889 (1993).

[20] H. Koyama, H. Tsujimoto, and R. Shirae, IEEE Transl. J. Magn. in Japan **2**, 815 (1987).

[21] R. C. Taber, Rev. Sci. Instrum. **61**, 2200 (1990).

[22] Yan Liu, Linfeng. Chen, C.Y. Tan, H.J. Liu, and C.K. Ong, Rev. Sci. Instrum. **76** (6), 063911 (2005).

[23] V. Bekker, K. Seemann, and H. Leiste, J. Magn. Magn. Mater. **270** (3), 327 (2004).

[24] Jiangjun Jiang, Gang Du, Yun Yao, Cheng Liu, Lin Yuan, Shaowei Bie, Xiucheng Zhang, and Huahui He, J. Magn. Magn. Mater. **320** (5), 750 (2008).

[25] M. Ledieu, F. Schoenstein, J.-H. Le Gallou, O. Valls, S. Queste, F. Duverger, and O. Acher, J. Appl. Phys. **93** (10), 7202 (2003).

[26] S. N. Starostenko, K. N. Rozanov, and A. V. Osipov, J. Appl. Phys. **103**, 07E914 (2008).

[27] A. M. Nicolson and G. F. Ross, IEEE Trans. Instrum. Meas. **19** (4), 377 (1970).

[28] W. B. Weir, Proc. IEEE **62** (1), 33 (1974).

[29] A.-L. Adenot, O. Acher, D. Pain, F. Duverger, M.-J. Malliavin, D. Damiani, and T. Taffary, J. Appl. Phys. **87** (9), 5965 (2000).

[30] O. Acher, J.L. Vermeulen, P.M. Jacquart, J.M. Fontaine, and P. Baclet, J. Magn. Magn. Mater. **136** (3), 269 (1994).

[31] J. Baker-Jarvis, M. D. Janezic, J. H. Jr. Grosvenor, and R. G. Geyer, NIST Tech. Note, National Institute of Standards and Technology, Boulder, CO. **1355** (1993).

[32] W. P. Westpal, Lab. for Insulation Research Tech. Report, MIT (1950).

[33] R. L. Jesch, Nat. Bur. Stand. (U.S.) Tech. Rep. Report NBSIR 78-896 (1978).

[34] F. S. Wen, L. Qiao, H. B. Yi, D. Zhou, and F. S. Li, Chin. Phys. Lett. **25**, 751 (2008).

Chapter 6

Anisotropic Electromagnetic Materials

In this chapter, design and fabrication approaches to realize anisotropic electromagnetic materials with strong and selectable anisotropy in the microwave range are investigated. The benefit of anisotropic magneto-dielectric materials is then demonstrated for an antenna ground plane for low profile applications.

6.1 Design and Fabrication of Anisotropic Magnetic Materials

6.1.1 Introduction

The theory of transformation optics opens up many opportunities and methods to design metamaterials to achieve unprecedented functionality in the control of electromagnetic and acoustic waves according to practical needs.[1,2] The required permittivity ε and permeability μ values in the transformed medium are usually anisotropic and inhomogeneous so that the path of the electromagnetic wave can be

manipulated. The realization of invisibility cloaks,[3,4] hyperlenses,[5] electromagnetic wave concentrators,[6] bending of electromagnetic waves[7-9] and forming of multi-beam antennas[10,11] have been designed and require spatially varying and strongly anisotropic ε and μ with singular values.

Lithography is a common approach to achieve material anisotropy by constructing three dimensional structures with features for example of the size $17.6 \times 17.6\ \mu m^2$,[12] but lithography is rather cumbersome for large-scale production. Self-assembling of anisotropic colloidal nanoparticles has also been reported[13,14], while it has also been demonstrated that anisotropic composites can be realized by aligning flake shape inclusions within a polymer matrix by extrusion[15], tape-casting[16,17], compact molding[18,19] and infiltration[20]. However, the maximum anisotropy difference in properties in orthogonal directions of these materials in terms of permittivity and permeability are limited (e.g. $\varepsilon_{//}'/\varepsilon_{\perp}' \sim 1.7$, $\mu_{//}'/\mu_{\perp}' \sim 1.2$, where $\varepsilon_{//}$, $\varepsilon_{\perp}$, $\mu_{//}$, and $\mu_{\perp}$ are the real permittivities and the real permeabilities parallel and perpendicular to the filler alignment respectively[21]). Therefore, simple and scalable fabrication methods to realize anisotropic electromagnetic materials with strong and possibly manipulable anisotropy in the microwave range are not yet available.

In this chapter, two approaches are explored. In section 6.1.2, anisotropic composites were developed in a preliminary study by aligning anisotropic magnetic inclusions within an epoxy matrix during curing by applying an external magnetic field. The microstructures and electromagnetic properties were then characterized and discussed but only weak anisotropy is induced. Rather than pursuing optimization of this initial

approach, in section 6.1.3, anisotropic material tiles formed from periodic multi-layer stacks of different materials were designed with the help of finite element based simulations using COMSOL Multiphysics software. An analytical model for anisotropy in these type of arrangements was also derived, and was then validated by comparing analytical predictions with both experimental measurements of simple anisotropic cast tiles, and with simulation results. Finally, arrangements of anisotropic cast tiles were explored for use as ground planes in low profile antennas, and preliminary optimization for the most effective arrangement of tiles performed by simulation.

6.1.2 Alignment of Anisotropic Inclusions

6.1.2.1 Experimental

Magnetic composites with two types of anisotropic shape magnetic inclusions were investigated: as-received Ni fibres (Φ30 μm x 0.5 mm, IntraMicron, Inc.) and in-house processed Fe flakes. Fe flakes were prepared by ball milling of spherical Fe powders (<10 μm, Alfa Aesar Ltd. UK) for 4 hours in a high-energy planetary mill (Pulverisette 6, Fritsch GmbH, Germany) at a rotational speed of 300 rpm with a ball-to powder weight ratio of 10:1 in ethanol, and then dried in the same manner as those flakes used in Chapter 4.

Anisotropic magnetic composites were prepared using an epoxy embedding medium (Epon™ 812 substitute) with two different hardeners: 2 dodecenylsuccinic anhydride (DDSA) and methylnadic anhydride (MNA) (Sigma Aldrich Ltd. UK), by a simple

casting route. After extended magnetic stirring of the epoxy mixture, the accelerator 2,4,6-tris(dimethylaminomethyl) phenol (DPM-30) was added, and then the filler powders (either Ni fibres or Fe flakes) were added under stirring followed by 5 min ultrasonication in an ice bath. The composite slurry was then degassed under low vacuum and poured into a silicone mould, with dimensions chosen to match the stripline jig for electromagnetic measurements after minimal machining. During curing of the composite at 60 °C, a magnetic field was applied to orient the anisotropic metallic fillers within the epoxy matrix by proximity of the 10 × 40 × 70 mm silicone mould to two neodymium-based permanent magnets with magnetic field strength ~ 1T, as shown in Fig. 6.1.

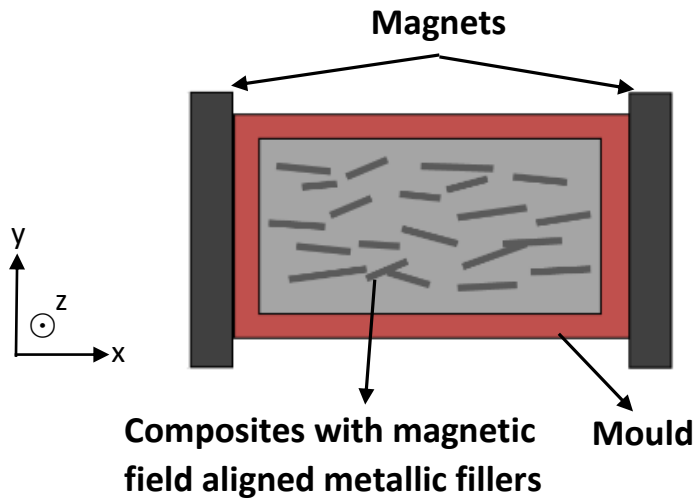

FIG. 6.1. Schematic plan view of aligning magnetic anisotropic inclusions within epoxy matrix by magnets.

Scanning electron microscopy (SEM) images of powders and cross-sections were taken using a JEOL JSM-840F field emission electron microscope and sample cross-sections were prepared by microtome (Ultracut E, Reichert, Inc.). The complex

permittivity and permeability of the composites were measured using a transmission/reflection method, in which a vector network analyser (MS4644A, Anritsu) was used to measure the transmission and reflection coefficients of a stripline containing the material under test. As used previously, the complex permittivity and permeability of the material were then extracted according to the method of Nicolson, Ross and Weir (NRW).[22,23] As shown in Fig. 6.2, in the stripline jig a central flat conducting line is symmetrically bounded by two ground planes and supports a transverse electromagnetic (TEM) waveguide mode. Two identical blocks of the material under test are placed above and below the conducting line. The wave propagates along the conducting signal line (*y*-axis); as a result the stripline measurement on the rectangular sample yields the permeability along the *x*-direction and permittivity along the *z*-direction. For the measurements of anisotropic materials, two pairs of samples with anisotropic inclusions (Ni fibres or Fe flakes) parallel and perpendicularly aligned to the *x*-axis of the composites were prepared for each type of anisotropic inclusions (Fig. 6.2).

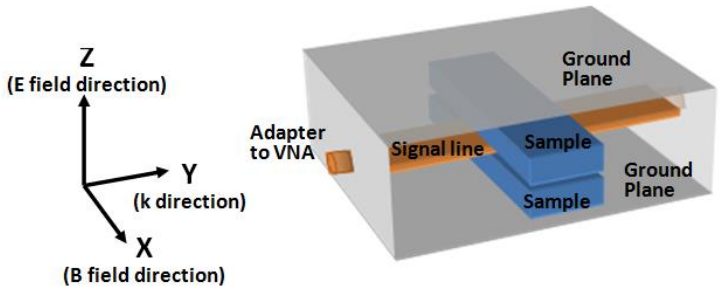

FIG. 6.2. Schematic of the stripline set up containing the sample. The stripline is connected to a vector network analyser (VNA).

6.1.2.2 Results and Discussion

Fig. 6.3(a) shows SEM images of the as-supplied Ni fibres with typical dimensions of Φ30 μm × 0.5 mm. Cross-section images taken in the *x*-*z* plane (see schematic in Fig. 6.2) of the rectangular-shaped 20 vol.% Ni fibre/epoxy composites with fibres partially oriented along *x*-axis and *y*-axis due to the application of the magnetic field are shown in Figs. 6.3(b) and (c), respectively, indicating a marked (but incomplete) fibre alignment and reasonable dispersion.

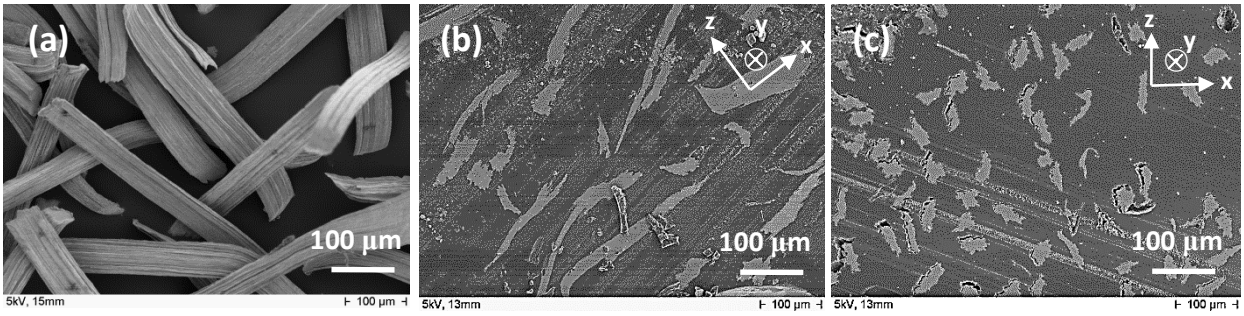

FIG. 6.3. SEM images of (a) as-supplied Ni fibres; *x*-*z* plane cross-sections of 20 vol.% Ni fibre composites with fibre oriented (b) along *x*-axis and (c) along *y*-axis, within the epoxy matrix. The coordinate system is defined in Fig. 6.2.

The frequency responses of the complex permittivity and permeability spectra from 10 MHz to 1 GHz are plotted in Fig. 6.4. The composite permittivity gradually decreased as frequency increased due to the good electrical conductivity of metallic Ni. For the two cases of aligned orientation, their permittivities were almost the same, and lower than that of the random orientation case, which may be explained with reference to Fig. 6.5. In the measurement, the electric field is parallel to the *z*-axis so

that the measured permittivity is in the *z* direction. The fibre alignment was either along the *x*-axis or the *y*-axis (i.e. always in the *x*-*y* plane) so that the aligned samples were equivalent in terms of the electric field experienced in the *z*-direction, resulting in the almost equal permittivities. In the random orientation case, there were more possibilities for fibres aligned and connected in the *z* direction, and this hence led to a larger polarization along the *z*-direction, resulting in the higher permittivity.

Conversely, the magnetic field acts in the *x*-direction so it was supposed that this might result in a distinct difference between permeabilities $\mu_{//}$ (parallel to the fibres) and $\mu_{\perp}$ (perpendicular to the fibres) of the composites, i.e. magnetic anisotropy. However, $\mu_{//}$ and $\mu_{\perp}$ decreased from a weak anisotropy of 1.3 and 1.2 respectively at 10 MHz to be essentially equal at ~1 at 1 GHz.

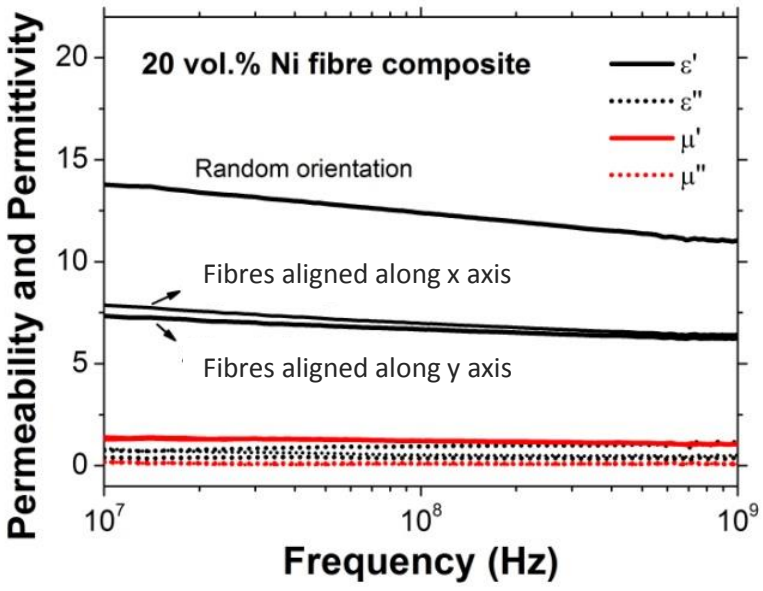

FIG. 6.4. Complex permittivity and permeability of composites with 20 vol.% of Ni fibres in the frequency range of 10 MHz to 1 GHz; comparison between the cases of aligned orientation and random orientation.

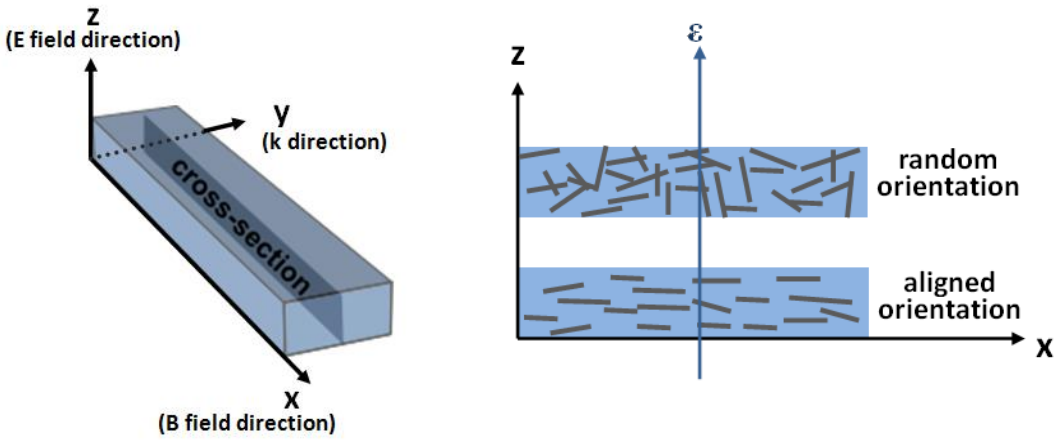

FIG. 6.5. Schematic of the arrangement of samples under the stripline measurement, and *x*-*z* plane cross-sections of Ni fibre composite with fibres in random and aligned orientations.

Given the weak effects provided by the Ni fibres in this frequency range, Fe was then investigated as potentially more effective filler with the objective that Fe particles might offer useful permeabilities in the frequency range of interest. However, no supplier of suitable Fe fibres could be identified, primarily due to the ease of oxidation of Fe fibres. Therefore, Fe flakes of high aspect ratio that might be preferentially aligned in a static magnetic field were prepared in-house by ball milling of Fe particles, and then immediately dispersed and aligned in the epoxy to minimise oxidation.

Fig. 6.6 shows SEM images of Fe particles before and after ball milling. The as-supplied spherical Fe particles with diameters from 1 to 10 μm [see Fig. 6.6(a)] were deformed into flakes with lateral dimensions of a few micrometers and sub-micrometer thickness, as shown in Fig. 6.6(b). Figs. 6.7(a) and (b) show the *x*-*z* plane cross-section images of 35 vol.% Fe flake/epoxy composites with flakes aligned

parallel and perpendicular to the x-axis, respectively, following an identical procedure previously described for Ni fibres.

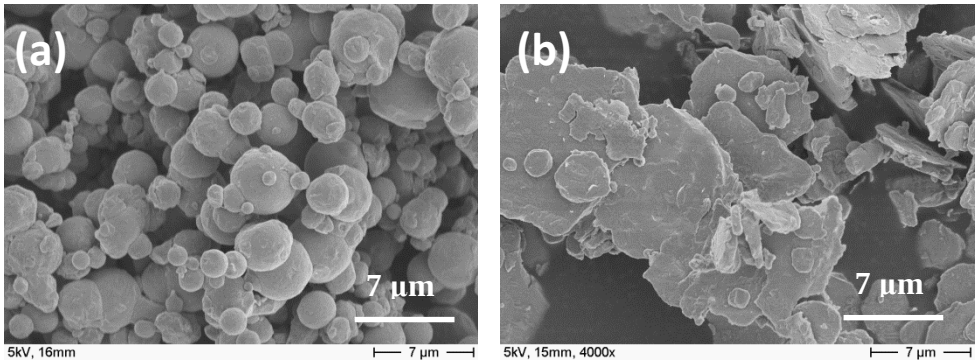

FIG. 6.6. SEM images of (a) as-supplied Fe particles; and (b) Fe flakes after ball milling.

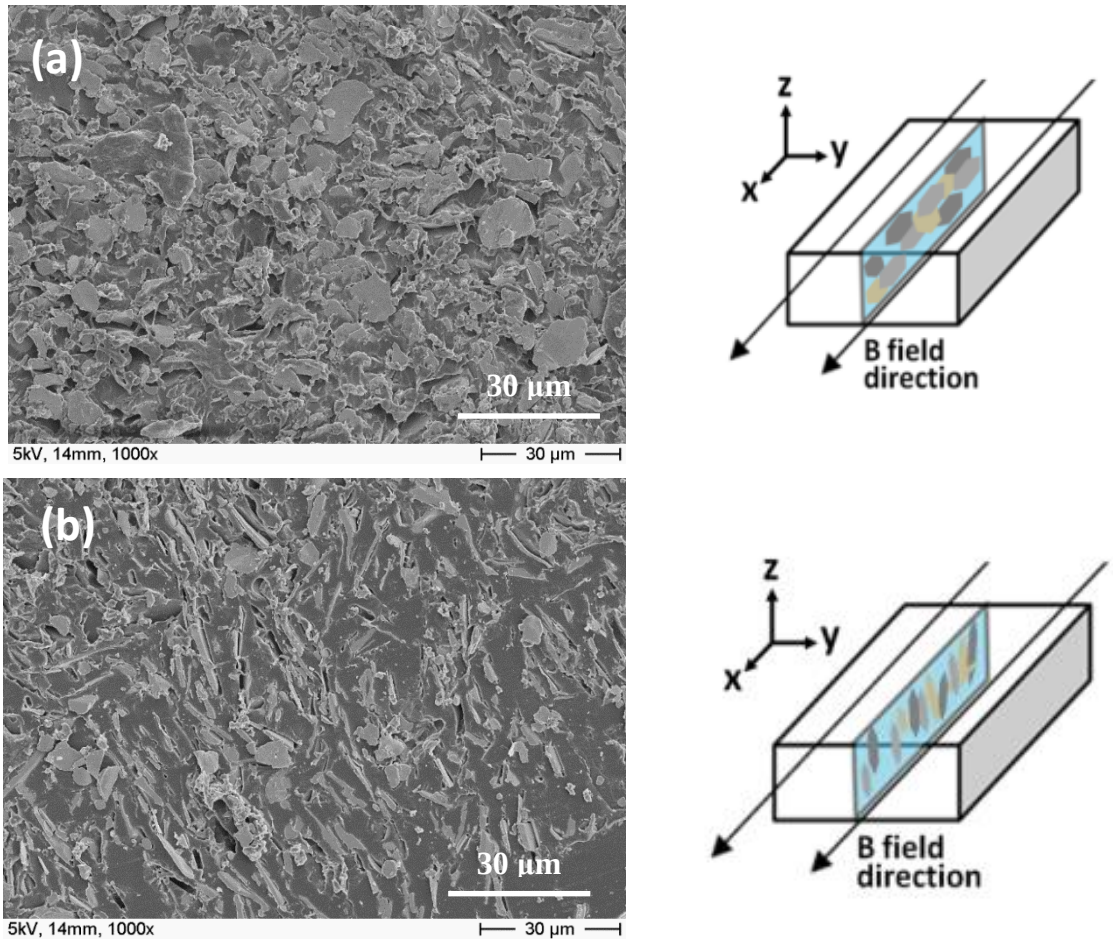

FIG. 6.7. SEM images of *x*-*z* plane cross-sections of 35 vol.% Fe flake composites with flake oriented (a) parallel to *x*-axis and (b) perpendicular to *x*-axis within the cast epoxy matrix. The corresponding schematics are shown on the right. The permeability μ was measured in the *x*-direction.

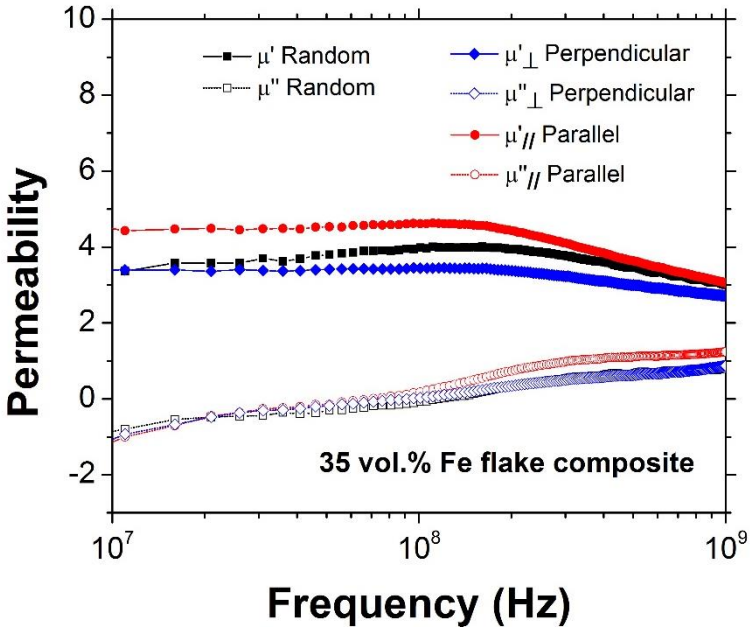

FIG. 6.8. Complex permeability of composites with 35 vol.% Fe flakes in the frequency range 10 MHz to 1 GHz; comparison between the cases of parallel, perpendicular, and no Fe flake alignment (random).

The complex permeabilities of 35 vol.% Fe flake/epoxy composites measured from 10 MHz to 1 GHz with and without Fe flake alignment are shown in Fig. 6.8. The permeabilities were approximately constant to ~ 200 MHz before dropping as the gyromagnetic resonance frequency was approached. The aligned Fe flakes introduced weak magnetic anisotropy in the microwave frequency range: the real permeability $\mu'_{//}$ ~ 4.8 parallel to the flake was higher than the real permeability perpendicular to the flake $\mu'_{\perp}$ ~ 3.6, and the real permeability μ' without any flake alignment lay between these two values. The imaginary permeabilities for these three cases are more or less equal below ~ 200 MHz, and the imaginary permeability $\mu''_{//}$ parallel to the flake became slightly higher than the others when the gyromagnetic resonance frequency

was approached. The slight negative values in the imaginary permittivities at the lowest frequency are due to the measurement instrument working at its lower frequency limit.

Although magnetic anisotropy was introduced, materials with stronger anisotropy and preferably lower loss are generally required for practical devices. As described earlier, when the applied fields are static or have spatial variation on a scale significantly larger than the scale of any local inhomogeneities, heterogeneous materials can behave (as far as incident waves are concerned) as being equivalent to a homogeneous medium. Therefore, as an alternative to intimately mixed materials on the micro-scale, structuring of materials at a coarser scale was explored with the intent of achieving stronger magnetic anisotropy.

6.1.3 Design of Anisotropic Structures

6.1.3.1 Structure Design

A metamaterial is typically composed of common dielectric and magnetic materials with simple periodic structures, but an often over-looked aspect is the need for a scalable fabrication route to realise the practical benefits offered by the material. The structure considered in this study was firstly a periodic array of rectangular channels (filled with air) embedded in a magnetic background material, possessing a complex magnetic permeability μ. A 3D model was created in Comsol Multiphysics software where slabs of 30 × 30 × 4.8 mm of material with arrays of air holes embedded in magnetic matrix whose permeability was assumed to be 6, 50, and 100 respectively.

The simulations themselves followed entirely standard approaches within the Comsol Mutltiphysics software, with the only bespoke aspect of the simulation were the use of different materials in the particular geometry of interest. The structure of this material is illustrated in Fig. 6.9(a), where *a* and *b* denote the dimensions of the rectangular channels in the *z*-direction of a rectangular slab. In the computational domain, two ports (input power 1 W) that were used to generate and receive signals were positioned on the sides of the measured slab. The permeabilities of the composites were then extracted from the simulated transmission and reflection coefficients according to the NRW method previously referenced several times. A systematic simulation study was then performed at an assumed frequency of 30 MHz to identify what types of easily fabricated structures (b/a ratio) and slab materials (μ) might exhibit the greatest magnetic anisotropy, and the results are presented in Table 6.1, where $\mu_{//}$ and $\mu_{\perp}$ represent the simulated effective permeabilities of the composite slab in the direction parallel to and perpendicular to the holes. Fig. 6.9(b) shows the distribution in the electric field magnitude from the Comsol Multiphysics model for one particular set of *b*/*a* ratio and μ assumptions, indicating that the field was weak in the air hole channels that inhibit the wave propagation.

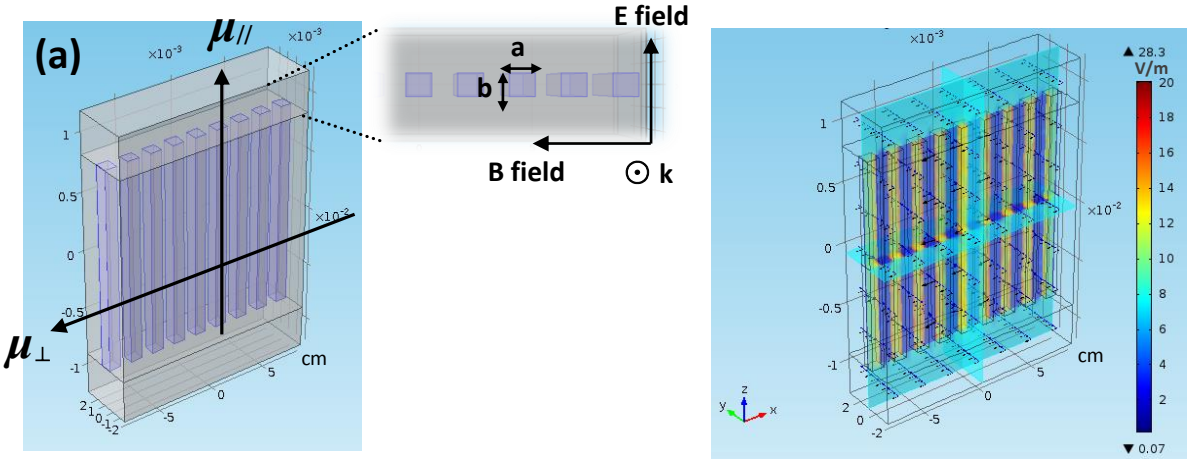

FIG. 6.9 (a) Slabs of 30 × 30 × 4.8 mm with arrays of air holes embedded in magnetic matrix whose permeability was assigned as 6, 50, and 100. The cross-section dimensions of the holes are denoted as *a* and *b*, with length *a* perpendicular to the *E* field, *b* perpendicular to the *B* field, and the wave propogation direction k is perpendicular to *E* and *B* which points out of the paper. (b) The simulated electric field magnitude plot from the Comsol Mutiphysics model, under one particular set of *b*/*a* ratio and μ assumptions.

Table 6.1. The magnetic anisotropy for structures with various matrix permeabilies and hole dimensions, as calculated using Comsol Multiphysics at a frequency of 30 MHz.

Matrix material	Hole size *b*/*a*	$\mu_{//}$	$\mu_{\perp}$	Anisotropy ratio $\mu_{//}/\mu_{\perp}$
μ = 6	1	5.6	5.4	1.0
μ = 50	1	45.9	43.3	1.1
μ = 100	1	89.2	81.6	1.1
μ = 100	2	78.4	61.3	1.3
μ = 100	4	56.8	20.9	2.7

The strength of magnetic anisotropy was defined as the ratio of the magnetic permeability in the direction parallel to the holes to that perpendicular to the holes, as demonstrated in the last column of Table 6.1. As should be expected, Table 6.1 shows that slabs comprising a matrix material with the highest permeability and the hole cross-sections with the largest aspect ratio resulted in the highest effective magnetic

anisotropy. Anisotropy was maximised when the hole length was perpendicular to the *B* field to impede the propagation of *B* field, with the extreme case comprising a multi-layer structure of alternating magnetic material and air. Considering the difficulty of manufacturing a robust, free standing multi-layer structural material with high fraction voids (air), a non-magnetic ($\mu \sim 1$) solid material instead of air was investigated. In order to guide the development of this magnetically anisotropic multi-layer slab material, an analytical model was developed, which could be compared both with the more complex Comsol Multiphysics simulations, and with experimental measurements of simple multi-layer multi-material slabs.

6.1.3.2 Analytical Model

The geometry of a multilayer 1-D periodic structure stacked along the *y* direction is depicted in Fig. 6.10. Each layer with thickness d_i is assumed to be made of material with permittivity ε_i and permeability μ_i, where the subscript *i* represents the i^{th} type of material ($i = 1, 2, \ldots, n$). *m* represents the number of the stacking periods from $i = 1$ to *n*. In order to behave as an effective homogenous medium so that the inhomogeneous structure can be replaced conceptually by a continuous material of average or effective properties, the spacing of one period of the layered structure *S* must be small relative to the wavelength of any incident microwave $\lambda_0 \sim S < 0.3\lambda_0$.[24]

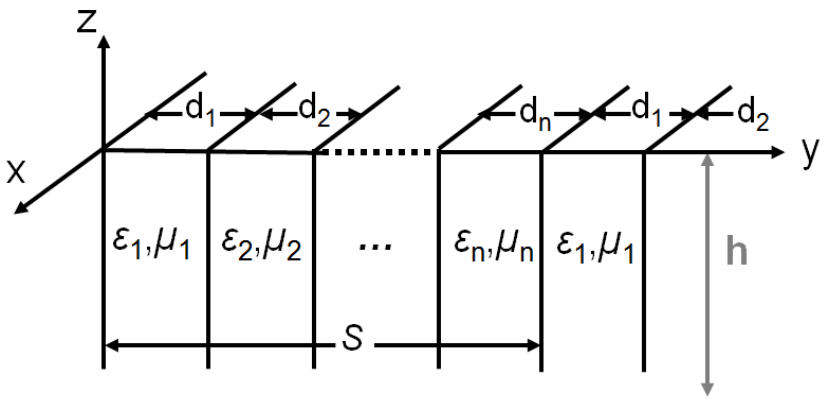

FIG. 6.10. A schematic representation of a periodic, multi-layered material.

Because of the similar orientation of the layers with respect to the *x* and *z* axis, it can be anticipated that the resulting medium has the same effective permittivity and permeability in the *x* and *z* direction, but different effective permittivity and permeability in the *y* direction, and therefore represents a uniaxial anisotropic medium where permittivity ε and permeability μ take the following form:

$$\varepsilon = \begin{bmatrix} \varepsilon_o & 0 & 0 \\ 0 & \varepsilon_e & 0 \\ 0 & 0 & \varepsilon_o \end{bmatrix} \tag{6.1a}$$

$$\mu = \begin{bmatrix} \mu_o & 0 & 0 \\ 0 & \mu_e & 0 \\ 0 & 0 & \mu_o \end{bmatrix} \tag{6.1b}$$

where subscript "*o*" and "*e*" demote the ordinary (non-periodic; non-layered) and extraordinary axes (periodic; layered), respectively.

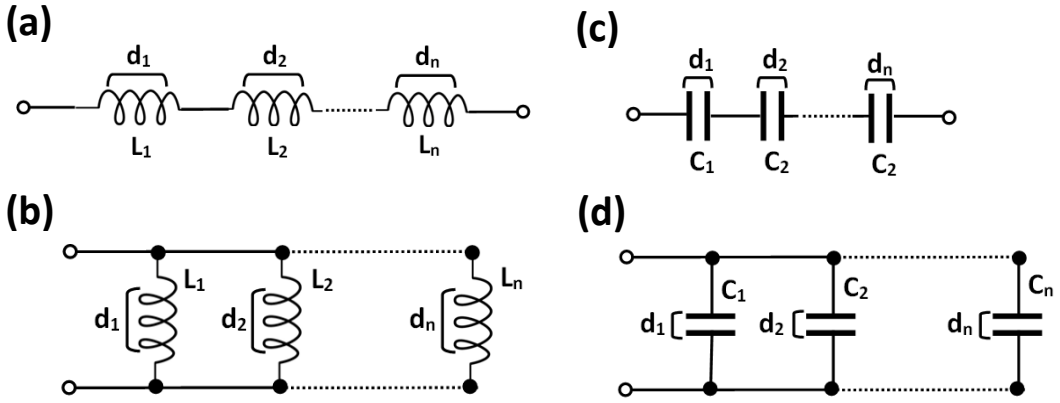

FIG. 6.11. Equivalent electrical circuits for multilayer structured material (a and b) inductors representing the permeability and (c and d) capacitors representing the permittivity

Similar to the derivation of gap correction model for thin film measurement in Chapter 5, the effective ordinary and extraordinary permittivities and permeabilities of the slab can also be evaluated analytically. In this case, it is a multi-layered structure rather than the concentric rings depicted in the coaxial line thin film measurement.

With reference to the schematic arrangement in Fig. 6.10, for the magnetic induction lines in the plane of the slabs, the effective relative permeability along the ordinary axis μ_o can be derived by considering each slab acting as an inductor in series (Fig. 6.11(a)), so that the effective inductance L_0 can be expressed as:

$$L_o = \sum_{m=1}^{m} (L_1 + L_2 + ... + L_n)_m \tag{6.2}$$

where L_i (i=1, 2,..n) are inductances of each slab-shaped layer of material.

The inductance of the magnetic flux Φ penetrating the circuit divided by the current I flowing in the circuit is given:

$$L = \frac{\Phi}{I} \tag{6.3a}$$

where $\Phi = \int \vec{B} \cdot d\vec{S}$; and B is magnetic flux density $B = \mu H$ (6.3b)

Ampere's law gives: $\int H \cdot d\vec{l} = I \Rightarrow H = \frac{I}{h}$; (6.3c)

where H is the magnetic field strength; h is the slab height defined in Fig. 6.10.

which yields $\Phi = \frac{\mu I}{h} d$ (6.3d)

so, $L = \frac{\mu d}{h}$ (6.3e)

Substitution of Eq. (6.3e) into Eq. (6.2) yields:

$$\mu_o = \frac{\mu_1 d_1 + \mu_2 d_2 + ... + \mu_n d_n}{d_1 + d_2 + ... + d_n} \tag{6.4}$$

In contrast to the case that the magnetic induction field is perpendicular to the plane of the slabs, the effective relative permeability along the extraordinary axis μ_e can be derived by considering a parallel of inductors [Fig. 6.11(b)],

$$\frac{1}{L_e} = \sum_{m=1}^{m} (\frac{1}{L_1} + \frac{1}{L_2} + ... + \frac{1}{L_n})_m \tag{6.5}$$

where L_e is the effective inductance of the arrangement as a whole along the extraordinary axis. The extraordinary permeability of the structure is then given by:

$$\mu_e = \frac{d_1 + d_2 + ... + d_n}{\frac{d_1}{\mu_1} + \frac{d_2}{\mu_2} + ... + \frac{d_n}{\mu_n}} \tag{6.6}$$

Similarly, for the alternative case of the electric field vector and the propagation vector

lying in the plane of the slabs, permittivity along the ordinary axis ε_o can be derived by considering a parallel of capacitors (Fig. 6.11(d)):

$$C_o = \sum_{m=1}^{m} (C_1 + C_2 + ... + C_n)_m \tag{6.7}$$

where C_o is the effective capacitance of the arrangement as a whole along the ordinary axis, and C_i (i=1, 2,..n) are capacitances considering one slab of each material. The capacitance of a parallel plate capacitor is:

$$C = \frac{\varepsilon A}{l} \tag{6.8}$$

where A is the area of plate, l is the distance between plates.

Substitution of Eq. (6.8) into Eq. (6.7) yields:

$$\varepsilon_o = \frac{\varepsilon_1 d_1 + \varepsilon_2 d_2 + ... + \varepsilon_n d_n}{d_1 + d_2 + ... + d_n} \tag{6.9}$$

For the electric field vector perpendicular to the plane of the slabs, the permittivity along the extraordinary axis ε_e can be derived by considering capacitor connecting in series:

$$\frac{1}{C_e} = \sum_{m=1}^{m} \left(\frac{1}{C_1} + \frac{1}{C_2} + ... + \frac{1}{C_n}\right)_m \tag{6.10}$$

So that,

$$\varepsilon_e = \frac{d_1 + d_2 + ... + d_n}{\frac{d_1}{\varepsilon_1} + \frac{d_2}{\varepsilon_2} + ... + \frac{d_n}{\varepsilon_n}} \tag{6.11}$$

The equivalent electric circuits for describing Eqs. (6.4), (6.6), (6.9) and (6.11) were shown in Figs 6.11(a-d), respectively. The circuits represent a stack of multi-layered

materials with electromagnetic properties ε_i and μ_i. C_i corresponds to the capacitance of the each material while L_i are their inductances (i=1, 2,…n). It is also interesting to note that this structure allows independent control of the effective permittivity and permeability i.e. ε_o and ε_e are only functions of ε_i, and μ_o and μ_e are only functions of μ_i. This simple multi-layer model can then be applied to the design of an anisotropic electromagnetic system.

6.1.3.3 Results and Discussion

The validity and applicability of the approach described in the previous sections [Eqs. (6.1) to (6.11)] were assessed by comparing predictions to experimental results obtained from measurements of fabricated multi-layer structured materials. In this study, only two types of material were investigated, although in principle more different layers could be used. Simulations again using the Comsol Multiphysics RF module were also applied in which the specific electromagnetic properties of each layer were explicitly represented as discrete, separate materials, based on experimental measurements of each material separately (in a stripline jig).

Slab or "tile" structures comprised commercially available sintered NiZn ferrite bars (FER/PLATE/F16) supplied by MagDev Ltd. (UK) and epoxy resin (Epon^{TM} 812 substitute) from Sigma Aldrich Ltd. (UK), which were manufactured into 30 × 30 × 4.8 mm alternating multilayer structured tiles, as shown in Fig. 6.12. The permittivity and permeability of the epoxy were approximately 3 and 1, respectively. The frequency dispersions of permittivity and permeability for the NiZn ferrite bars were

characterized as shown in Fig. 6.13. The real permittivity of NiZn ferrite was ~ 10.5, which was largely independent of frequency in the measured range 5 MHz to 1GHz. The real permeability of NiZn ferrite was approximately constant at ~ 55 up to 30 MHz before dropping rapidly as the gyromagnetic resonance frequency was approached.

FIG. 6.12. Multilayer tiles comprised of alternating layers of NiZn ferrite bars and epoxy resin with a size of 30×30×4.8 mm.

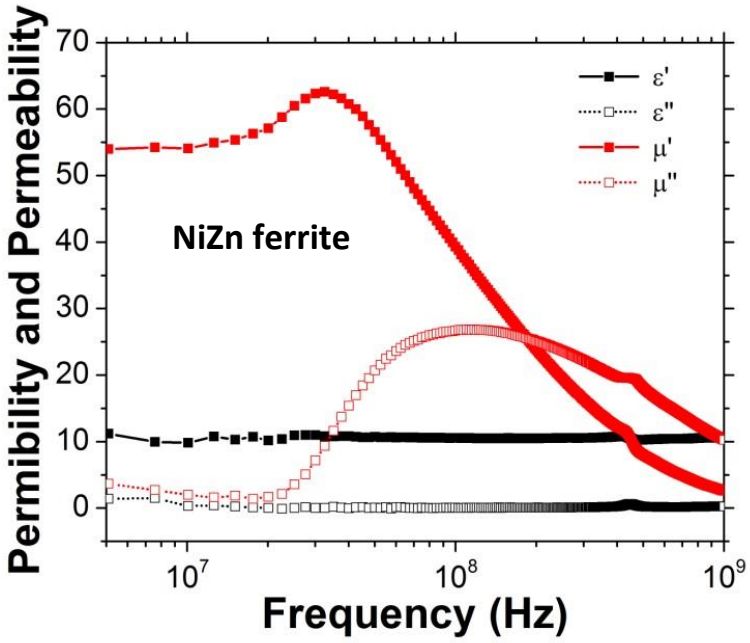

FIG. 6.13. Frequency dispersion of the complex permittivity and permeability of NiZn ferrite bars.

The manufactured tiles were characterized in a calibrated stripline arrangement, and in turn positioned with layers parallel to the magnetic field and perpendicular to the magnetic field so that both permeabilities along the direction parallel and perpendicular to the layers were obtained, as shown in Figs. 6.14(a) and (b) respectively. Strong magnetic anisotropy was obtained with a real permeability along the direction parallel to the layers $\mu_{//} \sim 30$, and perpendicular to the layers $\mu_{\perp} \sim 2$. That $\mu_{//}$ had strong frequency dispersion and reduced rapidly above a cut-off frequency of ~ 30 MHz, while $\mu_{\perp}$ remained almost constant over the measured frequency range, was in accordance with Snoek's law [25] that states that a larger permeability leads to a lower cut off frequency, and vice-versa. Unlike the permeabilities, the measured complex permittivities in Figs. 6.14(a) and (b) for both orientations were similar at approximately 7, and were essentially frequency independent in the measured region. This arose because for both measurement orientations the electric fields were always aligned within the plane of layers, as demonstrated in the insets of Figs. 6.14(a) and (b), resulting in the same permittivity. The dotted lines in Figs. 6.14(a) and (b) were obtained by simulation and the thin solid lines were calculated according to the analytical model. The two were generally coincident and in good agreement with the experimental results. The small differences in experiment, simulation and theory probably arose due to some variability during fabrication, especially the imperfect bonding at the NiZn ferrite/epoxy interface. Tiles with other alternative layer thickness were also experimentally measured and simulated. As expected, all results showed good consistent with the analytical model because the size of tiles is far smaller than the microwave wavelength so that the wave cannot distinguish the difference.

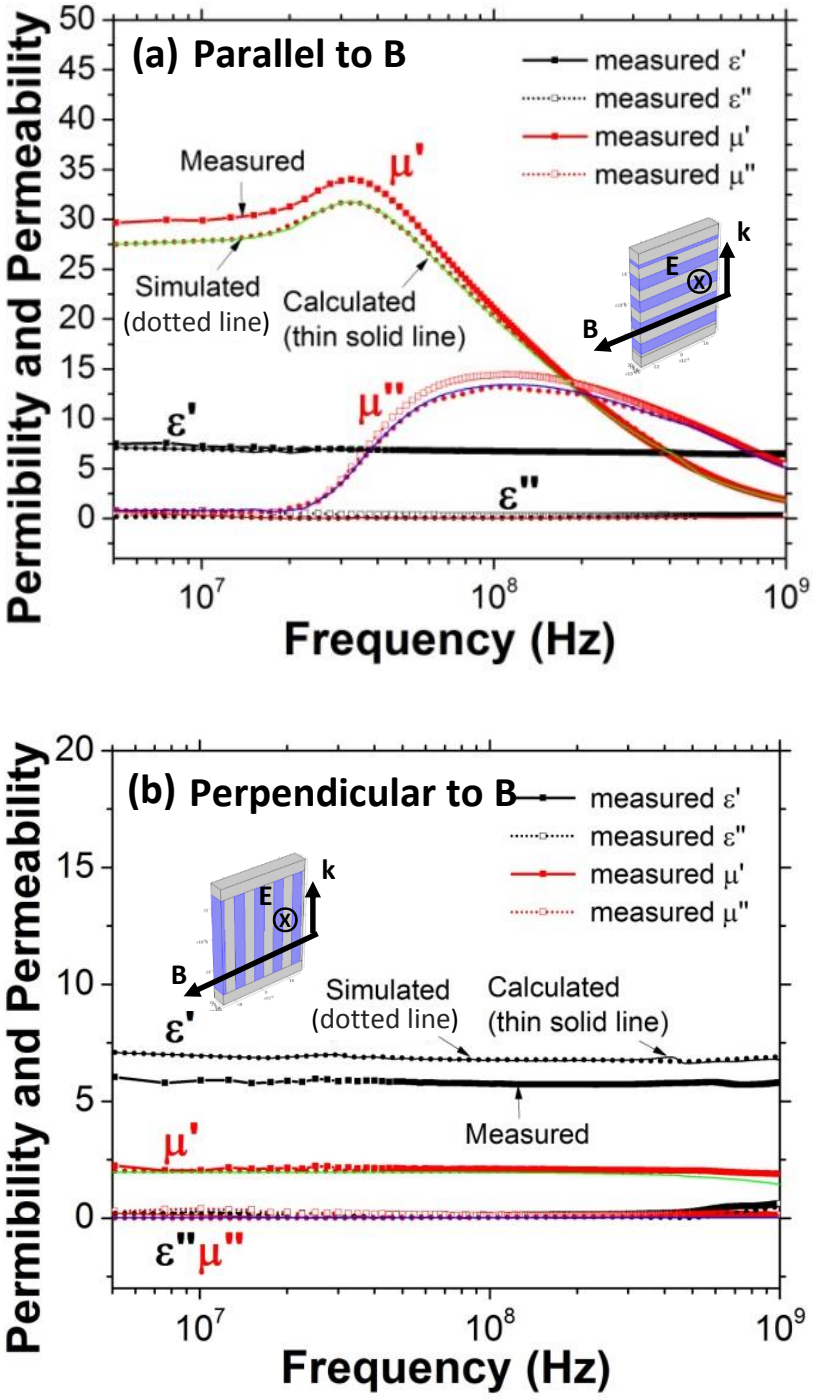

FIG. 6.14. Measured, simulated and calculated frequency dispersion of permittivity and permeability of the ferrite/epoxy multi-layer tiles with (a) magnetic field *B* parallel to the layers and (b) magnetic field *B* perpendicular to the layers. The insets show the schematic arrangement of the sample relative to *E* and *B* field.

For the two alternating layer case, the magnetic anisotropy in Eqs. (6.4) and (6.6) can be simplified to:

$$\frac{\mu_{//}}{\mu_{\perp}} = \frac{(\mu_1 + \mu_2\eta)(\mu_2 + \mu_1\eta)}{(1+\eta)^2 \mu_1\mu_2}, \quad \eta = \frac{d_2}{d_1} \tag{6.12}$$

where $\mu_{//}$ and $\mu_{\perp}$ are the real permeabilities along directions parallel and perpendicular to the layers, respectively; μ_1 and μ_2 are the real permeabilities of each material layer; d_1 and d_2 are the corresponding material layer width; and η is the two periodic layer width ratio.

Fig. 6.15 shows the strength of magnetic anisotropy as a function of η. One of the materials is assumed non-magnetic with μ_1 = 1. The permeability of the second material has a significant effect on the overall magnetic anisotropy. For a given materials combination, the maximum anisotropy is obtained when the two materials are equally spaced, i.e., $d_1 = d_2$, η = 1. Fig. 6.15 can be used as a "map" to locate the materials type and layer width combination for the desired magnetic anisotropic properties in practical applications.

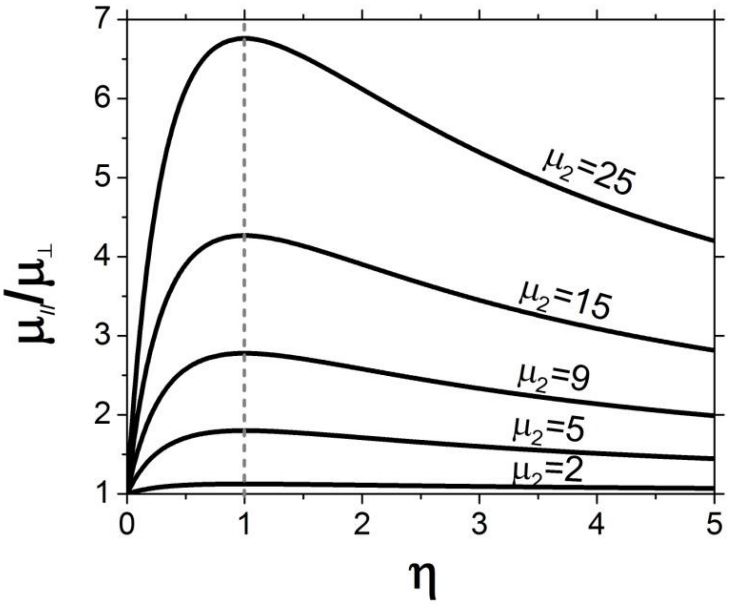

FIG. 6.15. The strength of magnetic anisotropy as a function of the layer width ratio for two types alternating multilayer structures. One type of material is considered non-magnetic. The maximum anisotropy effect is obtained at $\eta = 1$.

6.1.4 Conclusions

Two approaches to realize anisotropic electromagnetic materials were explored by aligning anisotropic magnetic inclusions within a curing polymer matrix using a static magnetic field and by designing multi-layer structures. Composites with aligned anisotropic inclusions achieved only weak electromagnetic anisotropy, but a stronger effect might be achieved in the future using filler materials with high aspect ratio and stronger magnetic response. Multi-layer dielectric and magnetic layer slab structures were simulated, assembled from epoxy and NiZn ferrite bars into tiles and were shown experimentally to give effective, homogeneous but anisotropic properties when the spacing between layers was small compared with the wavelength. An analytical model

was also developed to understand the effective anisotropic properties of the same multi-layer structures, and was validated successfully by comparison with experiment and simulation. Strong magnetic anisotropy was achieved in the multi-layer structure and it was shown to be straightforward to manipulate properties to achieve a wide range of magnetic anisotropy through variations in the layer constituent properties and their relative proportions.

In next section, the utility of these electromagnetically anisotropic materials is investigated in the design of low profile antenna.

6.2 Application of Anisotropic Magneto-Dielectric Materials in Low Profile Antenna

6.2.1 Introduction

The ever-increasing demand for portable electronic devices continues to push the development of multifunctional materials for miniaturizing electronic components, including low profile antenna designs. The dipole antenna is a simple and fundamental radiator in antenna engineering. Traditional implementations of dipole antennas entails using a perfect electric conductor (PEC) ground plane placed parallel to the dipole at a distance of a quarter working wavelength ($\lambda/4$) below the antenna to produce efficient radiation. The PEC behaves as an electromagnetic mirror, giving the minimum

destructive interference at this position. However, the antenna cannot radiate efficiently when positioned nearer to a PEC ground plane due to the reverse image currents and the resulting destructive effects on the emitted wave pattern.[26] Therefore, there is a fixed physical length between the antenna and the ground plane in terms of working wavelength, thus presenting serious challenges in the high-frequency (3-30 MHz) and very-high-frequency (30-300 MHz) range, where the wavelength is relatively long and the excessive height of antenna above the ground plane restricts integration into a single, small-scale platform.

To solve this problem, "artificial" metasubstrate structures have been realized by resonating embedded circuits stacked in dielectric substrates to replace the PEC ground plane, and to improve the efficiency of dipole antennas where the dipole is placed near the ground plane.[27] Substrate structures reported include parallel dielectric slabs loaded by split-ring resonators (SRRs)-like structures e.g. loop circuit resonators,[28] spiral loops,[29] "Omega" medium resonators,[30,31] and mushroom-like structures.[32] However, these structured ground planes are generally narrowband and otherwise lossy, and are inevitably bulky because their thicknesses are dictated by the metallic resonator dimensions.

Here, the performance of a low profile dipole antenna placed one hundredth of working wavelength above a thin non-metallic magneto-dielectric ground plane is explored. The effects of permittivity and permeability of the ground plane on the radiation produced are evaluated. Moreover, electromagnetically anisotropic materials based on those demonstrated experimentally in the precious section are investigated with

various patterning arrangements on the ground plane in a parametric simulation study. The radiation pattern, reflection coefficient and realized gain of the dipole antenna is shown to be strongly affected by anisotropy in the ground plane, and under an optimum arrangement the performance of the antenna with a 25 times height reduction was shown to be even better than that of traditional arrangements.

6.2.2 Antenna Design

The magneto-dielectric ground planes were designed for the simple case of a dipole with a length of half a wavelength ($\lambda/2$) using the COMSOL Multiphysics RF module. The ground plane and the dipole antenna arrangement was assumed to be operating at 30 MHz, consistent with the anisotropic electromagnetic properties of the tiles measured in the previous section.

The dipole antenna system is shown schematically in Fig. 6.16. In the 3D simulation model, the dipole length was 0.5 $\lambda_{30\ \mathrm{MHz}}$, radius 0.0125 $\lambda_{30\ \mathrm{MHz}}$, and gap source size 0.0025 $\lambda_{30\ \mathrm{MHz}}$, where $\lambda_{30\ \mathrm{MHz}}$ = 10 m is the free space wavelength at 30 MHz. The material properties of the dipole was assigned as copper and a port source of 1 V operating voltage and 50 Ω characteristic impedance was used. A finite ground plane with a PEC surface and size of 0.7 $\lambda_{30\ \mathrm{MHz}}$ × 0.7 $\lambda_{30\ \mathrm{MHz}}$ × 0.005 $\lambda_{30\ \mathrm{MHz}}$ was assumed. The height of the dipole over the top of the magneto-dielectric ground plane was one hundredth of wavelength i.e. 0.01 $\lambda_{30\ \mathrm{MHz}}$. As is standard in simulations of this type, a perfectly matched layer (PML) sphere was assumed to act as an absorber of outgoing radiation to truncate the computational region at a radius of 0.625 $\lambda_{30\ \mathrm{MHz}}$ and a

thickness of 0.125 $\lambda_{30\ \mathrm{MHz}}$. The reflection coefficient (S_{11}) was simulated as a function of frequency from 1 to 50 MHz, from which the antenna resonant frequency f_0 can be determined. At f_0, the directivity D, which is the maximum radiation in any given direction, and the realised gain G_r, which is the maximum radiation in any direction taking into account the reflection coefficient, were obtained from the simulation results. These are standard and validated approaches for Comsol simulations of this type and no particular new routines and algorithms were needed, only the description of the ground plane anisotropy.

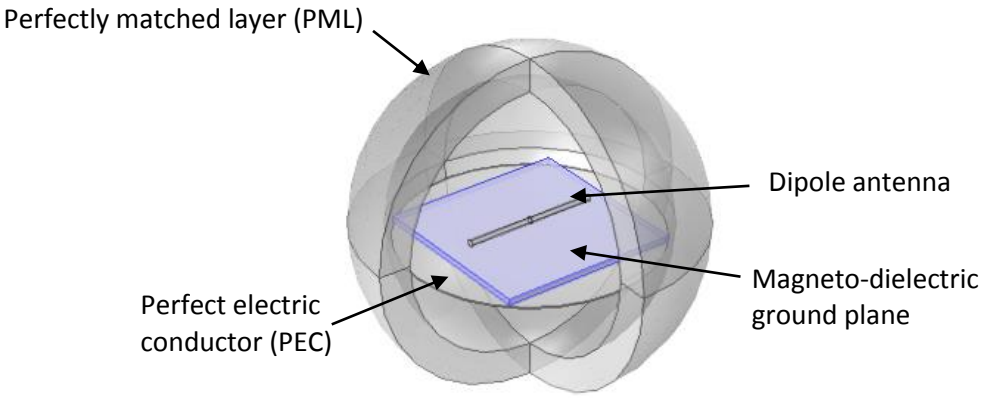

FIG. 6.16. A dipole antenna above a ground plane. The dipole consists of two cylindrical arms of conductive material with a voltage source in between. The computational region of free space is bounded by a perfectly matched layer (PML) that surrounds the antenna system, and over which various propagating wave or radiation properties may be evaluated.

6.2.3 Results and Discussion

Firstly, to show the adverse effects of positioning a dipole antenna too close to a PEC ground plane, the simulated reflection coefficient (S_{11}) values of a dipole in free space, a dipole at a quarter wavelength ($\lambda_{30\ MHz}/4$) above a PEC ground plane, and a dipole at one hundredth wavelength ($\lambda_{30\ MHz}/100$) distance above a PEC ground plane were compared. Fig. 6.17 shows the simulated reflection coefficients, and Table 6.2 lists representative dipole antenna performance parameters for these three arrangements. It is assumed that the materials of the ground plane itself were lossless (a typical, but questionable assumption in practice).

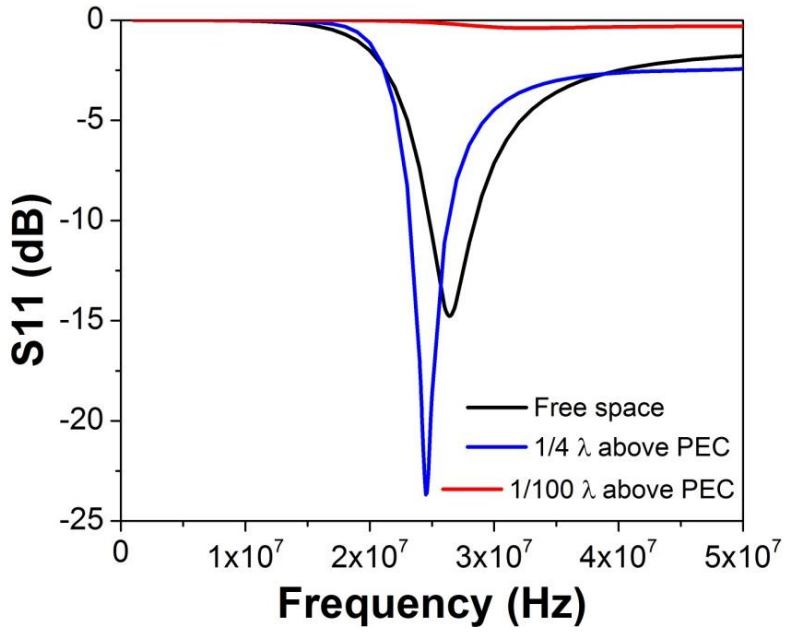

FIG. 6.17. Comparison of reflection coefficients for dipole antenna in free space, a quarter wavelength above a PEC, and one hundredth wavelength above a PEC.

Table 6.2. Comparison of dipole antenna performance in free space, a quarter wavelength above a PEC, and one hundredth wavelength above a PEC.

	f_0 (MHz)	S11 (dB)	D (dBi)	Gr (dBi)
Free space	26.4	-14.77	1.96	1.95
¼ λ above PEC	24.5	-23.68	7.56	7.56
1/100 λ above PEC	33	-0.39	6.21	-1.67

The results show that the dipole antenna in free space has a low reflection coefficient and the input energy was efficiently transferred into radiation. The directivity of the simulated dipole in free space is 1.96 dBi, which is in reasonable agreement with a theoretical directivity of 2.15 dBi.[33] The best (lowest) reflection coefficient of -23.68 dB was achieved by the traditional implementation of placing the antenna $\lambda/4$ above the PEC. When the dipole antenna was placed closer to the PEC ground plane at $\lambda/100$, the reflection coefficient increased dramatically to -0.39 dB, meaning that very little energy was radiated and giving a very poor realised gain. The reason is that the PEC surface induces a 180° phase change in the reflection so that the direction of the image current is opposite to that of the original dipole. The radiation from the reverse image current impedes the radiation from the original dipole due to their close proximity, resulting in a poor reflection coefficient and low radiation efficiency.

Maintaining the antenna arrangement in Fig. 6.16, the properties of the magneto-dielectric ground plane were investigated to understand if the performance of low profile antenna could be improved. The influence of both isotropic changes in ε and μ, and anisotropic variations in ε and μ, on the performance of the antenna were explored with the objective of identifying an optimum arrangement where the antenna had an acceptably low reflection coefficient and a high realised gain.

The antenna performance when arbitrarily varying the permittivity of the ground plane is shown in Fig. 6.18 and Table 6.3, with no obvious effects on the still very poor reflection coefficient $\lambda/100$ for ε = 5 or 100. The slightly decreased reflection coefficient compared with the case of the antenna directly above a PEC is simply due to the slightly increased antenna height of 0.005 λ as a result of the insertion of the magneto-dielectric ground plane. An increase in permittivity resulted in a slight increase in the reflection coefficient, and therefore decreased realised gain value, because the stored electrical energy of a high permittivity ground plane is increased and introduces capacitive coupling between the antenna, which degrades the antenna performance.[27]

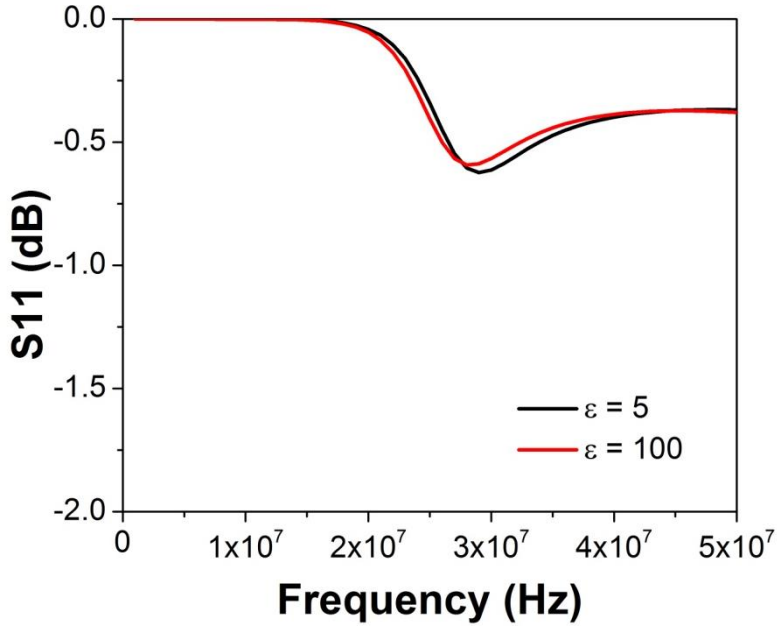

FIG. 6.18. Reflection coefficient as a function of frequency for an isotropic ground plane with ε = 5 and 100, μ = 1 and antenna height of $\lambda_{30\ \mathrm{MHz}}$ /100.

Table 6.3. Effect of permittivity on radiation properties of isotropic ground plane with ε = 5 and 100, μ = 1 and antenna height of $\lambda_{30\ \mathrm{MHz}}$ /100.

μ = 1	f_0 (MHz)	S11 (dB)	D (dBi)	Gr (dBi)
ε = 5	29	-0.62	6.06	0.04
ε = 100	28	-0.59	5.91	-0.31

Fig. 6.19 shows the antenna performance for changes in permeability in the range μ = 5 to 100 for an isotropic ground plane with ε = 1. The antenna resonant peak shifts to lower frequency as the substrate permeability increase. This is because the effective refractive index of the antenna medium (composed of air and the substrate) increases, leading to an increase in the antenna electrical length ($l_{electrical} = l_{\mathrm{physical}} \times n_{eff} = l_{\mathrm{physical}} \times (\mu_{eff}'\varepsilon_{eff}')^{1/2}$) and hence resonance occurs at a lower frequency where the wavelength is longer. The antenna now resonated at different frequencies (identified by black primary f_{01} and red secondary f_{02} dots), which is known as dual-band or multi-band operation, and antennas that can support multi-band transmitting and receiving within a single radiating device are desirable for some applications.[34] The primary resonance happens when the antenna electrical length is half the wavelength ($l_{electrical} = \lambda/2$), and the secondary resonance occurs when the antenna electrical length and the wavelength are equal ($l_{electrical} = \lambda$). The radiation parameters at the two resonant frequencies f_{01} and f_{02} are listed in Tables 6.4 (a) and (b). In general, increasing the permeability reduced the reflection coefficient and improved radiation efficiency, because the introduced inductance (due to permeability) counteracted the capacitive behaviour of the resonant behaviour, and hence reduced the coupling between the antenna and the ground plane.[27] When the permeability increased, the resonant frequencies of the antenna, which are inversely proportional to the refractive index ($n = \sqrt{\varepsilon\mu}$) of the ground plane, reduced as expected. The increase in permeability from 5 to 30 had the most marked

effect on directivity and gain, with little or no further improvement at higher permeabilities.

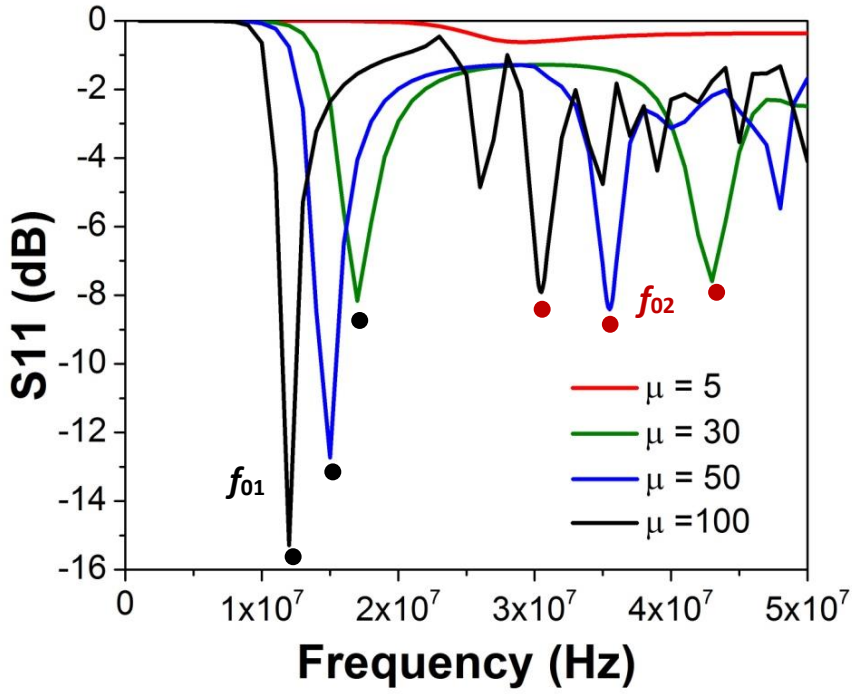

FIG. 6.19. Reflection coefficient for an isotropic ground plane for μ = 5 to 100, ε = 1 and antenna height of $\lambda_{30\ MHz}$ /100.

Table 6.4(a). Effect of permeability on radiation properties of isotropic ground plane for μ = 5 to 100, ε = 1 and antenna height of $\lambda_{30\ MHz}$ /100: at 1st resonance.

ε =1	f_{01} (MHz)	S11 (dB)	D (dBi)	Gr (dBi)
μ = 5	29	-0.62	4.57	-1.45
μ = 30	17	-8.16	5.81	5.71
μ = 50	15	-12.73	5.70	5.69
μ = 100	12	-15.29	4.77	4.77

Table 6.4(b). Effect of permeability on radiation properties of isotropic ground plane for μ = 5 to 100, ε = 1 and antenna height of $\lambda_{30\ MHz}$ /100: at 2nd resonance.

ε =1	f_{02} (MHz)	S11 (dB)	D (dBi)	Gr (dBi)
μ = 5	-	-	-	-
μ = 30	43	-7.59	4.99	4.86
μ = 50	35.5	-8.41	3.38	3.29
μ = 100	30.5	-7.91	6.31	6.19

To investigate the interaction between permittivity and permeability on the performance of antennas, the reflection coefficient for a ground plane with μ = 30 and ε varying from 1 to 15 is shown in Fig. 6.20. A change in permittivity alone again had little effect on the reflection coefficient, similarly to when μ = 1, as previously shown in Fig. 6.18 and Table. 6.3.

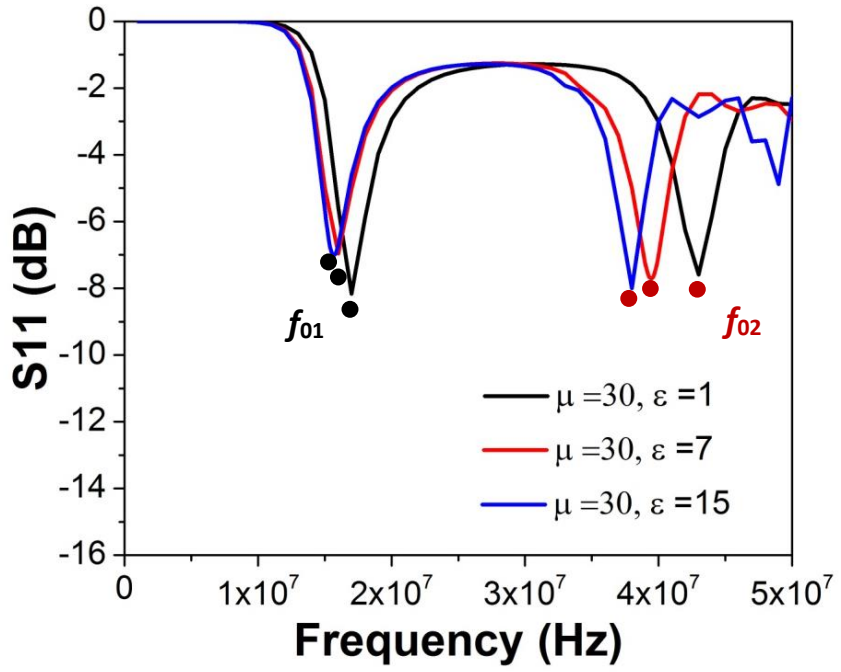

FIG. 6.20. Reflection coefficient for an isotropic ground plane for ε = 1 to 15, μ = 30 and antenna height of $\lambda_{30\ \mathrm{MHz}}$ /100.

As shown by the prior results, the radiation performance of an antenna depends on the often complicated interactions between the antenna radiation and the ground plane radiation due to the complex induced current flow patterns on the ground plane. Consequently it was hypothesized that anisotropic electromagnetic materials that would influence induced current flow and the resulting electromagnetic wave

propagation may have a strong effect on the overall antenna radiation performance. Surprisingly, this is an area that received little attention in the literature, although the more general case of electromagnetic band-gap (EBG) ground planes have been studied for low profile antenna applications and a 12.5 times reduction in antenna height has been reported.[35] An EBG ground plane is normally made of arrays of metal protrusions on a flat metal sheet, such as mushroom-like structure.[36] They behave as a network of resonant *LC* circuits that act as electric filter to block the flow of currents and do not support propagating surface waves in a forbidden frequency band, thus the antenna can radiate efficiently without interference along the ground plane.[36] However, the EBG is generally narrowband and rather bulky and heavy. More attractive characteristics might be provided if polymer-based anisotropic composites could serve to provide a similar or even better performance to the EBG ground plane approach, but to the best of author's knowledge this approach has not been reported.

To base the study of anisotropic effects within sensible limits, the anisotropic tiles previously described were taken as the "building blocks" of the ground plane, and their arrangement of radiation properties studied. The tiles introduced in section 6.1.3.3 were described using tensors with the practically achieved properties:

$$\varepsilon = \begin{bmatrix} 7 & 0 & 0 \\ 0 & 4.7 & 0 \\ 0 & 0 & 7 \end{bmatrix} \tag{6.13a}$$

$$\mu = \begin{bmatrix} 30 & 0 & 0 \\ 0 & 2 & 0 \\ 0 & 0 & 30 \end{bmatrix} \tag{6.13b}$$

The conceptual design of the anisotropic ground plane is shown in Fig. 6.21, where the anisotropic materials were arranged in a way that the ordinary axis with larger values of permittivity and permeability, were aligned at an angle α to the in-plane *x*-axis defined in a "first" tile, which occupied one quarter of the ground plane area. The remaining three tiles to complete the ground plane area are then simply mirror images across the *x*- and *y*-axis of the first tile. The principle variable under investigation was the angle α.

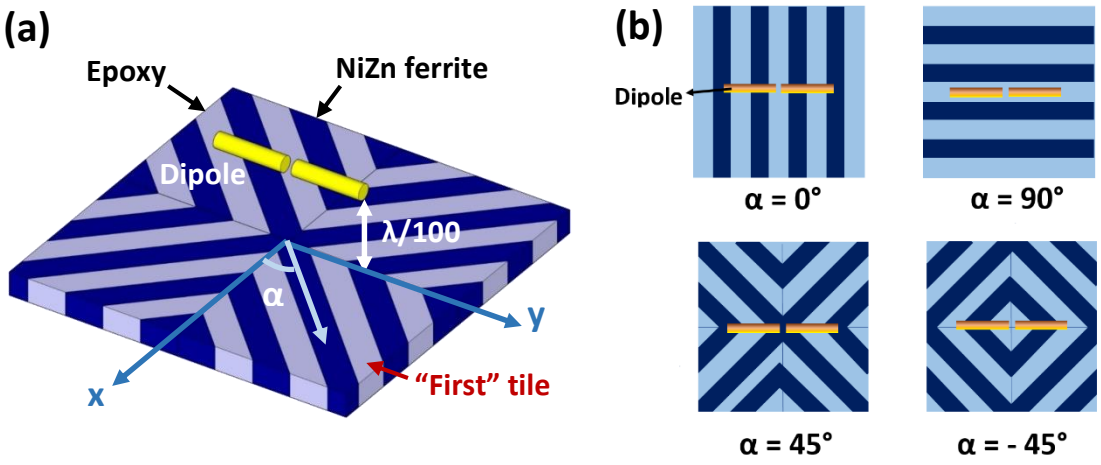

FIG. 6.21. Schematics of (a) a low profile dipole antenna over an anisotropic magneto-dielectric ground plane, comprised of low permeability epoxy and high permeability NiZn ferrite bars; and (b) plan view of tile arrangement examples at α = 0, ±45, 90°.

The reflection coefficients as a function of frequency against the variation of the anisotropic materials patterning for α = 0, ±30, ±45, ±60, 90°and antenna height of $\lambda_{30\,\mathrm{MHz}}$/100 are shown in Fig. 6.22, and the corresponding antenna radiation parameters are listed in Table 6.5 in the standard format used previously. Two resonant peaks are again shown in these cases, where the resonant frequency with the lower reflection coefficient value is preferable as the antenna working frequency.

The arrangement of the anisotropic tiles on the ground plane had a strong effect on the radiation performance. The best (lowest) reflection coefficient was -35.9 dB when the material ordinary axis was aligned $\alpha = 60°$ to the *x*-axis. However, under these conditions, the antenna also exhibited quadfurcation in the radiation direction at the resonant frequency of 57 MHz, as shown in Fig. 6.23, which shows a plot of 3D radiation pattern that refers to the directional dependence of the emitting radiation strength from the antenna. The appearance of the split four lobes dispersed the power radiated by the antenna and resulted in a relatively low realised gain of 2.69 dBi. When $\alpha = 30°$ and 45°, the reflection coefficients reduced to -21.7 dB and -17.6 dB respectively, while the realised gain reached as high as 8.71 dBi at 44.5 MHz and 8.39 dBi at 48 MHz respectively.

Figs. 6.24(a) to (d) show the 3D radiation patterns and elevation plane patterns for the same dipole antenna at 1/4 λ above PEC, 1/100 λ above PEC, 1/100 λ above an isotropic ground plane with $\varepsilon = 7$, $\mu = 30$, and 1/100 λ above anisotropic ground plane with $\alpha = 30^0$ respectively. 3D radiation patterns are useful for visualizing the antenna radiation directions. In order to better quantify the antenna radiation behaviour, the elevation pattern is typically formed by slicing the 3D pattern through an orthogonal plane and presented in a Cartesian coordinate system, where θ is the angle measured to the *z*-axis, and φ is the angle measured counter-clockwise to the *x*-axis. For the traditional implementation of dipole antenna using a PEC at a distance of 1/4 λ below the antenna, a unidirectional radiation pattern is produced, as shown in Fig. 6.24(a), where the PEC ground plane acts as a good reflector as mentioned earlier. Fig. 6.24(a)

shows that a realised gain of 7.56 dBi can be achieved at the main lobe, which refers to the radiation lobe containing the direction of maximum radiation. As the antenna is too close to the PEC ground plane at a distance of 1/100 λ, the reverse image currents in PEC cancel the currents in the antenna, leading to a high return loss of -0.39 dB and resulting in a very poor realised gain of -1.67 dBi at the main radiation lobe [see Fig 6.24(b)]. In comparison, as shown in Fig. 6.24(c), when the dipole antenna is 1/100 λ above the ground plane, the insertion of an isotropic magneto-dielectric substrate in addition to the PEC not only increased the main lobe gain from -1.67 dBi to 3.30 dBi, and the back lobe of the antenna that faces the ground plane also increased dramatically from -19.38 dBi to 0.71 dBi. As previously described, this is due to the increased inductive surface impedance as a consequence of increased substrate permeability.[37] When the isotropic magneto-dielectric substrate changed to an anisotropic ground plane with an arrangement of $\alpha = 30^0$, the radiation of the antenna was further enhanced to a realised gain of 8.39 dBi at the main lobe, as shown in Fig. 6.24(d). The superior performance of the anisotropic substrate over the isotropic substrate with the same values of ε and μ must derive from changes in the ground plane surface current flow and suppressed surface wave propagation. However the experimental verification of the benefit of anisotropic ground planes and a more detailed understanding of the underlying mechanisms lies in the domain of the electrical or antenna engineer in future work, and was considered out of scope of the current work focused on materials.

Overall, the simulations provide strong encouragement that proper manipulation of the electromagnetic anisotropy of the ground plane can maintain or even enhance the

performance of low profile antenna (higher realized gain and equivalent reflection coefficient).

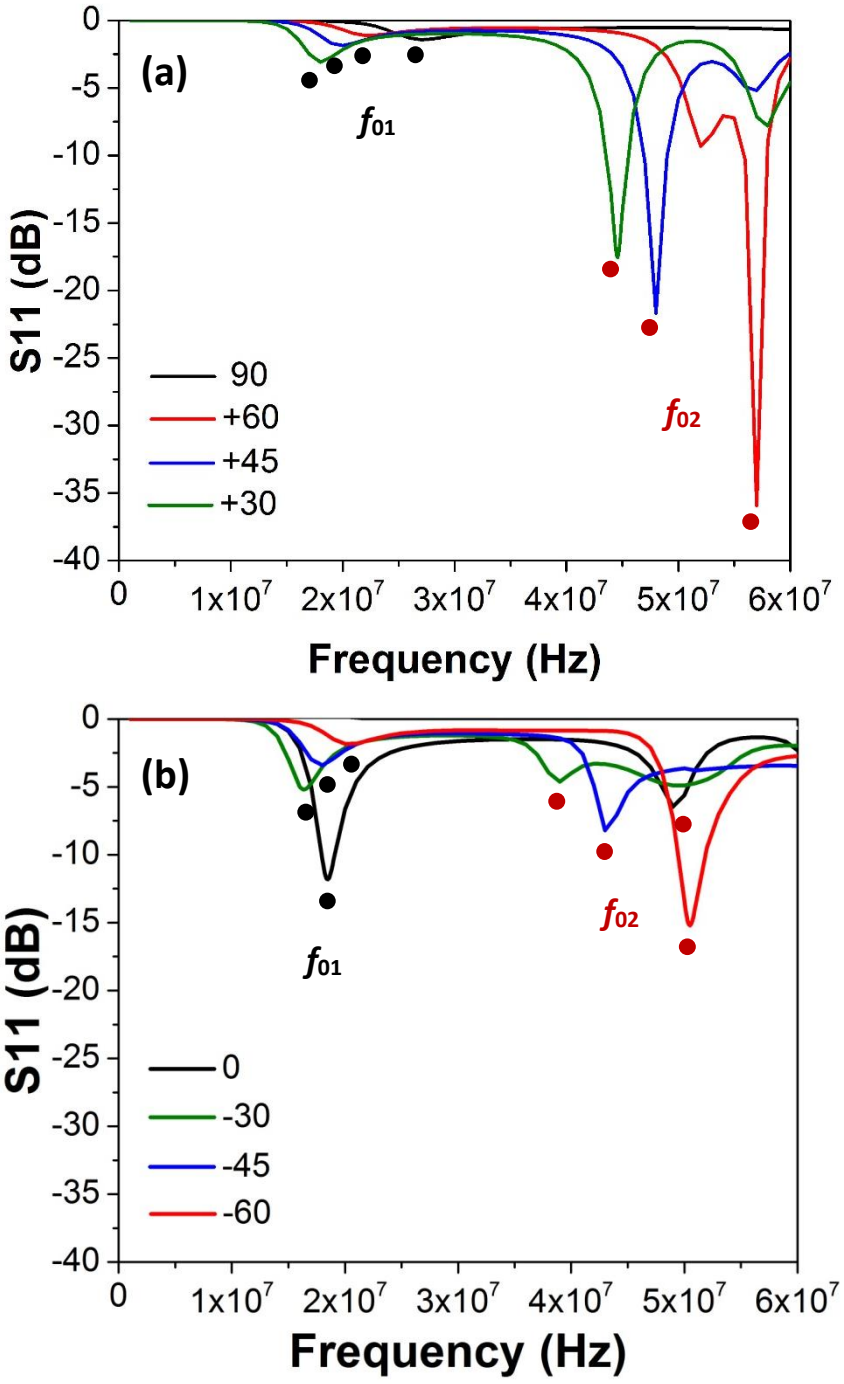

FIG. 6.22. Reflection coefficient for a uniaxial anisotropic ground plane with ε_o = 7, μ_o =30 and ε_e = 4.7, μ_e = 30 and antenna height of $\lambda_{30\ \mathrm{MHz}}$ /100 for α changes (a) from 30 to 90 degree, and (b) from -60 to 0 degree with uniaxial anisotropic material ε_o = 7, μ_o = 30 and ε_e = 4.7, μ_e = 30.

Table 6.5(a). Effect of anisotropic material patterning on radiation properties of ground plane for α = 0, ±30, ±45, ±60, 90° and antenna height of $\lambda_{30\ MHz}$ /100: at 1st resonance.

	f_{01} (MHz)	S11 (dB)	D (dBi)	Gr (dBi)
α = 90°	27	-0.64	5.57	-0.39
α = 60°	22	-1.11	4.97	0.98
α = 45°	20	-1.85	4.84	2.43
α = 30°	18	-3.08	4.88	3.68
α = 0°	18.5	-11.81	6.34	6.32
α = -30°	16.4	-5.18	5.14	4.72
α = -45°	18	-3.42	4.99	3.98
α = -60°	20	-1.84	4.82	2.39

Table 6.5(b). Effect of anisotropic material patterning on radiation properties of ground plane for α = 0, ±30, ±45, ±60, 90°and antenna height of $\lambda_{30\ MHz}$ /100: at 2nd resonance.

	f_{02} (MHz)	S11 (dB)	D (dBi)	Gr (dBi)
α = 90°	-	-	-	-
α = 60°	57	-35.93	2.69	2.69
α = 45°	48	**-21.70**	8.39	**8.39**
α = 30°	44.6	**-17.56**	8.71	**8.71**
α = 0°	49	-6.47	1.37	1.14
α = -30°	39	-4.62	4.97	4.42
α = -45°	43	-8.21	5.15	5.05
α = -60°	50.5	-15.20	5.50	5.50

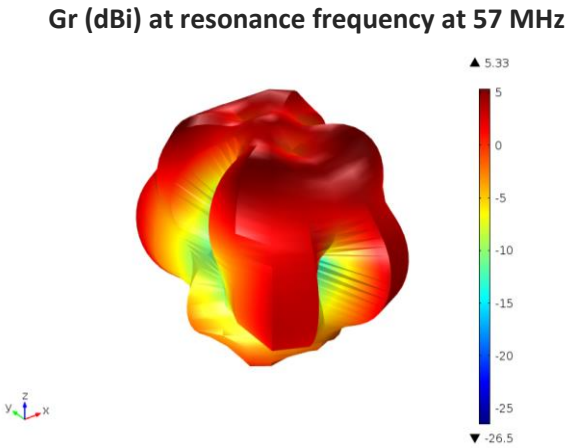

FIG. 6.23. 3D radiation pattern exhibiting quadfurcation for α = 60° at a resonant frequency of 57 MHz.

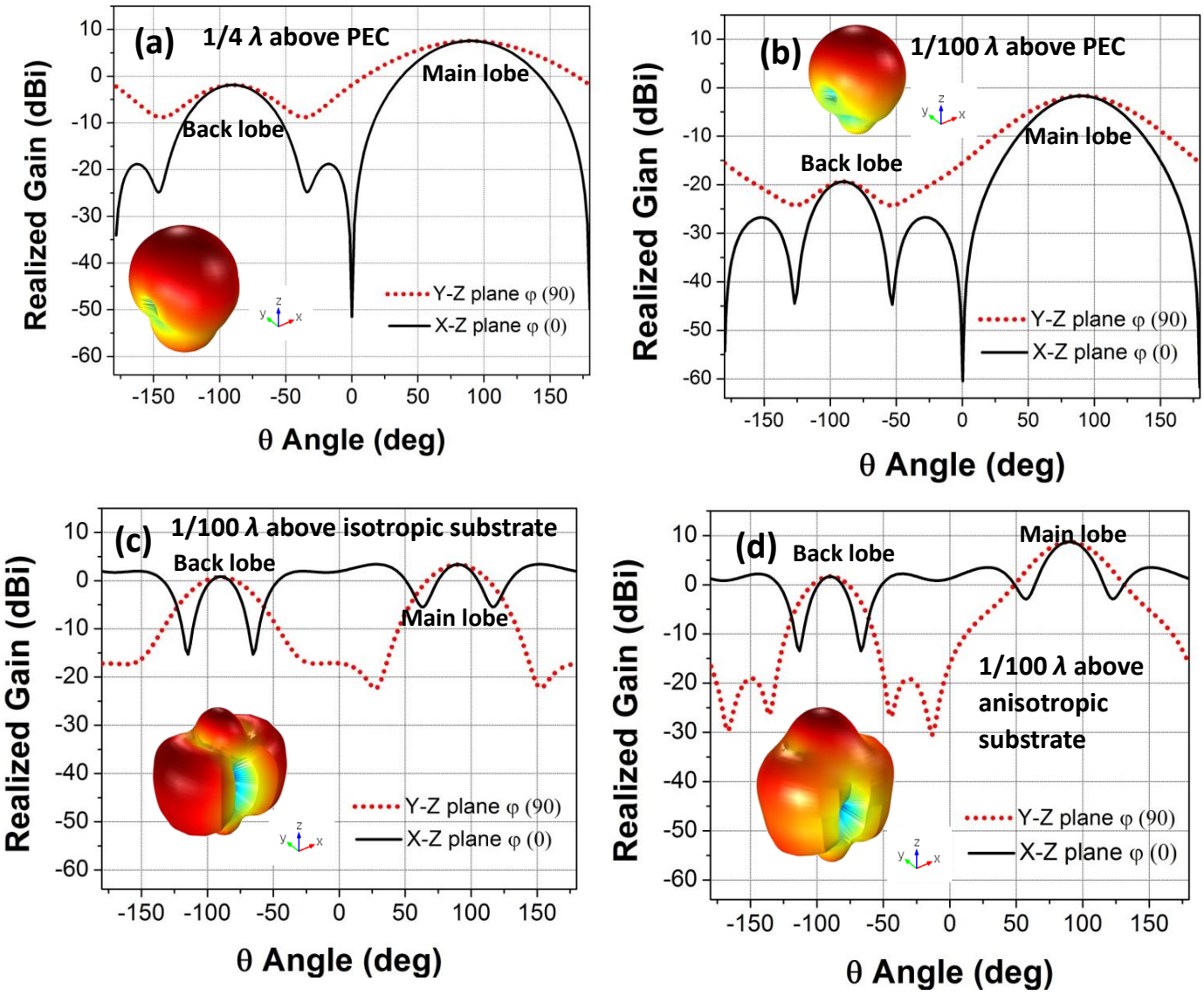

FIG. 6.24. Radiation pattern comparison of the dipoles at their resonant frequencies. (a) 1/4 λ above PEC at 26.4 MHz; (b) 1/100 λ above PEC at 33 MHz; (c) 1/100 λ above isotropic ground plane with $\varepsilon = 7$, $\mu = 30$ at 39.5 MHz; and (d) 1/100 λ above anisotropic ground plane with $\alpha = 30^0$. The insets show the corresponding 3D radiation patterns for each case.

6.2.4 Conclusions

Simulations of the effect of various types of ground plane for a simple dipole antenna arrangement have been performed. The magneto-dielectric material parameters of permittivity, permeability and anisotropy were evaluated respectively by performing parametric simulations based on practically realized materials developed in this thesis. The arrangement of ground plane anisotropy had a strong effect on antenna radiation characteristics. By placing a dipole antenna over a thin anisotropic structured ground plane with a thickness of only 0.005 λ rather than a PEC ground plane, a reduction of 25 times in antenna height was suggested, with superior performance.

Bibliography

1 J. B. Pendry, D. Schurig, and D. R. Smith, Science **312**, 1780 (2006).

2 A. J. Ward and J. B. Pendry, J. Mod. Opt. **43**, 773 (1996).

3 J. Li and J. B. Pendry, Phys. Rev. Lett. **101**, 203901 (2008).

4 R. Liu, C. Ji, J. J. Mock, J. Y. Chin, T. J. Cui, and D. R. Smith, Science **323**, 366 (2009).

5 D. Lu and Z. Liu, Nat. Commun. **3**, 2176 (2012).

6 M. Rahm and D.Roberts Schurig, D. A.Cummer, S. A.Smith, D. R.Pendry, J. B., Photo. Nano. Fund. Appl. **6**, 87 (2008).

[7] M. Cummer Rahm, S. A.Schurig, D. Pendry, J. B. Smith, D. R., Phys. Re. Lett. **100**, 063903 (2008).

[8] D. Huangfu, S. Xi, F. Kong, J. Zhang, H. Chen, D. Wang, B. Wu, L. Ran, and J. A. Kong, J. Appl. Phys. **104**, 014502 (2008).

[9] W. X. Jiang, T. J. Cui, X. Y. Zhou, X. M. Yang, and Q. Cheng, Phys. Rev. E **78**, 066607 (2008).

[10] Z. H. Jiang, M. D. Gregory, and D. H. Werner, IEEE Trans. Antennas Propag. **60**, 5063 (2012).

[11] Q. Wu, Z. H. Jiang, O. Quevedo-Teruel, J. P. Turpin, W. Tang, Y. Hao, and D. H. Werner, IEEE Trans. Antennas Propag. **61**, 5910 (2013).

[12] J. Valentine, S. Zhang, T. Zentgraf, E. Ulin-Avila, D. A. Genov, G. Bartal, and X. Zhang, Nature **455**, 376 (2008).

[13] K. J. Stebe, E. Lewandowski, and M. Ghosh, Science **325**, 159 (2009).

[14] Q. Liu, Y. Cui, D. Gardner, X. Li, S. He, and I. I. Smalyukh, Nano Lett. **10**, 1347 (2010).

[15] T. Liu, P. H. Zhou, J. L. Xie, and L. J. Deng, J. Magn. Magn. Mater. **324**, 519 (2012).

[16] K. Oh, H. Lee, W. Lee, M. Yoo, W. Kim, and H. Yoon, J. Magn. Magn. Mater. **321**, 1295 (2009).

[17] S. Yoshida, M. Sato, E. Sugawara, and Y. Shimada, J. Appl. Phys. **85**, 4636 (1999).

[18] W. Wang, T. Ma, and M. Yan, J. Alloys Compd. **459**, 447 (2008).

[19] T. D. Zhou, P. H. Zhou, D. F. Liang, and L. J. Deng, J. Alloys Compd. **484**, 545 (2009).

[20] L. Liu, Z. H. Yang, C. R. Deng, Z. W. Li, M. A. Abshinova, and L. B. Kong, J. Magn. Magn. Mater. **324**, 1786 (2012).

[21] M. Wu, H. He, Z. Zhao, and X. Yao, J. Phys. D: Appl. Phys. **34**, 1069 (2001).

[22] W. B. Weir, Proc. IEEE **62** (1), 33 (1974).

[23] A. M. Nicolson and G. F. Ross, IEEE Trans. Instrum. Meas. **19** (4), 377 (1970).

[24] R. E. Collin, IRE Trans. Microw. Theory Techn. **6**, 206 (1957).

[25] J. L. Snoek, Physica **14**, 207 (1948).

[26] W. L. Stutzman and G. A. Thiele, *Antrnna Theory and Design*, 2nd ed. (Wiley, New York, 1998).

[27] H. Mosallaei and K. Sarabandi, IEEE Trans. Antennas Propagat. **52**, 1558 (2004).

[28] H. Mosallaei and K. Sarabandi, IEEE Trans. Antennas Propagat. **55**, 45 (2007).

[29] P. Mookiah and K. R. Dandekar, IEEE Trans. Antennas Propagat. **57**, 3283 (2009).

[30] M. M. Saadoun and N. Engheta, PIER **9**, 351 (1994).

[31] K. Buell, H. Mosallaei, and K. Sarabandi, IEEE Trans. Microwave Theory Tech. **54**, 135 (2006).

[32] F. Yang and Y. Rahmat-Samii, IEEE Trans. Antennas Propagat. **51**, 2691 (2003).

[33] C. A. Balanis, *Antenna Theory, Analysis and Design*. (John Wiley and Sons, Inc., 1997).

[34] C. J. Lee, K. Leong, and T. Itoh, Proceedings of the 36th European Microwave Conference (2006).

[35] J. M. Bell and M. F. Iskander, IEEE Antennas Wireless Propag. Lett. **3**, 223 (2004).

[36] D. Sievenpiper, L. Zhang, R. F. Jimenez Broas, N. G. Alexopolous, and E. Yablonovitch, IEEE Trans. Microw. Theory Techn. **47**, 2059 (1999).

[37] N. Altunyurt, M. Swaminathan, P. M. Raj, and V. Nair, Electronic Components and Technology Conference, 59th, 26-29 May, 801 (2009).

Chapter 7

3D Printing of Ferrite/ABS Magnetic Composites for Electromagnetic Devices

This chapter introduces a 3D printing (additive manufacture) technique as a versatile fabrication method that offers the potential to realize complex 3D devices with metamaterial characteristics in a single process directly from a computer aided design. However, the range of functional devices that might be realized by 3D printing is limited by the current range of materials that are compatible with a given 3D printing process. In this chapter, fused deposition modelling (FDM), which is a widely used 3D printing method is explored, which typically employs only common thermoplastic filaments as feedstock. The development of a magnetic feedstock filament based on polymer-ferrite composite that is compatible with FDM is investigated, and the properties of various printed structures are assessed. Due to time constraints, this chapter provides essentially only a proof-of-concept (significant time was spent on developing the printable filament), but showed enormous potential for future printed devise and productive lines of future research

7.1 Introduction

As described in previous chapters, practical challenges remain in device fabrication based on metamaterials or that induce metamaterials-like effects. In particular there is an ongoing need to reliably realise spatial variations in permittivity and permeability, which for microwaves must take place over a few mm to several cm's, and with a "dynamic range" (difference in the lowest to highest permittivity or permeability values) that is most useful when it as large as possible. Fused deposition modelling (FDM) is an additive manufacturing process that can place different thermoplastic polymers at different locations in three dimensions with ~ 100 μm precision, and has been used for the fabrication of devices that operate at microwave frequencies, including an X-band Luneburg Lens where the gradient permittivity ranged from 1.01 to 2.7 by mixing the ratio of air (voids in the structure) and polymer,[1] an anisotropic material using a printed spatially varying lattice,[2,3] a meander line dipole antenna,[4] and channel emulator.[5] However so far, these printed devices were based on spatial variations in permittivity ε only (i.e. permeability μ = 1), restricting the design freedom and limiting the device performance. For example, reflection losses can arise due to the impedance mismatch $Z = (\mu/\varepsilon)^{1/2}$ when only ε is varied.

This chapter focuses on additive manufacture using the FDM process operating with a polymer-based composite filament containing NiZn-ferrite particles. Strategies to disperse the ferrite in the filaments and the printed part are described. A range of ferrite loadings have been investigated, with a maximum printable fraction of 25 vol%. The

printed magnetic permeability is investigated as a function of frequency, and shows permeability > 1 beyond 2 GHz, which is rare amongst magnetic materials whose magnetic properties usually degrade quickly, or are even absent (permeability close to 1), as the frequency exceeds 100 MHz, and especially above 1 GHz due to ferromagnetic resonant behavior.[6,7] The microstructures of the printed materials are characterized and the permittivity and permeability measured using a stripline technique.[8]

It is shown the FDM approach offers increased design freedom to manipulate both permittivity and permeability spatially, along with the capability to do this in relatively complex geometries and structures direct from a CAD file, helping to enable a new range of spatial transformation (ST) - designed devices in practice.

7.2 Experimental

The development of 3D printable magnetic composites involved three main steps; selection of a non-toxic printable thermoplastic matrix for the composite that can be printed and extruded with ferrite powders, development of composite feedstock for the 3D printing process, and optimization of 3D printing parameters. Acrylonitrile butadiene styrene (ABS) polymer (MFI-22, Silvergate Plastics Ltd, UK), which is a readily available modeling plastic, was chosen as the matrix polymer in this preliminary investigation due to its well-known ease of printing, low cost and wide availability. Compounding of ABS and ferrite powder was done by dissolving ABS pellets in acetone assisted with thorough magnetic stirring. The sintered NiZn ferrite powder (F16 MagDev Ltd. UK) used elsewhere in this thesis was then dispersed in

acetone followed by 10 min ultrasonication in an ice bath, and then was poured into the ABS-containing solution under stirring. The resulting well-mixed slurry was spread on trays allowing for full evaporation of acetone in a fume cupboard. The resulting solid composite was then ground into small granules and extruded into filaments of ~ 1.8 mm diameter by a commercial single screw extruder (Noztek Ltd. UK) at 200 °C. The 3D printer used was a Makerbot Replicator but with nozzles modified (increased diameter) to avoid nozzle clogging that otherwise occurred with the most heavily loaded filaments.

Scanning electron microscopy (SEM) images were taken using a JEOL JSM-840F field emission electron microscope. The magnetic and dielectric properties of the composites were measured by a stripline technique[8] using a Rohde & Schwarz ZNB 20 Vector Network Analyzer (VNA).

7.3 Results and Discussion

Approximately 10 m of the in-house 1.8 mm diameter ABS-ferrite filament was fabricated and is shown in Fig. 7.1(a). The uniformity of filament diameter plays an important role in reliable 3D printing, and was controlled by careful manipulation of the extrusion temperature (170 – 185 °C) based on the contained ferrite fraction. In general, the ferrite fraction is desired to be as high as possible to provide the widest dynamic range of permeabilities across a printed device, but low enough so as to enable the material to exit the heated extrusion nozzle of the 3D printer. So far, optimizing across filament production, printing parameters (nozzle diameter ~0.7 mm, feed

diameter ~1.78 mm, feed rate ~90, platform temperature ~100 °C, extruder temperature ~230 °C),+ and reliable operation, the maximum fraction is 25 vol.% ferrite; at higher fractions the filament tends towards brittle behavior in feeding and became difficult to print.

The printability of the composite filament was assessed by printing simple blocks using the FDM process. The composite filament was driven by a stepper motor into a temperature controlled nozzle and molten material was extruded and deposited onto the build platform in a layer according to the pre-programmed pattern. At the end of each finished layer, the build platform was lowered and the next layer printed on top. Selection of optimized FDM parameters e.g. nozzle temperature, feed rate, traverse speed of the head, etc., was important for reliable printing. Fig. 7.1(b) shows printed blocks of pure ABS and ABS + 17 vol.% ferrite, and with a size that allowed them to be placed in the stripline jig immediately after printing so their electromagnetic properties could be quickly compared.

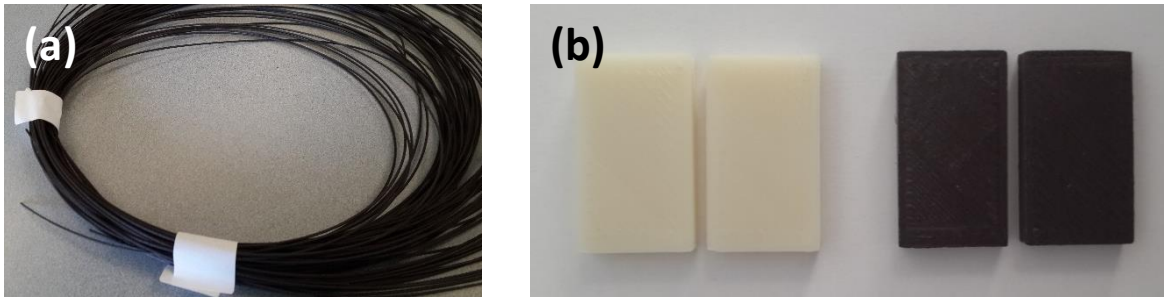

FIG. 7.1. Photographs of (a) in-house extruded ABS-17 vol.% NiZn ferrite filament; and (b) corresponding printed ABS (left) and ABS-17 vol.% NiZn ferrite (right) 30 × 17 × 4.8 mm blocks for electromagnetic characterization at microwave frequencies in a stripline jig.

Fig. 7.2 shows cross-sections of printed ABS-10 vol.%, 17 vol.% and 25 vol.% ferrite filaments, indicating an adequate homogeneity of ferrite particles in the ABS matrix in order to provide printability, although there were increasing small agglomerations as the ferrite fraction increased.

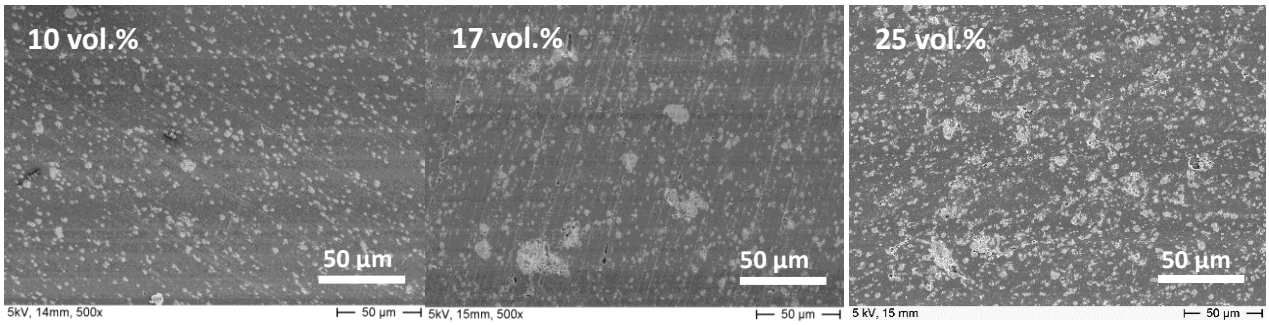

FIG. 7.2. Microstructures of printed blocks of ABS-10 vol.%, 17 vol.% and 25 vol.% ferrite.

The complex permittivity and permeability of printed blocks with different filler fractions were measured using a Rohde & Schwarz VNA and the stripline based measurement method used in Chapter 4 and Chapter 6. Fig. 7.3(a) shows that the permittivities of the printed composite materials remained almost constant with frequency. This is because the permittivity response of NiZn ferrites is provided by atomic and electronic polarization, which was largely independent of frequency over the measured range of 40 MHz to 2 GHz. The permeability displayed in Fig. 7.3(b) was approximately constant at ~ 2 up to 100 MHz for 25 vol% ferrite, and at ~ 1.3 up to 1 GHz for 10 vol.% ferrite, before reducing as the gyromagnetic resonance frequency was approached. Both permittivity and permeability of the composites increased with NiZn ferrite fraction.

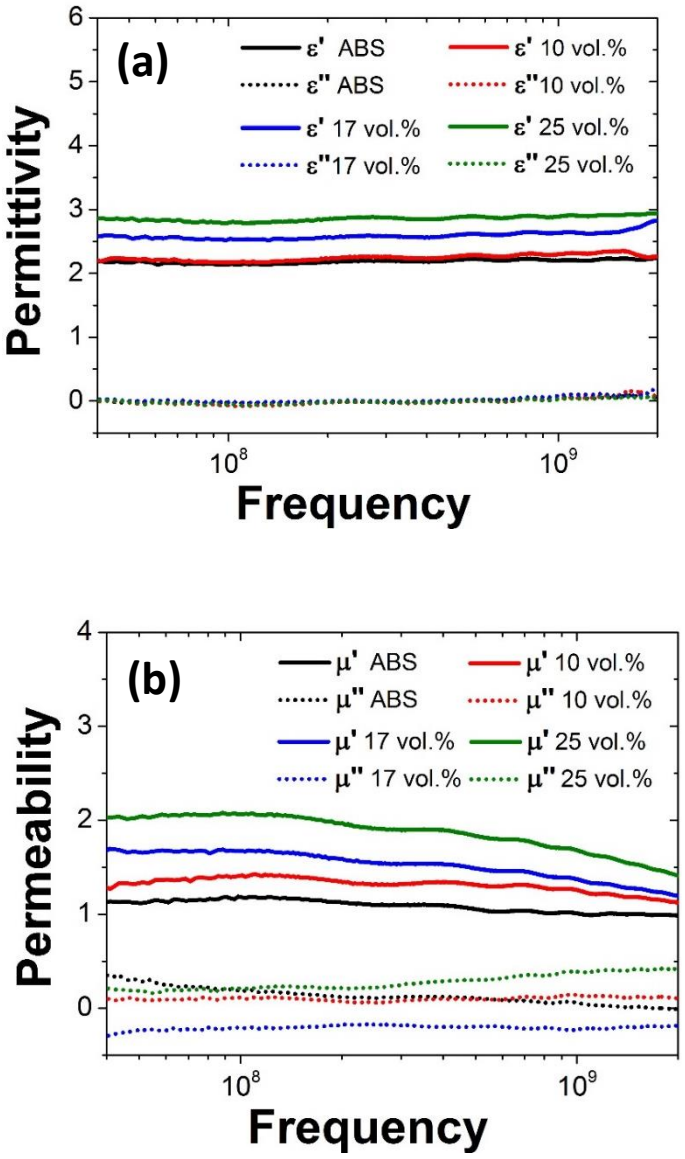

FIG. 7.3. Frequency dispersions of complex (a) permittivity and (b) permeability for printed ABS and ABS-10 vol.%, 17 vol.% and 25 vol.% NiZn ferrite.

When permittivity and permeability values below that of the filament are desired, the density of 3D printed material can be varied by including air in the form of controlled porosity. Further, a spatially varying, anisotropic all-dielectric metamaterial can be achieved by proper design of varying local porosity or oriented pores.[2] Now, the

magnetic feedstock developed in this study provides an additional degree of freedom to manipulate also the permeability of printed materials, extending the range of metamaterial-like devices that may be achieved by 3D printing in practice. To show the printability of developed composite filaments for more complex structures, Fig. 7.4 shows a magnetic diamond-like lattice structure.

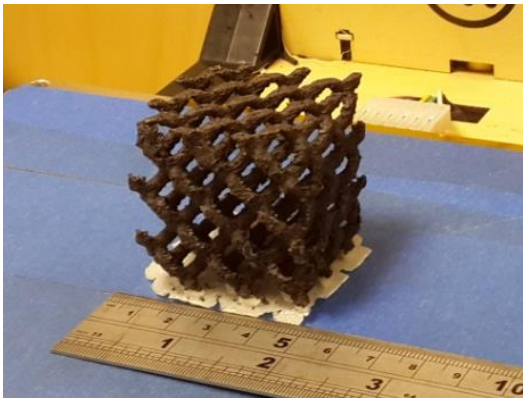

FIG. 7.4. Photograph of a 3D printed diamond-like lattice structure using in ABS-10vol% NiZn ferrite filament.

7.4 Conclusions

The processing route for magnetic composite filaments comprising NiZn ferrite micro-particles dispersed in acrylonitrile butadiene styrene (ABS) was developed. The magnetic filaments are then suitable for 3D printing of structures with a permeability up to 2. Optimization of the filament diameter and its uniformity, the nozzle diameter, and various printing parameters are critical for successful printing. The development of printable magnetic materials will enable the spatial manipulation of permeability

for designs obtained from spatial transformations that require gradient magnetic properties.

Bibliography

[1] M. Liang, W. R. Ng, K. Chang, M. E. Gehm, and H. Xin, Proc. IEEE Int. Microw. Symp., 1 (2011).

[2] R. C. Raymond C. Rumpf, R. G. Gesar, H. H. Tsang, J. E. Padilla, and M. D. Irwin, Prog. Electronmagn. Res. **142**, 243 (2013).

[3] C. R. Garcia, J. Correa, D. Espalin, J. H. Barton, R. C. Rumpf, R. Wicker, and V. Gonzalez, Prog. Electromagn. Res. **34**, 75 (2012).

[4] M. Ahmadloo, IEEE 22nd Conference on Electrical Performance of Electronic Packaging and Systems (EPEPS), 29 (2013).

[5] X. Jiao, H. He, G. Li, W. Qian, G. Shen, D. Pommerenke, C. Ding, D. White, S. Scearce, and Y. Yang, IEEE International Symposium on Electromagnetic Compatibility (EMC), 956 (2014).

[6] D. S. Gardner, A. M. Crawford, and S. Wang, IEEE International Interconnect Technology Conference, June, 101 (2001).

[7] T. Tsutaoka, T. Kasagi, T. Nakamura, and K. Hatakeyama, J. Phy. IV France **7**, C1 (1997).

[8] W. Barry, IEEE Trans. Microwave Th. Tech. **34**, 80 (1986).

Chapter 8

Conclusions and Future Work

8.1 Conclusions

This thesis has focused on the materials design and processing of magnetic composites in which the electrical and magnetic interactions with microwaves were achieved by loading various polymer matrices with relatively high permittivity and permeability particles. The work investigated a number of materials combinations and arrangements that provided composite materials with effective electromagnetic responses in the microwave regime that are difficult to find in naturally appearing or monolithic materials, including impedance matching and high magnetic anisotropy. Manufacturing approaches that were preferably inexpensive, scalable and capable of arranging materials in two or more dimensions were explored to fabricate composite materials with well-controlled permittivity and permeability. The developed manufacturing approaches were based on casting, spray deposition, and 3D printing.

Materials with relatively high (~ 6) and equal permeability and permittivity were fabricated by a scalable and flexible casting route, and it was experimentally demonstrated that at frequencies up to 100 MHz, a $Ni_{0.4}Zn_{0.6}Fe_2O_4$ ferrite/epoxy composite with a ferrite loading of 53 vol. % could achieve broadband impedance matching to free space with a refractive index of approximately 6, less than 0.03% reflection and over 96% transmission of incident radiation. These results indicated a flexible route to the fabrication of impedance matched materials for antenna miniaturisation, which was demonstrated by the casting of impedance matched 5 cm diameter hemispheres.

Hybrid ferromagnetic composites composed of $Ni_{0.4}Zn_{0.6}Fe_2O_4$ ferrite powder and Fe particles in an epoxy matrix with various composition ratios were also prepared by the mould casting route. Planetary ball milling was introduced to pre-grind Fe and NiZn ferrite filler mixtures before casting, which resulted in fragmentation of the NiZn ferrites and modification of the Fe morphology from spherical particles to sub-micron flakes. Composites containing the ball milled fillers exhibited a remarkable improvement in electromagnetic properties over the "as supplied" materials, especially in the suppression of dielectric and magnetic loss. By combining the characteristics of high resonant frequency of the Fe and low energy losses of the ferrite, an optimum mixture of ball milled 15 vol.% NiZn ferrite and 38 vol.% Fe in a hybrid epoxy-based composite gave an approximately one order of magnitude higher extended operating bandwidth over a ferrite-only composite, suppressing dielectric and magnetic loss tangents to approximately 10^{-2} up to 150 MHz without significant deterioration of permeability. This approach of manipulating multi-phase ferromagnetic material

fractions and their structure may provide flexibility in the development of bespoke electromagnetic materials for applications in telecommunications.

A spray deposition route was demonstrated to provide a flexible approach for the fabrication of nanocomposite films. Free standing nanocomposite films (up to 100 μm thick) based on fluoropolymer perfluoro alkoxy (PFA)/multiwall carbon nanotubes (MWCNT)/PFA multilayer films were spray formed and had an ultra-high permittivity of ~ 10^4 at a very low MWCNT concentration (< 0.5 vol.%) at low frequencies (< 1 kHz). These coatings were however also highly lossy despite insulating the conducting MWCNT in a polymer "sandwich". These films might be useful as absorbers. Ferrofluid (< 10 nm magnetite (Fe_3O_4) particles) were also introduced during the spray forming of sandwich structure films. Large scale flexible and robust PFA/Fe_3O_4 (ferrofluid)/PFA nanocomposite ~ 60 μm thick films up to 13 × 13 cm were manufactured successfully by the spray deposition technique, and showed increased static magnetization with increased thickness of magnetic filler layer.

However, the measurement of electromagnetic properties of these and similar polymer-based film for possible microwave applications become relatively problematic, especially for broadband magnetic characterization. Therefore, a new coaxial line technique for measuring the high frequency broadband complex permittivity and permeability of polymer-based films from 50 MHz up to 18 GHz without the need for a reference sample for calibration was developed. The approach was based on an analytical air gap correction model, which was then validated by

experiments and finite element simulations. The relative effects of film thickness and air gap on a range of measured permittivities and permeabilities was then elucidated.

Extending the earlier findings, the work was extended to anisotropic electromagnetic materials that could direct the propagation of electromagnetic waves, and two fabrication approaches for aligning anisotropic magnetic inclusions within a polymer matrix and stacking multilayer structures were explored. Based on simple simulations, and subsequently shown experimentally, strong magnetic anisotropy could be obtained in stacked dielectric and magnetic layer structures, and the maximum anisotropy for a certain materials combination occurred when the magnetic material and non-magnetic material were equally spaced in a repeating, alternating structure. Based on experimental measurements of magnetically anisotropic tiles, a design study using 3D simulations showed that these tiles could influence induced current flows in a ground plane placed beneath a dipole antenna. Under an optimum configuration suggested by simulation, the resulting far-field radiation pattern produced by the dipole antenna provided high-gain radiation patterns even when the dipole was placed 25 times nearer to the ground plane, facilitating a significantly lower physical profile.

Lastly, a preliminary feasibility study was conducted to investigate if 3D printing might offer significant potential to realize complex transformation optics devices. This work involved the development of printable magnetic composite feedstock with a range of NiZn ferrite loadings, and the development of re-optimised 3D printing parameters e.g. nozzle size and temperature, feed rate, traverse speed of the head, etc.

for the case of the 3D printing, or additive manufacture, process commonly referred to as fused deposition modelling (FDM). A maximum printable fraction of 25 vol.% NiZn ferrite/ABS composite filament was achieved with a real permittivity of ~ 3 and real permeability of ~ 2. It was also demonstrated that a complex 3D diamond-like lattice structure could be printed using a 10 vol.% NiZn ferrite/ABS composite filament. The exploration of printable magnetic composites can provide increased design freedom for direct realization of devices with graded or anisotropic electromagnetic properties operating at microwave frequencies.

Overall, the thesis has shown that while microwave interactions with composites generally produces less "spectacular" effects than resonating metamaterial structures, they offer considerably more flexibility from a manufacturing point of view. In particular their utility in broadband ground plane applications has been suggested, where previously very little magnetic anisotropic effects had been studied or exploited. Additive manufacture offers enormous potential for anisotropic, graded and resonating structures within a single, one-step manufacturing design, but considerably more work is required in low loss feedstock materials, especially those with useful permeabilities at 1 GHz or above.

8.2 Future Work

Several further directions following on from this work can be envisioned:

- Synthesis of conducting-insulating core-shell particle structures for magnetic polymer composites. Metallic magnetic materials e.g. NdFeB, AlNiCo, AlNiFe alloys, etc. are known to have high saturation magnetization and are capable of maintaining high magnetic permeability at microwave frequencies, but suffer severely from high dielectric losses. Using alloy-oxide core-shell fillers such as self-passivating alloy particles may restrict the dielectric losses to a low level and maintain a relatively high magnetic permeability at working frequencies.

- Investigation of multi-phase composites that may involve high permittivity particle fillers e.g. $BaTiO_3$, $SrTiO_3$, $BaSrTiO_3$, etc., high permeability particles fillers e.g. yttrium iron garnet (YIG), hexaferrite, semiconductor fillers such as C, Ge or Si, and noble metals such as nanosize Ag particles. A wide range of filler material and particle size combinations can be explored, and based on Fe/ferrite findings here, that may have interesting and beneficial electromagnetic interactions with each other in the composites.

- The interfaces in the composite (e.g. filler-matrix, filler coating-core, different material filler-filler, etc.) are considered to be important and may even dominate the electromagnetic properties of the composite. However there has been little conclusive work on this topic. Therefore, investigation into the role

of interfaces on the effective properties may provide a guideline for developing better composite materials.

- To experimentally validate the benefit of anisotropic ground planes for low profile antenna applications, and investigate the possible underlying mechanisms.

- Further development of printable composite materials and improved fabrication process for filament feedstock are needed for additive manufacture to fulfill its potential. Acrylonitrile butadiene styrene (ABS) was chosen as the matrix polymer in this preliminary investigation due to its well-known ease of printing, low cost and wide availability. Other polymer materials may provide better properties e.g. mechanical, thermal, loss, processability, etc., and could be developed in forms or variants suitable for additive manufacture. For example, polyethylene, which is less rigid and brittle than ABS, has recently been shown in our research group to be capable of higher filler loadings, and therefore could provide a wider range of composite permittivity and permeability values.

List of publications on the DPhil project

1. Y. Wang, P.S. Grant, "NiZn ferrite/Fe Hybrid Epxoy-based Composites: Extending Magnetic Properties to High Frequency", Applied Physics A 117(2), 477 2014.

2. Y. Wang, E. Edwards, I. Hooper, N. Clow, P.S. Grant, "Scalable Polymer based Ferrite Composites with Matching Permeability and Permittivity for High-Frequency Applications", Applied Physics A, 120(2), 609 2015.

3. Y. Wang, F. Castles, P.S. Grant, "3D Printing of NiZn ferrite/ABS Magnetic Composites for Electromagnetic Devices", 2015 MRS Spring Meeting proceedings, 1788, mrss15-2116292 doi:10.1557/opl.2015.661.

4. P.S. Grant, F. Castles, Q. Lei, Y. Wang, J. M. Janurudin, D. Isakov, S. Speller, C. Dancer, C. Grovenor, "Manufacture of electrical and magnetic graded and anisotropic materials for novel manipulations of microwaves", Philosophical Transactions of the Royal Society A, accepted.

5. Y. Wang, I. Hooper, E. Edwards, P.S. Grant, "Gap Corrected Thin Film Permittivity and Permeability Measurement with a Broadband Coaxial Line Technique", IEEE Transactions on Microwave Theory and Techniques, Submitted.

6. Y. Wang, N. Clow, P.S. Grant, "Application of High Anisotropic Magneto-Dielectric Materials in Low Profile Antenna", in preparation.

7. Y. Wang, P.S. Grant, “High Permeability and Low Loss Hybrid Ferromagnetic Composite for Very-High-Frequency Applications”, META’14, the 5th International Conference on Metamaterials, Photonic Crystals and Plasmonics, May 2014, Singapore.

8. Y. Wang, D. Isakov, P.S. Grant, “Nanocomposite Films with Controlled Dielectric and Magnetic Properties for Spatial Transformation Applications”, NanoMeta 2015, the 5th international Topical Meeting on Nanophotonics and Metamaterials, January 2015, Seefeld, Tirol, Austria.

9. Y. Wang, P.S. Grant, “Ferrite composite with broadband matching permittivity and permeability for antenna miniaturization application”, Royal Society Theo Murphy international scientific meeting: Spatial Transformations from Fundamentals to Applications, January 2015, The Royal Society at Chicheley Hall, Buckinghamshire, UK.

10. Y. Wang, F. Castles, P.S. Grant, “3D Printing of Magnetic Materials for Metamaterial Devices”, 2015 MRS Spring Meeting and Exhibit, April 2015, San Francisco, California, US.